Unravelling the Excitonics of Semiconductor Nanocrystals

An effort in guiding the design of novel structures for optoelectronic applications through spectroscopy

Jonathan I. Saari

A thesis submitted to McGill University in partial fulfillment of the requirements for the degree of

Doctor of Philosophy

Department of Chemistry, McGill University, Montreal, Quebec, Canada

For Tiny Tim (you know who you are), my family, and Chantal

Abstract

The optical modulation of the multiexitonic multiplicity of CdSe/ZnS nanocrystals (NC) through state-specific excitation demonstrated the potential of NCs as a novel platform for all-optical logic and switching with modulation rates reaching 1 THz, as dictated by Auger recombination. An optical pumping scheme demonstrating all-optical AND gating through CdSe/ZnS NCs made use of the unique multiexcitonic interactions of colloidal nanocrystals.

State resolved pump-probe spectroscopic techniques were applied to study the relative excitonic environments of freshly synthesized and aged CdTe NC. These experiments reveal fast electron trapping for aged CdTe NC from the single excitonic state (X). Pump fluence dependence with excitonic state-resolved optical pumping enables directly populating the biexcitonic state (XX) which produces further accelerated electron trapping rates. This increase in electron trapping rate triggers coherent acoustic phonons by virtue of the ultrafast impulsive timescale of the surface trapping process. The observed trapping rates were discussed in terms of electron transfer theory.

The subtleties of the excitonic couplings within NCs motivated the development of a novel two-dimensional electronic spectrometer with active carrier-envelope phase stabilization, capable of both collinear and non-collinear geometry. Pulse-generation was achieved through synched acousto-optic programmable dispersive filters. Phase stability was measured through spectral interferometry and found to be in excess of λ/300 for over an hour. The highly phase-stable design allowed for complete polarization control through pulse-pair recombination in a beam-splitter. Polarization control was achieved through sweeping the relative phases of the shaped pulses and demonstrated through a Mueller ellipsometer. Both one- and two-colour proof-of-principle experiments were performed on CdSe NCs.

Résumé

La modulation optique de la multiplicité multi-excitonique des nanocrystaux CdSe/ZnS obtenue par excitation d'états spécifiques démontre le potentiel d'application de ces matériaux dans le domaine de la logique optique, atteignant des taux de modulation de l'ordre de 1ThZ comme dicté par le taux de recombinaison d'Auger. Grâce à une méthode de pompage optique, une fonction « ET » a été réalisée avec des nanocrystaux de type CdSe/ZnS, mettant ainsi à profit les interactions multi-excitoniques uniques de ces nanocrystaux colloïdaux.

Des techniques spectroscopiques pompe/sonde résolues en états quantiques ont été appliquées afin d'étudier les différences d'environnements excitoniques entre des points quantiques CdTe fraîchement synthétisés et ayant vieilli. Dans le cas des points quantiques âgés, ces expériences révèlent une rapide capture de l'électron par l'état excitonique simple (X). Le fait que la nature de l'état excitonique optiquement excité dépende de la fluence de la pompe permet de directement peupler l'état bi-excitonique (XX), ce qui a pour effet d'accélérer le taux de capture d'électrons. Cette augmentation du taux d'électrons capturés provoque l'émission de phonons acoustiques en vertu des dynamiques ultrarapides des processus de capture à la surface des nanocrystaux. Les taux de capture observés lors de ces expériences ont été discutés dans le cadre de la littérature sur le transfert de charge.

Les subtilités des couplages excitoniques au sein des nanocrystaux a motivé le développement d'un spectromètre bi-dimensionnel dans le domaine du visible, pourvu d'un mécanisme de stabilisation de la phase de l'enveloppe des pulses et capable d'opérer en géométries colinéaires et non-colinéaires. La génération des pulses a été obtenue grâce à des filtres dispersifs accousto-optiques programmables. La stabilité de la phase a été mesurée par interférométrie spectrale et une valeur supérieure à $\lambda/300$ a été obtenue sur plus d'une heure. Ce montage, possédant une grande stabilité des phases, permet de contrôler la polarisation des pulses excitant l'échantillon en combinant une paire de pulses dans un miroir semi-réfléchissant. Le contrôle de la polarisation a été obtenu en balayant les phases relatives des pulses et en les observant dans un ellipsomètre de Müller. Des expériences à une et deux couleurs ont été réalisées sur des nanocrystaux de type CdSe, établissant ainsi la preuve du concept.

Acknowledgements

Graduate studies are, ideally, a lifetimes opportunity to sate an intellectual curiosity through the pursuit of an unknown. In few other situations is one given the resources and freedom to pursue their passion without the burden of quarterly reports, grant proposals, and overbearing micromanagement. True, there is still tedium, instrumental failure, and invigilation but these are a small price to pay.

More than all this, however, is the reward found in the passionate, like-minded, and quirky people with whom you share your hunt. To this end, I would like to thank Drs. Samuel Sewall and Ryan Cooney. The mentorship they provided was shadowed only by the sheer love they shared for the hard work and kinship essential for the pursuit of any goal. They drove themselves and in turn inspired others. This kinship is spawned from the inherently collective effort that is life in an ultrafast lab. Brenna Walsh, Dr. Amin Kabir, Hélène Seiler, Pooja Tyagi, and Dr. Eva Dias were my team – I would have accomplished nothing if it weren't for them. I also had the pleasure of collaborating with a number of professors and students during my time at McGill: Dr. Jay Nadeau was always a willing supplier of samples – despite my constant demands. Danielle Reifsnyder and Dr. Christopher Murray also delivered many a CdTe care package. Dr. Bradley Siwick and Dr. Paul Wiseman were always willing to give their time for my annual reviews, along with their immeasurably useful comments and suggestions.

Vance Morrison, Christopher Godbout, Jason Boubalos, Mark Stern, Andrew Bruhacs, Robert Chatelain, Kunal Tiwari - these are the people who made the highs the highest. They are my friends and I am forever in their dept.

The life of a scientist, however, is also a life fraught with lows. Stresses, insecurity, and politics all delight in the mind of one who pursues the intangible. For some daemons, there is only family. In this regard, I am incredibly blessed. My father, mother, sister, and brother in law, all of them – theirs are the shoulders on which I stand. I would be nothing, and am nothing, without them.

The world of a graduate student is confined to a 5 year period. Their perception, their ambitions, at least in my case, becomes entangled with their lab, and their pride in their own work. I feel innately and directly connected to its future. I take pride in knowing its path. It can be difficult to see life beyond; however, one of the joys comes from mentoring future graduate students. I am more than confident in passing the torch to the next generation of students and lab leaders: Brenna Walsh, Hélène Seiler, and Lakshay Jethi.

There is one above all else I wish to thank as without their tireless efforts securing funding, providing infrastructure and intellectual freedom, none of this would be possible, my supervisor: Dr. Patanjali Kambhampati.

Statement of Originality and Contributions

The following represents a brief summary concerning the novel contributions to the scientific community by the author.

Introductory Chapters

The introductory chapters involve a broad literature and theory review concerning spectroscopic techniques and nanocrystal science in general. The review is a collective presentation of work not performed by the author.

Chapter 3

The state-resolved spectroscopic technique, as developed by Drs. Kambhampati, Sewall and Cooney, was used to directly manipulate the excitonic multiplicity of CdSe/ZnS nanocrystals in an effort to investigate the effect of tailored pulse sequences on CdSe/ZnS nanocrystals. This work builds upon the initial state-resolved work performed by Drs. Sewall and Cooney. The experimental design, as described throughout the chapter, including pumping schemes and sources was the work of the author. Similarly, the analysis as well as figure generation were primarily performed by the author. The manuscript was first written by the author and subsequently edited by Dr. Kambhampati. The manuscript as manifest in the dissertation is greatly expanded by the author. Minor assistance in experiment was provided by Brenna R. Walsh and Michael M. Krause. This work is the pioneering demonstration of a novel direction for optoelectronic research involving nanocrystals: optical transistors and logic.

Chapter 4

The surface studies performed on CdTe were a collaborative effort between the groups of Dr. Chris Murray and Dr. Kambhampati. The synthetic efforts, as described in the chapter, were performed by Dr. Eva Dias (Kambhampati group) as well as Danielle Reifsnyder (Murray Group). The spectroscopic results represent the primary contribution of the author, as well as the figure generation and analysis. The manuscript was written along with Dr. Kambhampati. The chapter as in the dissertation has been expanded and revised by the author. The studies provide a thorough investigation into the ultrafast signatures pertinent to surface trapping. These signatures are of some significance to the field. Similarly, minor experimental assistance was provided by Brenna Walsh and Michael Krause.

Chapter 5

The development of a novel 2D spectrometer was a joint venture between the author and Dr. Pooja Tyagi as well as Fastlite Inc. The primary technical developments as well as the first successful (and subsequent) experiments were performed by the author with assistance from Brenna Walsh and Dr. Amin Kabir. This technical development involved modification and completion of an existing GUI developed by Fastlite inc, trouble-shooting and design of the interferometer, and proof-of-principle experiments on laser dyes such as Nile Blue and Rhodamine 6G as well as CdSe nanocrystals.

The bulk of the analysis and theoretical work concerning the manuscript was performed by Dr. Pooja Tyagi. The manuscript as it appears in the dissertation is solely the work of the author aside from the exceptions described in the forward to the chapter.

The novelty arises in the dual-AOPDF design as described in the chapter. This design greatly simplifies the many technical difficulties involved in the highly phase-sensitive measurement that is 2D electronic spectroscopy. The design allows for direct feedback controlled active phase-stabilization as well as complete control over output pulse polarization.

Chapter 6

The final chapter is a collection of experiments and technique development ideas as envisioned by the author. The details and figures within are the sole effort of the author with the exception of the final figure which was taken with the assistance of Kunal Tiwari.

Table of Contents

Section 1: Introduction and Theory

Chapter 1 Ultrafast Spectroscopy: A Window Into Excitonics

Chapter 2 Nanocrystals

Section 2: Experimental Results

Chapter 3 Nanocrystals: A Platform for Optical Signal Processing

Chapter 4 The Surface

Chapter 5 Two Dimensional Electronic Spectrometer

Chapter 6 Concluding Remarks and Future Works

Section 1: Introduction and Theory

1 Ultrafast Spectroscopy: A Window into Excitonics

1.1 – Introduction

The theoretical work by Townes and Schawlow in the late 1950s[1], and the subsequent advent of the ruby laser by Maiman in 1960[2] (Figure 1.1a), provided the physical sciences with a powerful tool to explore the interaction of light and matter. The progression of laser technology has led to intensities ranging from pico- to petaWatts and nanoscale devices to kilometer sized cavities. The laser today is ubiquitous not only in research but also our daily lives.

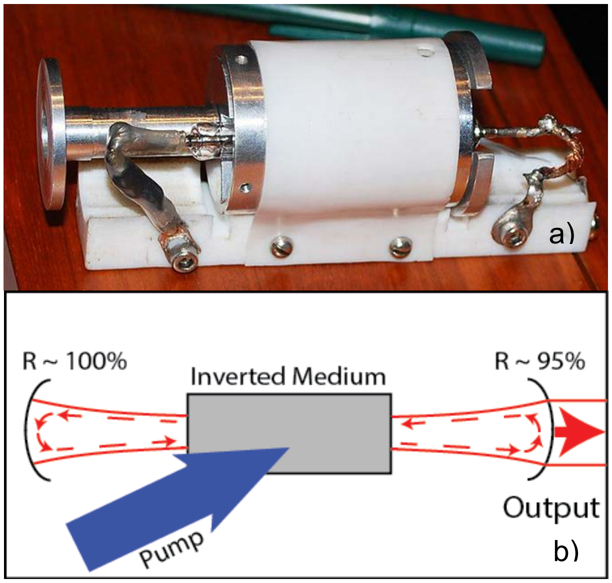

Figure 1.1 – a) The Ruby laser. (wiki commons) b) Simplified diagram depicting the major components of a laser cavity

Despite the almost arbitrary complexity of modern laser cavities, lasers are generally comprised of four components: a gain medium, some pump source, be it chemical, electrical, or optical, to create the population inversion, an output coupler, and a high-reflector (Figure 1.1b) creating a resonant cavity.[3] There exist a plethora of invertible media such as solid-state semiconductor diodes, crystals, various gasses, chemical dyes, and so on, each with their own practical advantage and use.[3, 4]

There are also a number of ways to invert a medium. An excited dimer, or excimer, laser uses high voltage to create a meta-stable bound state of a given gas combination which subsequently relaxes through emission of photons.[4] Dye lasers are often optically pumped by the second harmonic of electrically pumped solid-state lasers like a Q-switched neodymium-doped yttrium aluminum garnet (ND:YAG) laser.[4] Chemical lasers, such as carbon dioxide lasers, involve an electrical discharge and the energy transfer between compounds, such as N_2 and CO_2, to develop population inversion.[4]

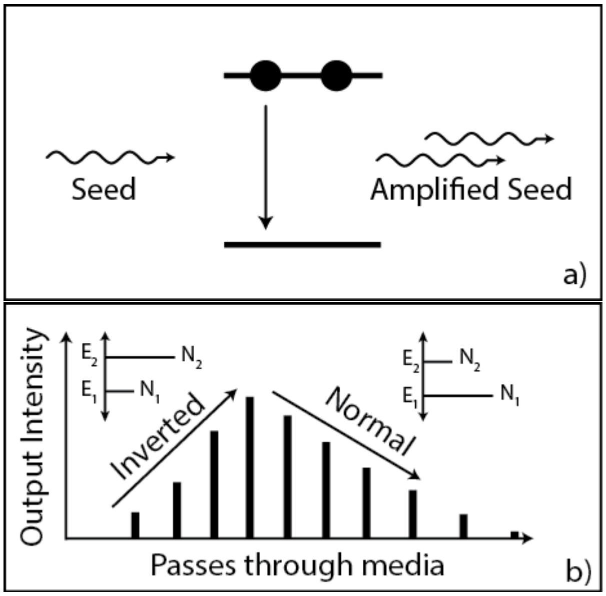

Figure 1.2 - a) Cartoon depiction of amplified stimulated emission. b) Pulse intensity as a function of cavity round trips in a model system.

A laser either generates or amplifies a coherent electromagnetic wave through the stimulated emission of a transition whose energy is resonant with the impingent wave [3] as shown in Figure 1.2a. In the case of an oscillator or amplifier, throughout multiple passes in a cavity, a field acting on an inverted population stimulates the relaxation of an excited species thereby amplifying the beam, or seed. In the absence of an inverted ground state population, on average, the seed would simply be absorbed (Figure 1.2b).

This chapter is intended to guide the reader through a brief summary of spectroscopy and laser theory with the end goal of design and implementation of linear and non-linear spectroscopic instrumentation. Specifics concerning the infrastructure used throughout later chapters will be covered.

1.2 Theory

Generally, optical gain is a study of the competition kinetics of transitions. Einstein provided the primary theoretical description of the major contributors to atomic transition probabilities given a thermally equilibrated two level system in the dipole approximation, the Einstein coefficients [5]:

$$\frac{N_2}{N_1} = e^{-h\nu/k_bT} = \frac{B_{1-2}\rho(\nu)}{A_{2-1}+B_{2-1}\rho(\nu)} \qquad (1.1)$$

where $\rho(\nu)$ is the radiation density of an impingent electromagnetic field resonant with the transition:

$$\rho(\nu) \sim \overline{E^2}(\,\nu) \qquad (1.2)$$

Three competing processes were defined: absorption, stimulated emission, and spontaneous emission with their relative probabilities given by B_{1-2}, B_{2-1}, and A_{2-1} respectively (Figure 1.3). Of note is the radiation density, $\rho(\nu)$, term present for both the B_{1-2} and B_{2-1}, while all processes are generally dependent on the square of the magnitude of the transition dipole:

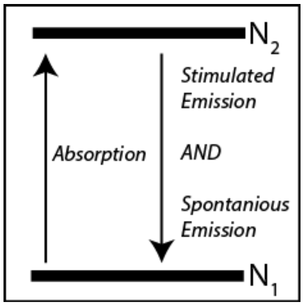

Figure 1.3 – Two-level system with three competing processes.

$$B_{1-2} = \ B_{2-1} \sim \rho(\nu)\ |\ \mu_{21}|^2 \qquad (1.3a)$$

$$A_{2-1} \sim |\ \mu_{21}|^2 \qquad (1.3b)$$

absorption and stimulated emission are both dependent on the intensity of the impingent field. They are stimulated transitions: both require a resonant external electromagnetic field, or photon, in order to occur. This photon may originate from another atom or molecule in the system itself through spontaneous emission or another light source acting as a seed (Figure 1.4b). The interplay between absorption and stimulated emission is dictated by excited state populations as shown in Figure 1.4. In order to achieve amplified stimulated emission (ASE) the contribution of stimulated emission (SE) must overcome the absorption of said photon, or, there must exists a greater population in an excited state throughout the sampled ensemble than population to be excited in resonant transition. This is known as a population inversion. The discussion of population inversions is specifically pertinent to the dissertation as a large portion of the material presented in chapter 3 involves optical gain.

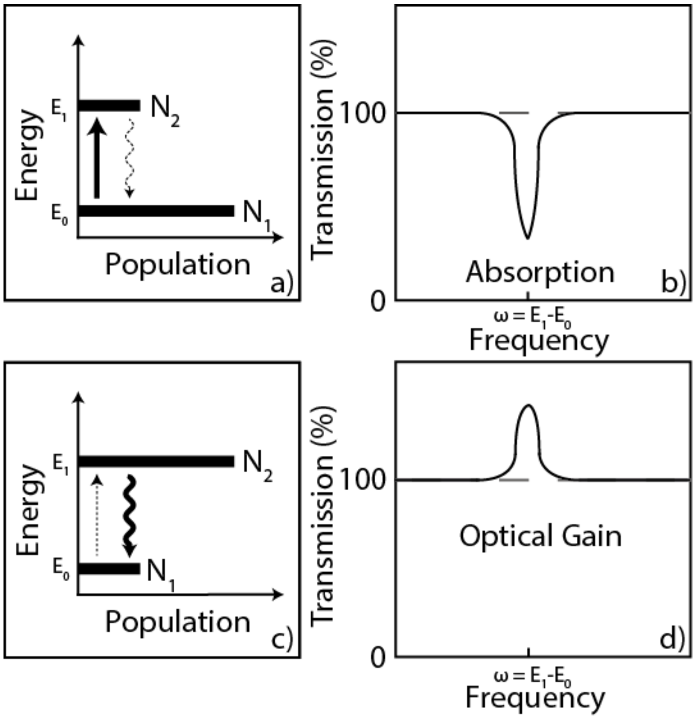

Figure 1.4 – a) Simplified 2-level model for non-inverted medium. b) Impingent electromagnetic wave is absorbed. c) Inverted 2 level system d) Seed is amplified

1.2.1 - Population inversion

Consider a two level system with ground and excited state energies of E_1 and E_2 respectively. The thermal population distribution at room temperature is given by the Boltzman equation:

$$\frac{N_2}{N_1} = e^{-\Delta E / k_B T} \qquad (1.4)$$

where N_i are the respective populations, k_B is Boltzmann's constant, and $\Delta E = E_2 - E_1$. Given a thermal equilibrium and $\Delta E > 0$, the ratio of N_2/N_1 will never exceed one. This suggests a population inversion for a thermally populated two-level system will never occur; in other words: a material will not lase on its own.

In order to achieve population inversion, in the case of large ΔE, it is apparent that a strong external field must be applied. Two-level population inversion, in non-thermally equilibrated situations, may occur in the absence of strong dephasing, as with spins in Nuclear Magnetic Resonance spectroscopy (NMR).[5, 6] However, an appropriate model to address a given electronically or optically pumped laser system is a four-level model, as shown in Figure 1.5. In this case, a high-energy transition is excited through a resonant pump. This excited state relaxes quickly into a lower energy excited state which then radiatively relaxes to state E1. The E_1 transition then quickly relaxes back to ground state, maintaining thermal population. The relative competition kinetics between the transitions allows for the population inversion of a material.[3]

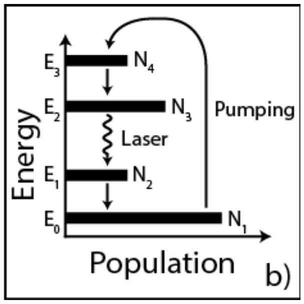

Figure 1.5 – Four-level model for laser system

The excited states for these systems have lifetimes themselves. Relaxation, intersystem crossing (in molecules), phonons, bath collisions and other forms of dephasing inherent in systems dictate the final stimulated emission lifetime and linewidth, two topics which will be covered in length in later portions of the chapter.

The primary theme in terms of this dissertation is the interplay between population inversion, optical transparency, and absorption. Given a simplified two-level system, optical transparency occurs when there is an equal population in the higher lasing level and the lower. When population is greater in the higher lasing level, stimulated emission will occur on average. When the higher lasing level has lower population, absorption at that frequency will dominate.

Spectroscopy is the indirect study of matter through the influence of a system on a given field. Absorptive spectroscopy measures the attenuation of a field by a sample; photoluminescence spectroscopy measures the spontaneous emission of a sample caused by excitation through a field. All of these techniques rely on a field-matter interaction.

1.2.2 – Field-Matter Interaction

In general, a measurement is made through a square law detector that reads the intensity of the desired field and may or may not be coupled to a spectrometer. These detectors measure either the self-acted or heterodyned field, depending on geometry. In the case of heterodyne detection, the signal field and local oscillator are mixed. In pump-probe geometry, the probe pulse is attenuated through self-action of the signal field.[7] The signal field is a manifestation of the non-equilibrium polarization of the material by the preceding pump-pulses that radiates a phase-lagged field which either attenuates the final beam (in the case of self-action) or mixes with the local oscillator. This polarization is a result of the time evolution of the system after multiple field-matter interactions. The multiple field-matter interactions are described through a response function. The response function may comprise many theoretical treatments from correlation functions and line shape models to dipole operators and strict eigenstates. The key to understanding any given linear or non-linear experiment is deriving the various response functions which contribute to the induced polarization with the appropriate level of theory.

An electromagnetic field, in terms of Maxwell-Liouville equations described later, interacts through the induced polarization of the sample.[6, 7] The polarization may be described in terms of powers of the electric field with subsequent material susceptibilities ($\chi(\omega)^{(n)}$):

$$P = \varepsilon_0(\chi(\omega)^{(1)} \cdot E + \chi(\omega)^{(2)} \cdot E \cdot E + \chi(\omega)^{(3)} \cdot E \cdot E \cdot E + \cdots) \quad (1.5)$$

which lead to the convenient separation of orders, namely linear

$$P^{(1)} = \int_0^\infty dt_1\, R^{(1)}(t_1)E(t - t_1) \quad (1.6)$$

dealing with the linear response function $R^{(1)}$, and non-linear polarization:

$$P^{(n)}(t_{n,}\, \dots, t_2, t_1) =$$

$$\int_0^\infty dt_n \dots \int_0^\infty dt_2 \int_0^\infty dt_1\; R^{(n)}(t_n, \dots, t_2, t_1)\; \cdot \quad (1.7)$$

$$E(r, t - t_n)E(r, t - t_n, \dots - t_2)E(r, t - t_n \dots - t_2 - t_1)$$

which relates to the nth level response function.

The polarizability expansion is pertinent beyond description of the linear and non-linear responses in a spectroscopic sense. It forms a basis for non-linear optics in general.[8] For example, in non-inversion symmetric media, such as the birefringent crystal β-Barium borate (BBO), where the even-order responses do not cancel out, the polarizability expansion provides the formulation for sum and difference frequency generation as discussed later.[8, 9]

In general throughout this chapter the electromagnetic field will be treated as a plane wave [7]:

$$E = E_0 \cos(\omega t) \tag{1.8a}$$

$$E = \frac{1}{2} E_0 (e^{-i\omega t} + e^{i\omega t}) \tag{1.8b}$$

The system will be expressed through an appropriate Hamiltonian which will be first derived for simple systems, then expanded to the condensed phase. The following will provide a general description of non-linear optics and response functions in terms of pump-probe and two-dimensional electronic spectroscopy. Similarly, a brief discussion on the effect of system fluctuations on spectral line shapes will be presented. If one is interested in the combined quantum electrodynamic descriptions, the reader is pointed towards references. [4, 6, 7, 10]

1.2.2.1 – What Does Spectroscopy Measure

As alluded to, ensemble spectroscopy relies on measuring the influence of an electromagnetic field on the materials macroscopic polarization. Therefore, an understanding of the sources of macroscopic polarization in a given n-wave mixing experiment is crucial to an understanding of the results. The theoretical approach to interpreting the physics behind non-linear spectra, at the level of this dissertation, is embedded in either Hilbert or Liouville space.[7] To begin, consider the time-evolution of the density matrix given by the Liouville Von-Newman equation:

$$\frac{\delta\rho}{\delta t} = -\frac{i}{\hbar}[H,\rho] \tag{1.9}$$

The density matrix, ρ , is a representation of the system with the diagonal elements ρ_{nn} representing the probability of the system being in a given state, or the population, and the off-diagonal elements ρ_{nm} representing the coherences, or couplings, between states of the system. The immediate benefit is that, beyond the possible treatment of non-pure states, the expectation value of an observable, A, is simply given by taking the trace of the density matrix [5, 7]:

$$\langle A(t)\rangle = Tr[A\rho(t)] \tag{1.10}$$

However, this treatment remains in Hilbert space wherein operators are defined as matrices. Liouville space treats the density matrix as a vector:

$$\rho_{Hilbert} = \begin{bmatrix} \rho_{11} & \rho_{12} \\ \rho_{21} & \rho_{22} \end{bmatrix} \Rightarrow \rho_{Liouville} = \begin{pmatrix} \rho_{11} \\ \rho_{22} \\ \rho_{12} \\ \rho_{21} \end{pmatrix} \tag{1.11}$$

The transformation of the density matrix into Liouville space introduces the Liouville space superoperators, which for a two-state system takes the form [7]:

$$\frac{d\rho_{Liouville}}{dt} = -\frac{i}{\hbar}[H_{Lioville}, \rho_{Liouville}] \tag{1.12a}$$

$$\frac{d}{dt}\begin{pmatrix} \rho_{11} \\ \rho_{22} \\ \rho_{12} \\ \rho_{21} \end{pmatrix} = -\frac{i}{\hbar}\begin{bmatrix} 0 & 0 & -V_{21} & V_{12} \\ 0 & 0 & V_{21} & -V_{12} \\ -V_{12} & V_{12} & \Delta E_{12} & 0 \\ V_{21} & -V_{21} & 0 & \Delta E_{21} \end{bmatrix}\begin{pmatrix} \rho_{11} \\ \rho_{22} \\ \rho_{12} \\ \rho_{21} \end{pmatrix} \tag{1.12b}$$

These superoperators act solely to the right (or, 'from the left') unlike the Hilbert space equivalents, which may act on either the bra or the ket. This arises from the nature of the superoperators: each superoperator within Liouville space is now a coupled treatment of bra and ket, labelled through four indices:

$$A_{jk,mn} = \langle\langle jk \vert A \vert nm \rangle\rangle \tag{1.13}$$

The conversion between Hilbert space and Liouville space operators given by:

$$A_{jk,mn} = A_{nn'}\delta_{mm'} - A^{*}_{mm'}\delta_{nn'} \tag{1.14}$$

with $A_{nn'}$ being a standard Hilbert space operator.

1.2.2.2 – The Interaction Picture

Often when considering the influence of an external field on a system it is convenient to split the Hamiltonian into an exact, often time-independent system Hamiltonian and a time-dependent perturbative field [5-7]:

$$H(t) = H_0 + V(t) \tag{1.15}$$

assuming the influence of $V(t)$ is sufficiently weak. With an impingent electromagnetic field, the Hamiltonian may become:

$$H(t) = H_{sys} + V_{Light+Matter}(t) \tag{1.16}$$

where $V_{Light+Matter}(t)$ modulates the coupling between the incident field with the initial and final states of the system.

How does $V_{Light+Matter}(t)$ influence the system? Considering a material is a collection of charged particles, the force exerted by the EM field is given by the Lorentz force [5]:

$$F = q(E + \frac{1}{c}(V \times B)) \tag{1.17}$$

q and v are the charge and velocity of the particle respectively with E and B, the electronic and magnetic fields respectively. Classically, an incident electric field will affect the equilibrium of the system as it may displace the charged particles as shown in Figure 1.6.

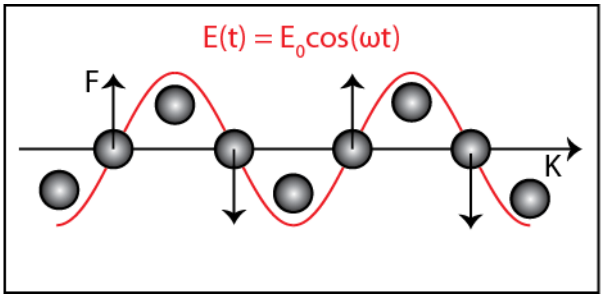

Figure 1.6 – Classical representation of a charged particle in an EM field.

Quantum mechanically, the field couples through the dipole operator generating coherent superpositions of states. Assuming a Coulomb gauge, classically, the Hamiltonian for a single charged particle in an EM field is given by [11]:

$$H_{Classic} = \frac{1}{2m}[\bar{p} - q\bar{A}(\bar{r},t)]^2 \tag{1.18}$$

where q is the charge of the particle, $\bar{p}$ the canonical momentum, and $\bar{A}$ is the vector potential associated with the electric field from Maxwell's equations. The quantum analogue is [5]:

$$H_{QM} = \frac{1}{2m}(-\hbar^2\nabla^2 + \frac{q^2}{c^2}|A|^2 + 2\frac{i\hbar q}{c}\bar{A}\cdot\bar{\nabla}). \tag{1.19}$$

In the perturbative limit, where the impingent EM field is weak, the $\frac{q^2}{c^2}|A|^2$ term is dropped leaving:

$$H_{QM} = \frac{1}{2m}(-\hbar^2\nabla^2 + 2\frac{i\hbar q}{c}\bar{A}\cdot\bar{\nabla}) \tag{1.20}$$

which becomes, for a collection of charged particles:

$$H = H_o + V(t) \tag{1.21a}$$

$$H_0 = -\sum\frac{\hbar^2}{2m_j}\nabla_j^2 + V \tag{1.21b}$$

$$V(t) = \sum_j \frac{e}{m_j c}\bar{A_J}\cdot\bar{\nabla_J}. \tag{1.21c}$$

The non-equilibrium dynamics of interest begin with the light-pulse. The system experiences the perturbation for the duration of the pulse and the material then subsequently evolves. The explicit time dependence of the system lies with the weak perturbation. The separation of the total Hamiltonian into a time-independent, often known, system Hamiltonian, and a time-dependent interaction term leaving the system to evolve freely through the operators is the interaction picture [6, 7]:

$$H_{total} = H_0 + V_I(t) \tag{1.22a}$$

$$H_0(t) = H_0 \tag{1.22b}$$

$$H_I(t) = e^{iH_0t/\hbar}H_0e^{-iH_0t/\hbar} \tag{1.22c}$$

with the time-evolution of the density matrix given by the von-Newman equation:

$$\frac{d\rho}{dt} = -\frac{i}{\hbar}[V_I(t), \rho_I(t)] \tag{1.23a}$$

$$V_I(t) = e^{iH_0t/\hbar}Ve^{-iH_0t/\hbar} \tag{1.23b}$$

and the dipole operator becomes:

$$\mu_I(t) = e^{\frac{iH_0(t-t_0)}{\hbar}} \mu\, e^{\frac{-iH_0(t-t_0)}{\hbar}} \qquad (1.24)$$

This provides a simplified method of calculating the influence of multiple weak pulses on a given material, as will be shown later in the discussion of time-ordering.

1.2.2.3 – Macroscopic Polarization

The induced macroscopic polarization of a sample is the window of spectroscopy. The difficulty comes in discerning the coupling between the microscopic polarization of multiple randomly-or-otherwise oriented particles within a system and an electromagnetic field of a given polarization. How much will each individual particle contribute to the ensemble measurement? This inherently requires statistical mechanics.[6, 7] In the case of optical spectroscopies, where the typical length scale of an interacting system is less than that of the wavelength of the incident field, one can invoke the Dipole approximation [5-7] which leads to a transition dipole moment. Consider an ensemble of molecules, the molecules, assuming gas-phase, will be randomly oriented about space. Their bonds and electronic orbitals will similarly be randomly oriented. Intuitively from equation 1.17, the strength of the coupling of an incident linearly polarized EM field will be dependent on the magnitude to which the EM field can project about the system, as shown in Figure 1.7 An example of this point is the anisotropy in

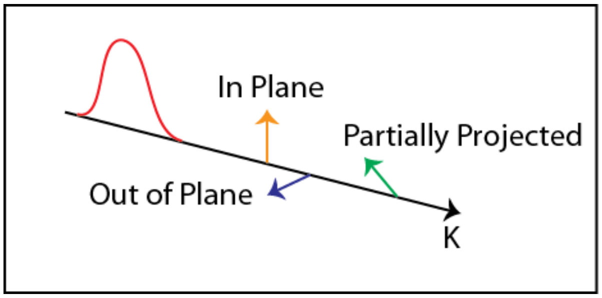

Figure 1.7 – Orientation of multiple dipoles relative to linearly polarized light pulse.

photoluminescence or absorption measurements between two orthogonally polarized EM fields in ordered systems, such as quantum wells [12], or molecules [13].

A sample can be described through a summation over the respective microscopic polarizations within the system:

$$\bar{\mu} = \int d\bar{r}\, \bar{r}\, \rho(\bar{r}) \tag{1.25}$$

with $\rho(\bar{r})$ representing the charge density of the system. The impingent field then interacts with the system through the interaction potential, as described by equation 1.22a:

$$V(t) = -\bar{\mu} \cdot \bar{E}(t) \tag{1.26}$$

The transition rate for a given two level simple system is given by:

$$w_{fi} = \frac{\pi}{2\hbar^2} |E_0|^2 |\mu_{fi}|^2 \left[\delta\left(\omega_{fi} - \omega\right) + \delta\left(\omega_{fi} + \omega\right)\right] \tag{1.27}$$

where μ_{fi} dictates the strength of the transition, or the dipole coupling strength:

$$\mu_{fi} = \langle f|\mu \cdot E|i\rangle\ . \tag{1.28}$$

As described previously, the expectation value for an operator is given through the trace of the density matrix, which for the macroscopic polarization of a sample within the dipole approximation in Hilbert space is given by:

$$P(t) = Tr(\mu\rho(t)). \tag{1.30}$$

The interest comes in the time dependence of the density matrix. What happens if multiple pulses are involved, such as in n-wave mixing. This requires the invocation of time-ordering.

1.2.2.4 – Time Ordering

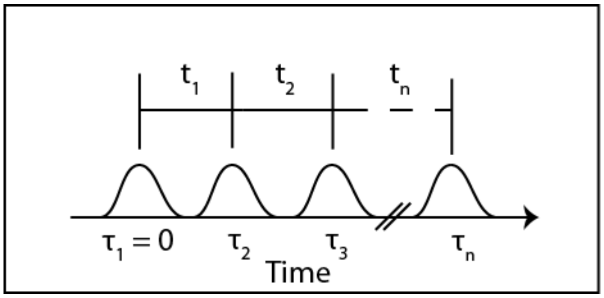

Figure 1.8 – Time ordering between incident light pulses

Each impingent field may have its own influence on the system. The field may interact with a material which is currently in a thermal equilibrium or it may reach a system that has been previously perturbed by another field. In other words, each field will create a polarization component whose sum will potentially comprise the emitted signal field time t later, as shown in Figure 1.8. In order to consider each individual field contribution within the interaction picture, one may expand the density matrix in terms of the time intervals between n-fields:

$$\rho(t) = \rho^{(0)}(-\infty) + \sum_{n=1}^{\infty} \rho^{(n)}(t) \qquad (1.31)$$

where $\rho^{(0)}$ represents the thermally populated pre-interaction density matrix and $\rho^{(n)}$ will interact with the nth electronic field through the interaction picture dipole operator:

$$P^{(n)}(t) = \langle \mu \rho^{(n)}(t) \rangle \qquad (1.32)$$

Taking the time intervals between electric fields to be those as described above we get an expression for the nth order polarization:

$$P^{(n)}(t_{n,} \dots, t_2, t_1) = -\left(-\frac{i}{\hbar}\right)^n$$

$$\int_0^\infty dt_n \dots \int_0^\infty dt_2 \int_0^\infty dt_1 \ E(r, t - t_n) E(r, t - t_n, \dots - t_2) \ E(r, t - t_n \dots - t_2 - t_1) \cdot$$

$$\langle \mu(t_n + \cdots + t_2 + \ t_1) \dots [u(t_2 + t_1), [u(t_1), [u(0), \rho(-\infty)] \dots]\rangle \qquad (1.33)$$

where the nth order response function, which describes the material contribution to the signal, is given by:

$$R^{(n)} = \ -\left(-\frac{i}{\hbar}\right)^n \langle \mu(t_n + \cdots + t_2 + \ t_1) \dots [\mu(t_2 + t_1), [\mu(t_1), [\mu(0), \rho(-\infty)] \dots]\rangle$$

(1.34)

The system is allowed to interact with each optical pulse through the interaction dipole operator. Each subsequent pulse generates a given influence on the polarization which radiates a field based on the final interaction given by:

$$\mu(t_n + \cdots + t_2 + \ t_1) \qquad (1.35)$$

1.2.2.5 – Rotating Wave Approximation

The expansion of the density matrix and subsequent description of the non-linear polarization leads to an over-abundance of contributions to the signal adding to the task of interpreting the result.[6, 7] In order to simplify the parameter space, one may invoke the rotating wave approximation (RWA). The E(t) field, as described in equation 1.8b, is composed of two components each capable of interacting through the field for a two level system [5]:

$$\langle 1|\mu \cdot E(t)|2\rangle = \hbar\mu E_0 \cos(\omega t) e^{-i\omega_0 t} \qquad (1.36a)$$

$$\langle 2|\mu \cdot E(t)|1\rangle = \hbar\mu E_0 \cos(\omega t) e^{i\omega_0 t} \qquad (1.36b)$$

where ω_0 is the transition frequency, ω the light frequency, and μ is the real valued magnitude of the transition dipole operator. The time dependence of the density matrix in terms of the coupling above is given through, in the interaction picture:

$$\frac{d\rho}{dt} = -\frac{i}{\hbar}[V_I(t), \rho(t)] \tag{1.37}$$

Taking the first term gives:

$$\dot{\rho}_{11} \sim \cos(\omega t)(e^{i\omega_0 t}\rho_{12} - e^{-i\omega_0 t}\rho_{21}) \tag{1.38a}$$

$$\dot{\rho}_{11} \sim \frac{1}{2}\left(e^{i\omega t} + e^{-i\omega t}\right)\left(e^{i\omega_0 t}\rho_{12} - e^{-i\omega_0 t}\rho_{21}\right). \tag{1.38b}$$

Expanding the electric field gives:

$$\dot{\rho}_{11} \sim e^{i(\omega_0+\omega)t}\rho_{12} - e^{-i(\omega_0-\omega)t}\rho_{21} + e^{i(\omega_0-\omega)t}\rho_{12} - e^{-i(\omega_0+\omega)t}\rho_{21}\,. \tag{1.39}$$

Assuming the exciting field is near or on resonance with the transition, or ω ~ ω_0, the $(\omega_0 + \omega)$ terms oscillate with a highly off-resonant frequency 2ω. These rapidly oscillating terms will be ignored, leaving:

$$\dot{\rho}_{11} \sim e^{i(\sim 0)t}\rho_{12} - e^{-i(\sim 0)t}\rho_{21} \tag{1.40a}$$

$$\dot{\rho}_{11} = i\frac{\mu E_0}{\hbar}(\rho_{12} - \rho_{21}). \tag{1.40b}$$

This applies to discussion of the response functions, both linear and non-linear as well. Within the RWA the highly off-resonant 2ω terms will be ignored throughout all contributions in the $P^{(n)}$ term shown in equation 1.33.

1.2.2.6 – Navigating Liouville Space: Two-Sided Feynman Diagrams

Admittedly, even with simplification through RWA, the higher order polarization and response functions involved in multi-wave mixing processes are numerous and complicated. Thankfully, Feynman provided an intuitive roadmap through Liouville space: the two-sided Feynman diagram.[6]

A two-sided Feynman diagram is shown in Figure 1.9. The diagram depicts the relative light-matter interactions pertinent to the nth order response in a given experiment for n-impingent electromagnetic fields. The left most side represents action on the KET, the right most side action on the BRA. Time-ordering is shown from bottom to top with each subsequent arrow representing a given light-matter interaction. The RWA manifests itself through the direction of the arrow, rightward pointing being the E contribution from the EM field, leftward being the E*. The emitted signal field is generally distinct from incident fields through a dashed line.

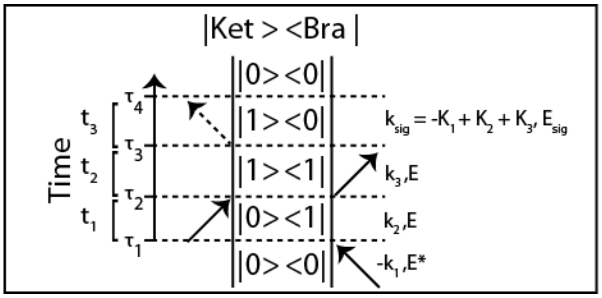

Figure 1.9 – An example two-sided Feynman diagram. Arrows represent components of the E-M field during light -matter interactions.

Physically, the manifestation of the rotating wave approximation is intuitive through Feynman diagrams. Imagine that the first interaction in the Feynman pathway in Figure 1.9 involved E (+k$_1$) acting on the BRA. While this indeed represents a potential pathway mathematically, the first field-matter interaction would depopulate the ground state through emission which is an unphysical result [6].

1.3 – Linear Spectroscopy

Linear spectroscopy has become ubiquitous in the physical sciences. Whether in the form of steady-state absorbance and photoluminescence or time-resolved, linear spectroscopy provides a window into concentrations, reaction kinetics, and population lifetimes. Techniques from total internal reflection microscopy to High Performance Liquid Chromatography with UV-VIS detection all make use of the linear response of a material to a field.

1.3.1 – 1st order Polarization and Response

The contributions to the first order response in the dipole approximation, given through the trace of the density matrix and the dipole operator are:

$$R^{(1)}(t) \sim -i\langle \mu(t_1)[u(0), \rho(-\infty)]\rangle. \tag{1.41}$$

Invoking the rotating wave approximation, the only two terms surviving are shown in the two sided-Feynman diagram in Figure 1.10. The observed absorption is a direct result of the self-action of the emitted signal field and the E* of the incident beam [7]:

$$A^{(1)} \sim Im \int_{-\infty}^{\infty} dt\, E^*(t)\ P^{(1)}(t) \tag{1.42}$$

which can be normalized to the incident beam intensity giving the absorbance:

$$A^{(1)} \sim Im \int_{-\infty}^{\infty} dt\, E^*(t)\ P^{(1)}(t)\ /\ \int_{-\infty}^{\infty} dt\ |E(t)|^2 \tag{1.43}$$

It is interference caused by the emitted radiation of the oscillating electronic structure of the sample which is 90° phase-lagged to the incident field.

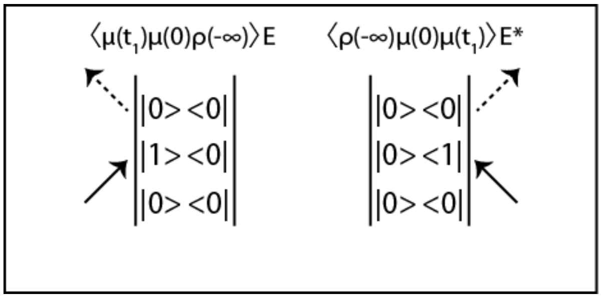

Figure 1.10 – Two Feynman pathways contributing to linear absorption spectra.

1.3.2 – Beers Law and Optical Density

The practical description of linear absorption is that of optical density (OD):

$$OD = -\log_{10}(\frac{I}{I_0}) \tag{1.44}$$

where *I* is the intensity of the attenuated beam and I_0 is the intensity of the beam pre-sample. The form is similar to that of equation 1.43. The common application for linear absorption systems beyond the qualitative analysis of absorbing analytes within a sample is the concentration of a liquid system. The concentration of a given non-turbid, non-scattering solution can be determined simply, assuming the extinction coefficient for the system is known, through the Beer – Lambert law:

> Tip:
>
> An OD of ~100 – 200 mOD at band-edge is best as increased OD will lead to increased effect of the excitation gradient across the sample! Remember, an OD of 1 means a pump beam will be ~ 10 times weaker at the back-face of the sample!

$$A = \varepsilon CL \tag{1.45}$$

where C is the concentration of the sample, A the 'absorbance', L the path length and ε the extinction coefficient.

1.3.3 – A Brief Aside on Spectral Line Shape

A spectroscopic measurement is performed, often, in the hopes of discerning some form of information based on a given sample or reaction. In the visible, this information can aid in the understanding of the relative electronic environment of the system. One aims to map the potential energy surface, or the probability, against a given observable coordinate, as shown in Figure 1.11. In infrared spectroscopy this could amount to any given vibrational mode. Electronic spectroscopy, as described previously, indirectly measures the polarization of the sample through perturbed electronic populations. However, spectroscopy does not directly measure the material itself; it merely measures the influence of the material on the electric field. The interpretation of the signal requires modelling. Modelling and spectroscopy go hand-in-hand. The following section will briefly outline the various theoretical approaches to mapping observed spectra onto some desired coordinate through fluctuations in the energy gap as a function of frequency.

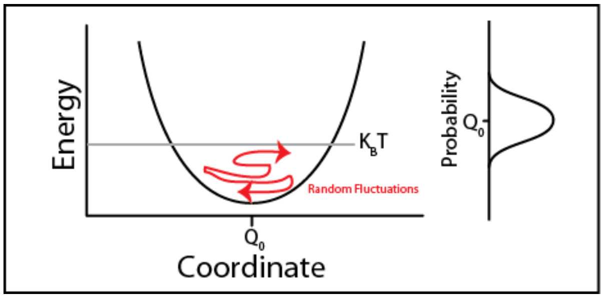

Figure 1.11 – Potential energy surface projection about a given coordinate. Random fluctuations generate a Gaussian distribution in probability.

1.3.3.1 – Correlation Functions and Spectroscopy

An electromagnetic field creates some coherent response in a material through coupling to the dipole operator which manifests itself in an oscillating polarization, as shown in equation 1.33.

This influence may be mapped through the appropriate response function in the eigenestate (wave function) representation if the system is well known. In a perfect model system, completely isolated from all influences of its local

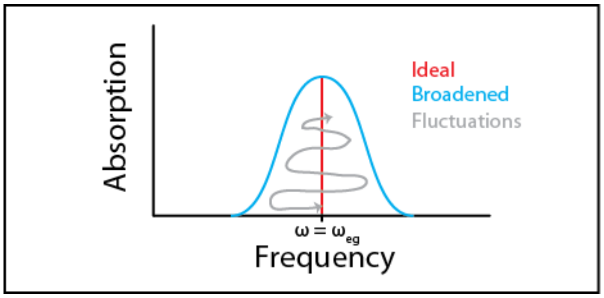

Figure 1.12 – Ideal delta-function lineshape broadened through random fluctuations within the environment.

environment, such as an ideal gas, the transition frequency would be a delta function at the energy gap ignoring Doppler broadening and relaxation, as shown in Figure 1.12. This result is inferred through equation 1.27. However, most systems have relaxation dynamics and structural asymmetries. Similarly, local environments, especially in complex condensed phase systems at thermal equilibrium, have dynamically evolving environments.[7, 14] This evolution may arise from collisions in the gas phase to interactions with the bath or local environmental asymmetries in the condensed phase. All of these processes influence the observed spectra, manifesting themselves in a broadening of the spectral lineshape, as shown in Figure 1.12. The end goal is to map the effects of these fluctuations onto the response of the system itself to discern information regarding the desired coordinate. In other words, one aims to correlate the fluctuations within the environment to the system, and vice-versa, through the narrowing or broadening of the spectrum.

In order to begin, consider the time dependent autocorrelation function:

$$C_{AA}(t,t') \equiv \langle A(t)A(t') \rangle \tag{1.46}$$

which maps the relation between an observable in two moments in time[7, 14]. The quantum canonical time-correlation function for an equilibrium distribution is given by:

$$C_{AA}(t,t') = \langle \frac{e^{\frac{-H}{K_bT}}}{Z} A(t)A(t') \rangle \qquad (1.47)$$

where Z is the canonical partition function. This leads to the time dependent dipole-dipole correlation function:

$$C_{uu}(t) = \langle \mu(t)\mu(0) \rangle \qquad (1.48)$$

the Fourier transform of which gives the absorption and emission spectra, within the Frank-Condon approximation:

$$\sigma(\omega) = \frac{1}{2\pi} \int_{-\infty}^{\infty} dt\, e^{-i\omega t} \langle \mu(t)\mu(0) \rangle \qquad (1.49)$$

Equation 1.48 bears a striking resembles to the previously derived equation for the linear polarization.

1.3.3.2 – Stochastic Processes

Without a complete knowledge of the eigenstates of the system, the development of an appropriate model is required. Consider the parabolic free energy surface shown in Figure 1.11. At room temperature the system will be thermally populated up to k_BT, leading to a distribution along the potential energy surface (PES). This provides a large configuration space, or phase space, any given system may sample over a given time. Depending on the topography surrounding the mimima of the surface, the system may be able to rapidly sample the phase space or may be hindered through potential barriers. In order to map the thermal distribution, a correlation between the transition frequency and the time evolution of the thermal distribution needs to be determined, or, an energy-gap correlation function [7, 14]:

$$C_{eg}(t) = \langle \omega_{eg}(t)\omega_{eg}(0) \rangle. \qquad (1.50)$$

The fluctuation of the system about the minima of the PES will lead to fluctuations in the energy-gap. If these fluctuations occur stochastically about the mean defined by the minimum of the well, the system will follow Gaussian statistics which is the central limit theorem: a large number of stochastic processes occurring about a mean will follow a Gaussian distribution about the mean[14]. This will greatly simplify the cumulant expansion of the dephasing function later on.

1.3.3.3 – The Displaced Harmonic Oscillator Picture

In order to develop an energy-gap correlation function, an appropriate model Hamiltonian must first be discussed. The displaced harmonic oscillator (DHO) picture, as shown in Figure 1.13, is a common model used throughout spectroscopy.[7] Much like the development of the interaction picture wherein the explicit time dependence of the system lay with the weak perturbation, the DHO approach can be used to modulate the energy gap based on interactions with a given set of harmonic oscillators acting as a bath, as expressed through an energy-gap Hamiltonian [7, 14]:

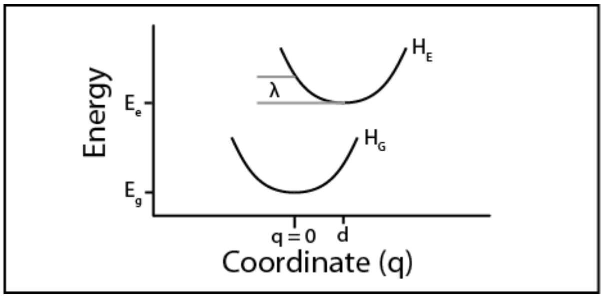

Figure 1.13 – Simple displaced harmonic oscillator surfaces. Vibrational progressions not shown.

$$H = \hbar\omega_{eg} + H_{eg} + 2H_g \tag{1.51a}$$

$$H_{eg} = -2\hbar\omega_0 dq + \lambda \tag{1.51b}$$

where q is the coordinate of interest, d the displacement between oscillators, and λ is the reorganization energy. When considering equation 1.51a in the form of a system bath Hamiltonian:

$$H = H_e + H_{SB} + H_B \tag{1.52}$$

one may take the ground-state oscillator, H_g, as the bath with the energy gap Hamiltonian, H_{eg}, representing the time dependent coupling between the electronic Hamiltonian and the bath [7, 15]:

$$H_e(t) = H_g + H_{eg}(t) \tag{1.53}$$

The time dependence of the energy gap Hamiltonian is now given by:

$$H_{eg}(t) = e^{iH_g t} H_{eg} e^{-iH_g t} \tag{1.54}$$

which leads to the energy-gap dephasing function:

$$F(t) = \langle e^{-\frac{i}{\hbar}\int_0^t H_{eg}(t)} \rangle \tag{1.55}$$

Taking the time-ordered cumulant expansion, which, due to the Gaussian statistics discussed earlier may be truncated at the second order, the dephasing function leads to the dipole correlation function:

$$C_{uu}(t) = \left|\mu_{eg}\right|^2 e^{\frac{-i(\Delta E_{eg}+\lambda)t}{\hbar}} e^{-g(t)}. \tag{1.56}$$

Fourier transformation of equation 1.56 leads to the emission and absorption spectra, with the Stokes shift given by 2λ. The final term, $g(t)$, is a so-called lineshape function:

$$g(t) = \int_0^t d\tau_2 \int_0^{\tau_2} d\tau_1 \langle \delta\omega_{eg}(\tau_2 - \tau_1)\delta\omega_{eg}(0) \rangle \tag{1.57}$$

where:

$$C_{eg} = \langle \delta\omega_{eg}(\tau_2 - \tau_1)\delta\omega_{eg}(0)\rangle \qquad (1.58)$$

is the energy-gap correlation function. In other words, the relative treatment of the bath interactions and their subsequent effect on the dipole-correlation function (spectral broadening and phonon-progressions) is given through the lineshape function.

The lineshape function may also be used in the calculation of a given response function. Taking 1.56, the linear response would be given by:

$$R^{(1)}(t) = -i\,\left|\mu_{eg}\right|^2 e^{\frac{-i(\Delta E_{eg}+\lambda)t}{\hbar}}\, e^{-g(t)} \qquad (1.59)$$

which allows for the calculation of complicated condensed phase linear and non-linear spectra through various system-bath treatments, without a priori knowledge of the eigenstates of the system.

1.3.3.4 – A Practical Description of Broadening

The general recipe for modelling a given spectra starts with the energy-gap correlation function as it, hopefully, contains all the pertinent fluctuations. Whether the model uses coupling to a single bath mode or a continuum of modes, as in the multimode Brownian oscillator model, the processes is the same. Basically, one calculates the energy-gap correlation function, C_{eg}, for a given system-bath Hamiltonian. The correlation function then feeds into equation 1.56 to give the lineshape function. The lineshape function then feeds the dipole-dipole correlation function, which, when Fourier transformed, provides the absorption and emission lineshapes.[7]

A particular feature pertinent to the discussion of spectral broadening is the correlation time, τ_c, of a given time-dependent correlation function [14]:

$$\tau_c = -\frac{1}{\langle \delta A^2 \rangle} \int_0^\infty \langle \delta A(t) \delta A(0) \rangle \qquad (1.60)$$

which is the characteristic time for the time-correlation function (as given by equation 1.45) to decay to 0. This correlation time is a figure-of-merit for a given stochastic processes' influence on the spectral lineshape. For example, if a system undergoes multiple collisions or fluctuations in a short period of time, the correlation time will be quite short, as in the condensed phase. If the system undergoes no collisions, or few collisions, the subsequent correlation time will be long, as in the gas-phase. The importance of the correlation time comes when one considers the breadth of the configurations space a given sample may have, as given by the full width at half-maximum (FWHM) of the probability distribution shown in Figure 1.11. It is the relative ratio between the configuration space and the correlation time which dictates the homogeneity of the spectral linewidth.

Consider the Kubo lineshape function [6, 14]:

$$g(t) = \Delta^2 \tau_c^2 \left[e^{\frac{-t}{\tau_c}} + \frac{t}{\tau_c} - 1 \right] \qquad (1.61)$$

where Δ is the FWHM of the probability distribution (configuration space) of a fluctuating system and t is the given sampling time. For very long correlation times, the lineshape reduces to:

$$g(t) = \frac{\Delta^2 t^2}{2} \qquad (1.62)$$

giving an inhomogenously broadened, Gaussian spectrum covering the full configuration space:

$$\sigma(\omega) \sim |\mu|^2 e^{-\frac{(\omega - \langle\omega\rangle)^2}{2\Delta^2}} \tag{1.63}$$

known as the inhomogeneous limit. In the event of short correlation times, the lineshape function becomes:

$$g(t) = \Delta^2 \tau_c^2 t \tag{1.64}$$

which leads to a homogenously broadened, Lorentzian lineshape given by:

$$\sigma(\omega) \sim \frac{1}{(\omega - \langle\omega\rangle^2) - \frac{1}{T_2^2}} \tag{1.65}$$

where T_2 maps the relation between the configuration space and the coherence time, or :

$$T_2 = \Delta^2 \tau_c \tag{1.66}$$

Generally, a real-world system will exist in between these two limits, in a region where the correlation time decays on the order of the sampling time of the configuration space by the system. In other-words, one (or many) homogenously broadened components spectrally diffuse about the configuration space with time. This leads to a Voigt lineshape given by the convolution of the homogeneous and inhomogeneous limits, known as the spectral diffusion regime [6, 7]:

$$\sigma(\omega) \sim \frac{1}{(\omega - \langle\omega\rangle^2) - \frac{1}{T_2^2}} \, e^{-\frac{(\omega - \langle\omega\rangle)^2}{2\Delta^2}} \tag{1.67}$$

Non-linear spectroscopy, through photon-echo or, more immediately, two-dimensional spectroscopy, can provide information regarding the relative contributions of the homogenous and inhomogeneous broadening on a given spectrum. Photon-echo experiments, based on the relative amplitudes of the initial peak and the shifted peak, provide information on the combined influence of relaxation dynamics and correlation times as they directly affect the amplitude of the photon-echo peak.[16] Two-dimensional spectroscopy, by the very nature of its sampling methods, can directly monitor spectral diffusion through sweeping population time in any given experiment.[17]

1.3.3.8 – Relaxation Dynamics and Lineshape

The discussion surrounding lineshape has thus far centered on the stochastic fluctuations of the system and the bath, however, population dynamics also play a role in the final absorption lineshape. Equation 1.64 provides the linewidth for the homogenous limit. Of particular interest is the timescale given by T_2. This characteristic timescale contains all the potential dephasing mechanisms within a system, namely population dynamics and the familiar pure-dephasing mechanisms (collisions and the like):

$$T_2 = T_1 + T_2^* \tag{1.68}$$

where T_2^* is the pure dephasing time. Population dynamics may be split into two contributions: radiative relaxation and non-radiative relaxation:

$$T_1 = T_R + T_{NR}. \tag{1.69}$$

These relaxation dynamics manifest themselves in the lineshape through broadening the homogenous linewidth.

1.3.3.9 – Marcus-Jortner Electron Transfer Theory

The Marcus-Jortner electron transfer (ET) theory is an extension of the DHO models discussed above wherein the oscillators act as electron donors and acceptors to model the long range coupling of electronic charge distribution within the system.[14, 18-20] This particular approach to modelling both spectral lineshape and its temperature dependence will play a significant role in the discussion of steady-state nanocrystal surface emission in chapter 2. Like in the DHO model, the Marcus-Jortner ET theory minimally comprises two displaced oscillators with a given reorganization energy and displacement across a coordinate, as shown in Figure 1.14. The system coordinate is often taken to reflect the organization of the solvent as the solvent must re-arrange to accommodate accumulating negative charge at the acceptor center. However, as in all DHO models, the coordinate can be taken in a form that best represents the information of interest.

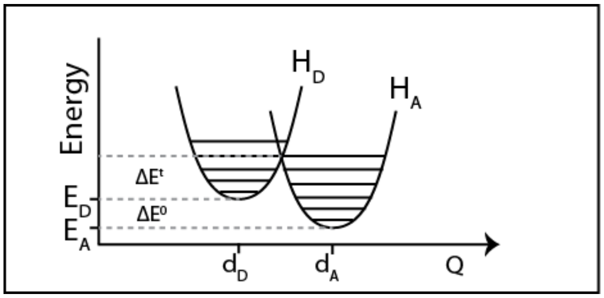

Figure 1.14 – Marcus-Jortner ET surfaces with vibrational modes represented.

The methodology remains the same, determine an appropriate Hamiltonian, derive the appropriate ‘picture’ (separation of the Hamiltonian), determine the correlation function, solve the lineshape function and apply it to a Fermi’s Golden-Rule expression. To begin, the Hamiltonian for the system described in Figure 1.14**:**

$$H = H_0 + V \tag{1.70a}$$

$$H_0 = |D\rangle H_D \langle D| + |A\rangle H_A \langle A| \tag{1.70b}$$

Invoking a Golden Rule expression using the energy-gap Hamiltonian:

$$w_{ET} = \frac{|J|^2}{\hbar^2} \int_{-\infty}^{\infty} dt e^{-\frac{i\Delta E_{AD} t}{\hbar}} e^{-\frac{i\lambda t}{\hbar} - g(t)} \tag{1.71}$$

where J gives the coupling strength between surfaces based on distance between donor and acceptor orbitals:

$$J = J_0 e^{\frac{R - R_0}{K_B T}} \tag{1.72}$$

allows for the description of the electron transfer rate in terms of the now-familiar lineshape function, g(t). The g(t) used depends on the treatment of interest. Taking g(t) to include coupling through Harmonic modes leads to a jth vibrational-mode and tunnelling-assisted electron transfer rate given by:

$$w_{ET} = \frac{|J|^2}{\hbar} \sqrt{\frac{\pi}{\lambda_0 K_B T}} \sum_{j=0}^{\infty} \left(\frac{e^{-D}}{j!} D^j \right) e^{\frac{-\left(\Delta G^0 + \lambda_0 + j\hbar\omega_0\right)^2}{4\lambda_0 K_B T}} \tag{1.73}$$

where λ_0 is the reorganization energy given through the lowest-frequency vibrational mode, ΔG^0 the Gibbs energy between donor and acceptor (related to the activation energy for transfer as shown in Figure 1.14) and D is the displacement between surfaces:

$$D = (d_A - d_D)^2 \tag{1.74}$$

This tunnelling assisted temperature dependence of the transfer rate between displaced harmonic oscillators was extended to describe the temperature dependence of the surface emission of colloidal quantum dots[21].

1.3.4 – Experimental Design

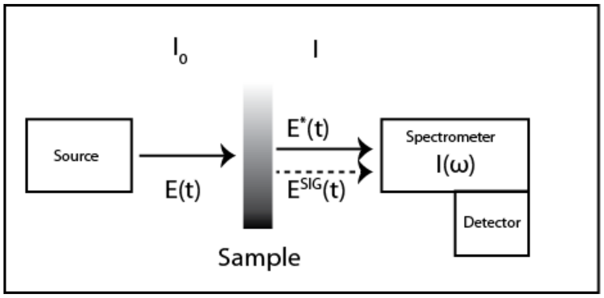

Figure 1.15 – Generic Linear absorption setup

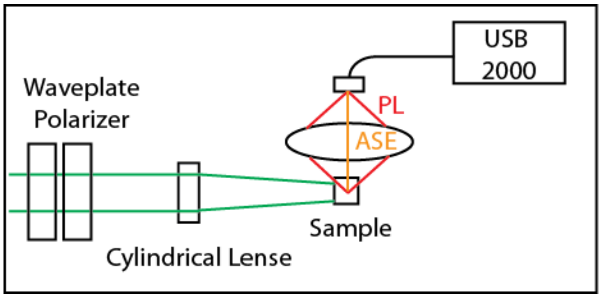

Figure 1.16 – Experimental setup for ASE/PL measurements.

Linear spectrometers are stable, commercial devices available from a myriad of sources with a vast array of complexity and cost. They generally employ a broadband, continuous-wave light source and some tuned monochrometer or charge-coupled device (CCD) in order to detect in the frequency domain as shown in Figure 1.15. The steady-state spectrometer used throughout this dissertation was a Cary UV-VIS spectrometer. Photoluminescence (PL) and Photoluminescence Excitation (PLE) measurements were taken using a Fluromax, generally through high energy, 3.1 eV, excitation in the case of PL. In the case of solid-state amplified stimulated emission (ASE) and photoluminescence measurements presented in the dissertation, optical layout is shown in Figure 1.16, excitation was achieved through an OPA tuned resonant to the transition of interest. It was then compressed through a folded prism compressor pair and focused into a strip via a cylindrical lens onto the sample. The resultant PL, SE, and ASE were collected via a 3.5” collection lens, coupled into a fiber, and subsequently detected using an Ocean Optics USB 2000 spectrometer. Polarization and fluence were controlled via wave plate-polarizer pairs.

1.3.4.1 – Temperature Dependent Linear Spectroscopy

As mentioned previously, thermal populations play a large role in spectroscopy. At room temperature, for example, k_BT is roughly 20-30 meV, leading to an inherent distribution amongst states whose separation is less than 30 meV. A large component in spectral line shape is both the inherent homogenous line width present due to relaxation times and pure dephasing as well as inhomogeneous broadening. Lowering temperature may sharpen spectral features through limiting the contributions of given vibrational modes as seen in the DHO and Marcus-Jortner pictures discussed above.

The temperature dependent experiments throughout the dissertation were performed using a Janis Flow Cryostat down to liquid He temperatures paired to either a Cary UV-Vis spectrometer or a Fluromax with excitation energies generally at 3.1 eV, in general.

1.4 – Non-Linear Spectroscopy

Whereas linear spectroscopy involves a single weak light-matter interaction, non-linear spectroscopy involves many, or intense, light-matter interactions. As with the linear spectroscopy, the polarization may be described in terms of response functions. Similarly, the oscillating 3rd polarization emits a signal field which is a manifestation of the multiple field-matter interactions involved. However, due to the multiple-interaction nature of n-wave mixing, the subtleties of the relative interactions lead to multiple potential detection mechanisms.

1.4.1 – 3rd Order Polarization and Response

The third order polarization is given, as inferred through equation 1.33, by:

$$P^{(3)}(t_3, t_2, t_1) =$$

$$\int_0^\infty dt_3 \int_0^\infty dt_2 \int_0^\infty dt_1 \; E(r, t - t_3) E(r, t - t_3 - t_2) \; E(r, t - t_3 - t_2 - t_1) \cdot$$

$$\sum_n R_n \,(t_3, t_2, t_1) \qquad (1.75)$$

The eight general contributions to the 3rd order response for a two-level model, as shown in Figure 1.17 (below), within the RWA and interaction picture are [6, 7]:

$$R_{(1)} \sim \langle \mu(t_3 + t_2 + t_{1)} \mu(0) \rho(-\infty) \mu(t_1) \mu(t_1 + t_2) \rangle \text{ + C.C.} \qquad (1.76a)$$

$$R_{(2)} \sim \langle \mu(t_3 + t_2 + t_{1)} \mu(t_1) \rho(-\infty) \mu(0) \mu(t_1 + t_2) \rangle \text{ + C.C.} \qquad (1.76b)$$

$$R_{(3)} \sim \langle \mu(t_3 + t_2 + t_{1)} \mu(t_1 + t_2) \rho(-\infty) \mu(0) \mu(t_1) \rangle \text{ + C.C.} \qquad (1.76c)$$

$$R_{(4)} \sim \langle \mu(t_3 + t_2 + t_{1)} \mu(t_1 + t_2) \mu(t_1) \mu(0) \rho(-\infty) \rangle \text{ + C.C.} \qquad (1.76d)$$

As with the linear response (equation 1.59), the 3rd order response functions may also be described in terms of an energy-gap correlation function and subsequent lineshape functions.[6, 7] Taking the first response function as an example:

$$R_{(1)} = -\left(\frac{i}{\hbar}\right)^3 \mu^4 e^{-i\omega(t_1+t_3)} e^{-g(t_1)-g(t_2)-g(t_3)+g(t_1+t_2)-g(t_1+t_2+t_3)} \qquad (1.77)$$

which, when combined with the various levels of system-bath Hamiltonians discussed previously, allows for the simulation of increasingly complex systems, such as those in the condensed phase. This is again without knowledge as to the exact solutions of the system .[7]

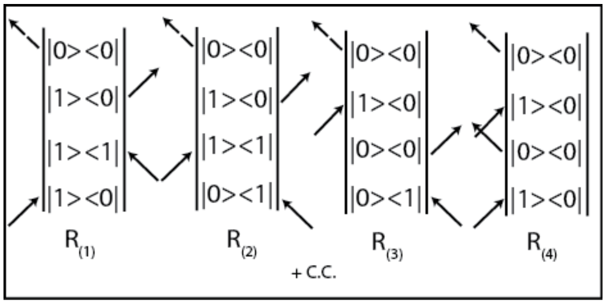

Figure 1.17 – Four of the eight contributing Feynman pathways in a 4-wave mixing non-linear experiment on a two level system

Of practical importance, when considering the multitude of Feynman pathways contributing to a given signal, are the incident electric fields themselves. A plane-wave electric field travels along a given wave-vector with a given phase:

$$E(t) = E_0(t)\cos(\vec{k} \cdot \vec{r} - \omega t + \varphi) \qquad (1.78)$$

which will directly influence the emitted signal field, shown through equation 1.6. The signal field, which follows the wave-vector $\vec{k}_{sig}$, will be emitted in phase-matched direction of the contributing pump pulses to the non-linear polarization in the RWA:

$$\vec{k}_{sig} = \pm\vec{k}_1 \pm \vec{k}_2 \pm \vec{k}_3 \qquad (1.79)$$

which, in the case of $R_{(1)}$ from equation 1.76a, would be:

$$\vec{k}_{sig(R^1)} = \vec{k}_1 - \vec{k}_2 + \vec{k}_3 \qquad (1.80)$$

All contributing Feynman pathways will produce a signal in their given phase-matched direction as dictated by the sum of the electric field contributions to the

Feynman pathway in a given experiment. This leads to a practical method for separating the given contributions through the non-collinear pumping of a sample. Through proper placement of a detector, or mask, the given signal of interest may be detected through understanding the wave-vector of the desired signal.[6, 17]

Two prominent non-collinear geometries are the box-CARS geometry, named from its use in Coherent Anti-Stokes Raman Spectroscopy, and the pump-probe geometry, as shown in Figure 1.18.[6] Box-CARS involves three entirely non-collinear pulses each with their own independent wave-vector. When mapped in a plane, the three pump pulses appear to form the outer quadrants of a square, with the emitted signal field making the fourth. This non-collinear separation of wave-vectors is often used in photon-echo experiments,[16, 22] as well as for background-free two-dimensional electronic spectroscopy.[17] Pump-probe geometry, however, makes use of collinear pumping. In other words, the wavevectors $\vec{k}_1$ and $\vec{k}_2$ follow the same trajectory which herein will be referred to as $\vec{k}_{pump}$ with $\vec{k}_3$ and $\vec{k}_{sig}$ following $\vec{k}_{probe}$. It is this phase-matching condition which leads to the self-acted signal field, removing requirement of a local oscillator for detection.

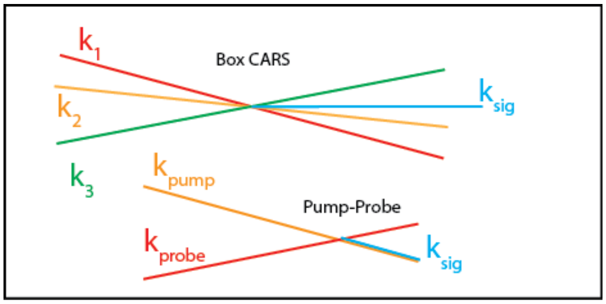

Figure 1.18 – Wave-vectors and phase matching for non-collinear pumping schemes

1.4.2 – Pump-Probe Spectroscopy

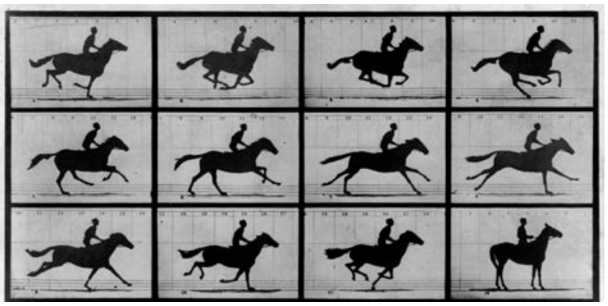

Figure 1.19 - "The Horse In Motion" by Eadweard Muybridge (1878 - Wiki Commons)

The development of pump-probe spectroscopic techniques followed the advent of pulsed laser sources. Through perturbing a sample with a varying intensity laser pulse, and subsequently probing with another, one can derive dynamical data through changes in the respective absorptive spectra as a function of time. The resolution with which one can accurately extract dynamic signals is, in a large fashion, dictated by the temporal duration of the pump and probe pulses. In some respects, the pump-probe response is analogous to a film reel. Consider the first live action movie “The Horse in Motion” by Eadweard Muybride. A camera was used to take multiple frames in quick succession of a horse in a gallop, each frame representing a different state of the horses run at a given time (Figure 1.19). By stringing these photographs together and playing them in quick succession the horses gallop was reproduced. However, both by watching the horse in gallop and the movie itself one cannot make the unique distinction that the horses’ four hoofs were ever off the ground. Only by examining the individual frames with sufficient temporal resolution can one be sure.

Pump-probe spectroscopy is a $\chi^{(3)}$ technique using the pump-probe geometry, as described above. The resultant $P^{(3)}$ and its emitted signal field manifest themselves as self-action with the probe beam, much like in linear spectroscopy. This self-action removes the requirement of a local oscillator as in other $\chi^{(3)}$ experiments, such as photon echo. This unique geometry provides direct measurement of the relative excited state populations of a given sample. The three contributing Feynman diagrams are shown in Figure 1.20 for a minimal 3-level model. The resultant pathways are excited state absorption, stimulated emission and ground state bleach. Not pictured are the complex conjugates.

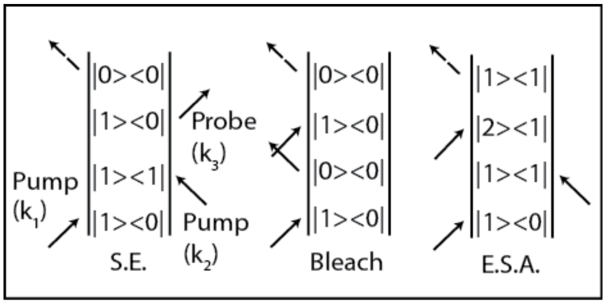

Figure 1.20 – Three major contributing Feynman pathways to the pump-probe signal

1.4.2.1 – ΔOD and OD_{NL}

While the Liouville and Feynman descriptions for non-linear spectroscopy provide an understanding toward the origins of signals in terms of the respective light-matter interactions, the more practical experimental description is that of optical density (OD). As described in section 1.3.2, linear optical density (OD_0), as measured by attenuation of light transmitted through a sample, is a steady state description of the relative optical transitions within a system. Pump-probe spectroscopy, however, is the study of dynamics through the change in optical density (ΔOD) of a probe beam through a sample as influenced by a pump pulse. In the case of ratiometric detection equation 1.44 becomes:

$$\Delta OD = OD^{ON} - OD^{OFF} \tag{1.81a}$$

$$\Delta OD = \left(-\log_{10}\left(\frac{I^{ON}}{I^{Ref}}\right)\right) - \left(-\log_{10}\left(\frac{I^{OFF}}{I^{Ref}}\right)\right) \tag{1.81b}$$

for the pumped (OD^{ON}) and unperturbed (OD^{OFF}) samples respectively. I^{Ref} is included to compensate for intensity fluctuations within the probe beam itself. The influence of the pump on the ΔOD signal manifests itself in slight changes in the transmission of the probe. As described above, the three primary contributions to the pump-probe signal are absorption (bleach), stimulated emission, and excited state absorption.

Optical bleach monitors the temporal evolution of a given transitions excited state population through the attenuated absorption (or increased transmission) of the probe due to decreased ground state population available in the pumped sample, as shown in Figure 1.21. The excited sample becomes decreasingly transparent to the probe as the excited state population relaxes to ground state. State filling dynamics and hot charge carrier relaxation may be monitored directly through transient bleach dynamics, a topic which will be discussed in chapters 2 - 5.

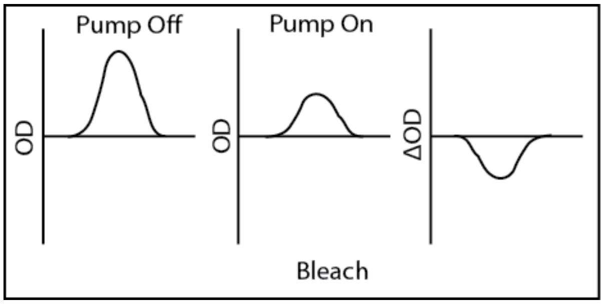

Figure 1.21 - Optically exiting the sample reduces available ground state population for absorption, lowering the apparent optical density.

Excited state absorption (ESA), as shown in figure 1.22, arises in the event of a resonant transition between an existing excited population (created by the pump interaction) and a higher excited state. ESA, depending on energy, may manifest itself in the form of attenuated bleach (if the excited state and ground state absorptions are near-resonant) or a positive going signal (if ground and excited state absorptions are sufficiently well separated).

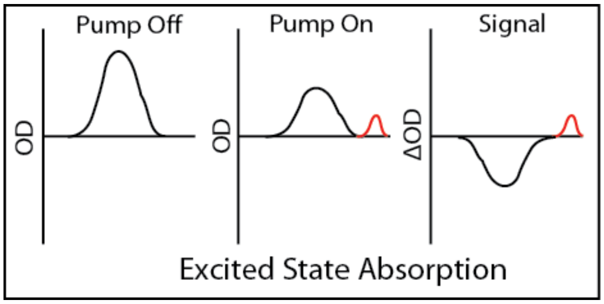

Figure 1.22 – Excited state population created through optical pumping is promoted to a higher energetic state through interaction with the probe.

ESA will play a critical role in the description of optical gain and multiexcitonic interactions further in the dissertation. Broadly, the ESA may arise due to intrinsic electronic structure or level shifting through Stark like effects.[23]

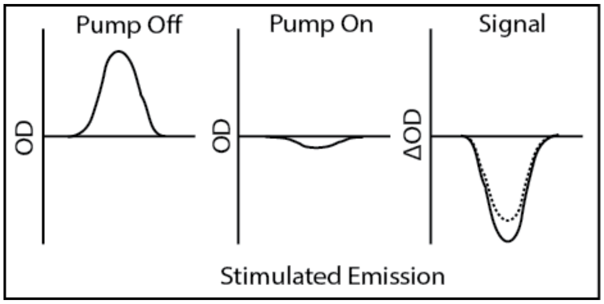

Figure 1.23 – Population inversion caused by pump pulse leads to stimulated emission seeded by probe

Stimulated emission, in terms of ΔOD, can be seen as an increase in the intensity of the probe above and beyond the fields' initial intensity. This manifests itself in a ΔOD signal which exceeds the conceivably maximum absorption of the sample: OD_0, as shown in Figure 1.23. When compared against the steady-state absorption spectrum, OD_0 as described in equation 1.44, which defines the theoretical maximum absorption, the stimulated emission intensity may be quantified. This comparison leads to a description of the non-linear spectrum, or OD_{NL} discussed later.

1.4.2.2 – Experimental Design

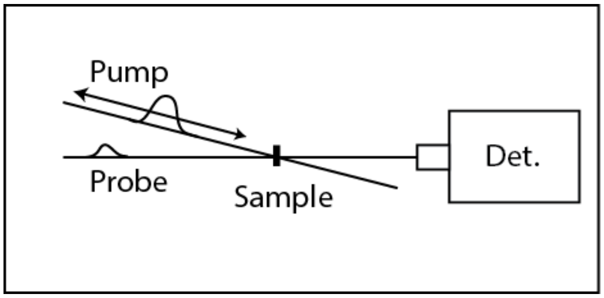

Figure 1.24 – Generic pump-probe design

The various pump-probe spectroscopic designs, at their core, share the same few components (Figure 1.24): a pump source, a probe source, some detector, and some form of temporal delay. With non-linear spectroscopies, the complexity of design is as vast as one's imagination. For example, ultrafast electron diffraction invokes a laser pulse as a pump to create some perturbation and subsequently probes the structural dynamics through changes in diffraction patterns of a compressed electron bunch.[24] In the case of femtosecond pump-probe transient absorption optical spectroscopy a pump creates a perturbation either through exciting a vibrational, rotational, or electronic transition, depending on the resonant frequency of the transition, and the often less intense probe pulse then interacts with the excited sample being absorbed and thereby attenuated.[7]

The purpose of the following section is to give a brief description of typical experimental considerations when developing pump-probe spectroscopic instrumentation as well as outline the specific system used throughout the dissertation.

1.4.2.2.1 – The Pump: Multicolour sources

Often, when dealing with femtosecond laser spectroscopy, an experiment is dictated by available light-sources in lieu of appropriate excitation conditions. The excitation domains of the commonly used titanium: sapphire laser lay roughly in the windows of 800 nm, 400 nm, and 266 nm with the fundamental, second, and third harmonic respectively. In order to excite, and subsequently examine, the various transitions and dynamics of a given material one requires fully tunable sources across a broad region of interest with femtosecond pulse duration.

Tip:

The number of variables can be overwhelming but remember this:

Space and Time

you can do an auto-correlation you can do a cross-correlation you can align an OPA you can do a Pump/Probe experiment. It is all just space and time.

1.4.2.2.2 – Optical Parametric Amplifiers

Optical parametric generation provided respite from the tedious operation of organic dye lasers as tunable pump-sources. Through the development of optical parametric amplifiers (OPA) and oscillators (OPO), readily available, simple, high power, tunable light sources allowed spectroscopists a new degree in freedom when exploring parameter space.[9] The following will focus mainly on the development of a non-collinear optical parametric amplifier used later in the dissertation for the two-dimensional electronic spectrometer.

Optical parametric amplification relies on the momentum conservation (phase matching) between the fast and slow axes of a birefringent crystal [8, 9]:

$$\Delta k_{p,i+s} = 0 \tag{1.82a}$$

$$k_p = k_i + k_s \tag{1.82b}$$

where k_n is the wave-vector of the pump, idler, or signal respectively. Casting the above in terms of the index of refraction leaves:

$$n_p = \frac{n_i \omega_i + n_s \omega_s}{\omega_p} \tag{1.83}$$

This provides two phase-matching conditions depending on the relative incident polarizations of the optical beams, and therefore the relative orientation about the fast and slow axis of the crystal for the mixing components:

$$Type\ I \equiv o_i + o_s \rightarrow e_p \tag{1.84a}$$

$$Type\ II(a) \equiv o_s + e_i \rightarrow e_p \tag{1.84b}$$

$$Type\ II(b) \equiv e_s + o_i \rightarrow e_p \tag{1.84c}$$

These phase-matching conditions apply to many discussions of wave mixing in anisotropic material, such as BBO. The appropriate phase-matching condition depends on the intended use. Also, an understanding of the relative contributions is essential in designing even a doubling line for a pump-probe experiment. The 400 nm field will exit the crystal orthogonally polarized to the incident 800 nm line. In order to ensure the exiting 400 nm beam is appropriately polarized (orthogonally) relative to the probe being used, the 800 nm pump line must be oriented parallel to the probe beam. For development of the non-collinear optical parametric amplifier (NOPA), however, the non-linear mixing software SNLO was used in order to optimize pump-intensities, crystal angles, and thicknesses.[19]

A pump field amplifies a signal (seed) field while generating a third field, the idler. The OPA process can be thought of as the inverse of sum frequency generation where two photons of different lower energies create a single photon of higher energy. This leads to the degeneracy condition:

$$\omega_p = \omega_s + \omega_i \tag{1.85}$$

where the pump frequency dictates the maximum tunable range for both signal and idler. Pumping a BBO crystal with the fundamental of a titanium:sapphire laser at 800 nm provides a degeneracy of $\frac{1}{2}\omega_p = 1600\, nm$. By convention, the signal field is considered to be the higher energy field (from ~ 900 nm to 1600 nm) and the idler field the lower energy (> 1600 nm).

The colour range accessible through a collinear OPA is extended through further non-linear processes such as sum and difference frequency generation (SHG, DFG) between the signal (or idler, depending on wavelength of interest) and the pump. Similarly, the second (or higher) harmonic generation (SHG) of the signal (or idler) can be used. These extensions allow OPAs to span from the ultraviolet to the infrared in one system.

Momentum conservation also provides two unique geometries, the collinear geometry wherein seed and pump arrive parallel to the mixing crystal and non-collinear wherein the seed and pump arrive at some angle α. This angular separation provides the following phase matching condition [25]:

$$k_p \cos(\alpha) = k_i \cos(\vartheta) + k_s \tag{1.86}$$

where α is the fixed angle between pump and seed, ϑ is the self-correcting angle between generated signal and idler. This non-collinear pumping leads to a large swath of generated signal. When pumped with the second harmonic of titanium:sapphire, the degeneracy point of mixing is now ~800 nm leading to an amplified ω_s range spanning the visible spectrum, as shown in Figure 1.25.

A schematic describing the home-built double-pass broadband non-collinear optical parametric amplifier (NOPA) can be seen in Figure 1.26. Roughly 400 µj/pulse of fundamental is telescoped down to > 5mm to maximize doubling efficiency in a 1 mm 29.2° cut BBO crystal. The second harmonic used to pump the NOPA is split from the remaining fundamental through a p-coated 400 nm dielectric mirror. The pump beam then traverses a fixed delay line and is split by a 50/50 ultrafast beam splitter with the transmitted portion acting as the pump for the first pass and the reflected portion acting as the pump for the second.

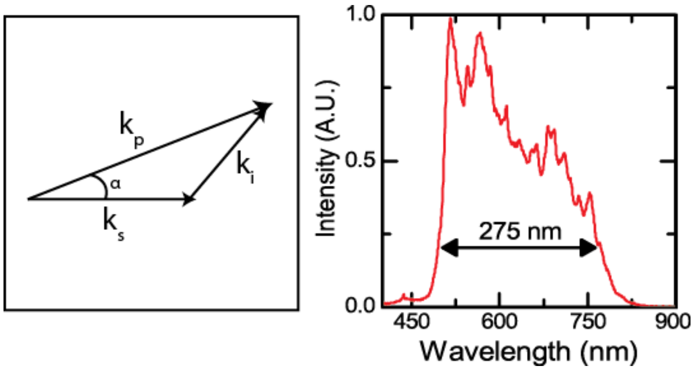

Figure 1.25 - a) Phase-matching condition for non-collinear optical parametric amplification. b) Output of home-built non-collinear optical parametric amplifier

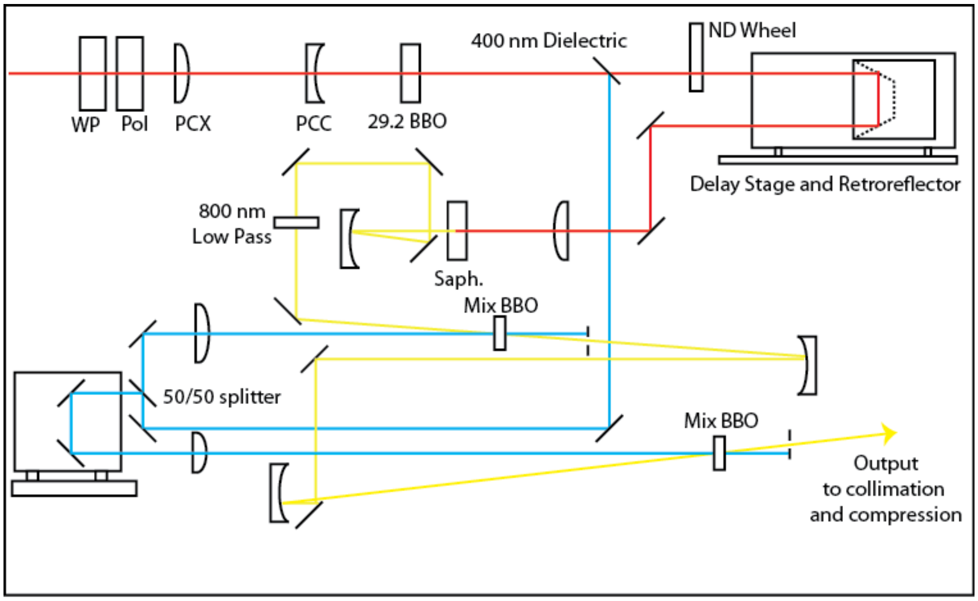

Figure 1.26 – Schematic diagram of home-built non-collinear optical parametric amplifier. Note: beam-paths and optics are not drawn to scale.

Tip:

Overdriving (pumping with too much intensity) either the sapphire to generate seed or the mixing BBOs will lead to large instabilities in the NOPA. You may get more power – but it will not be worth it.

Generally, the minimal seed energy required to get output is best.

In the first pass, the pump is focused and a 1 mm thick 32° cut mixing BBO is placed shortly after the focus to minimize the effects of self-focusing.[25] The intensity of the pump is increased to the point of generating superfluroescence from the BBO. The remaining second harmonic is caught by a beam dump. In the second pass, the pump is sent through a delay stage and subsequently focused slightly before a second 1 mm thick, 32° cut BBO mixing crystal, similarly at intensities nearing superfluroescence.

The remaining fundamental is sent through an optical density wheel to control power and a delay stage to fine tune the optical path length to match that of the first-pass pump line. It is then focused through a 2 mm sapphire plate to generate white-light continuum to act as a seed. The seed (S-polarized) is then focused on the first pass mixing BBO at an angle, α = 3.6°, and overlapped with the pump (P-polarized) in a type-II phase matching scheme. The seed delay and pointing are adjusted to maximize bandwidth and intensity of the amplified signal.

For the second pass the signal is separated through a pinhole and rounded toward the second mixing BBO, using only reflective optics. It is similarly focused and overlapped with the second pass pump at an appropriate angle. The delay of the pump (via the 2nd pass delay stage), pointing of the seed, and crystal angle are iterated to maximize final output signal intensity. The output is then sent through a 400 nm notch filter and collimated. In order to address spatial chirp across the output, as well as clean up the mode, the beam can be focused through a 100 μm pinhole prior to collimation, however this greatly reduces output intensity. Alternatively, the NOPA should be pumped with collimated second harmonic as opposed to focusing; unfortunately this would require greater pump intensities.

Tip:

Always be weary of focal lengths when collimating or focusing.

If the lens isn't AR coated, the back – reflection (which you used to align the lens of course) may end up burning an optic up-table.

The NOPA produces ~8 μj/pulse over ~250 nm of bandwidth FWHM with a maximum compression through a grating-prism pair and an acousto-optic programmable dispersive filter (AOPDF) of ~16 fs. In principle, optical pulses with the broad-bandwidth output by the NOPA should be well below 10 fs in duration; however, compression methods available at the time of development were insufficient. A Spatial-Light Modulator (SLM) can provide the simplified compression required for the broad-bandwidth two-dimensional electronic spectrometer discussed in chapter 5.[26, 27]

1.4.2.2.3 – The Probe: Super continuum Generation

Broadband probe sources are convenient in linear and non-linear spectroscopies alike. There exist many methods for developing broadband probe sources from the UV to the IR from photonic crystal fibers,[28] filament-in-air,[29, 30] gases,[31] to NOPAs.[25, 32] The probe used throughout the dissertation was derived through white-light continuum generation in sapphire plates.[33]

Super continuum generation is a non-linear phenomenon which is believed to occur through a myriad of processes, such as self-focusing, self-phase modulation, and self-steepening.[34, 35] A proper discussion of these non-linear processes may be found in '*Non-linear optics'* by Boyd.[35]

A simplified optical layout for compressed white-light continuum generation is shown in Figure 1.27. As with all optics, normal incidence to the center of the focusing lens is priority in order to obtain a stable, circular single-filament probe. Reflective optics were used throughout the design in order to minimize the group velocity dispersion. Prism pairs are employed in a folded prism compressor design to compensate for existing group-velocity dispersion (GVD) as well as to allow for spatial selection of desired probe bandwidth through a slit.

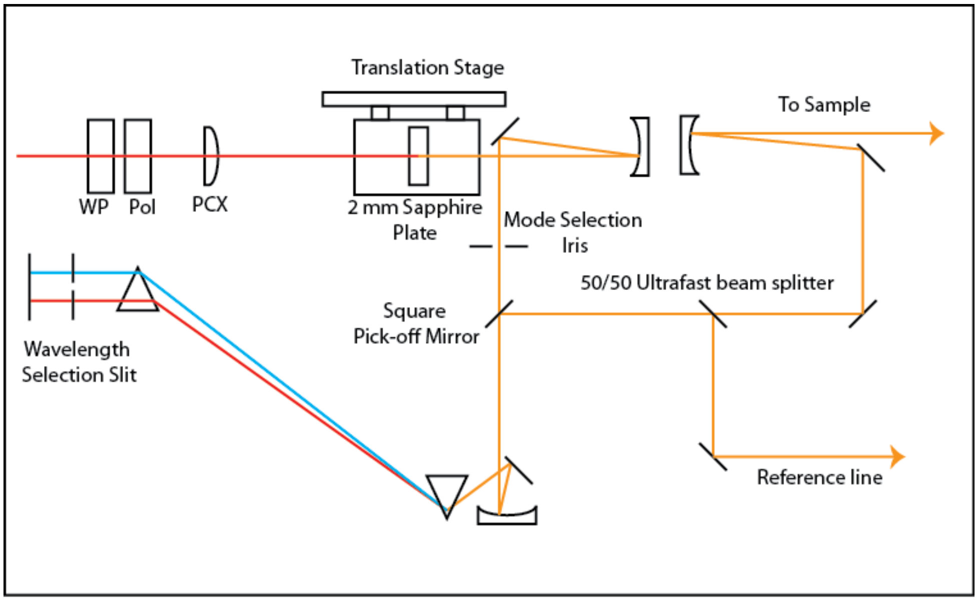

Figure 1.27 – Simplified white-light super continuum generation setup. Folded prism pair included for compression as well as probe-wavelength selection (in the case of Time Domain Transient Absorption).

1.4.2.2.4 – 'Chirp-Free' Probe and Instrument Response Functions

The instrument response function (IRF) for a given pump-probe design, as with most time-resolved spectroscopic techniques, is ultimately determined by the temporal convolution of the pump and probe[1]:

$$IRF(t) = \int_{-\infty}^{\infty} Probe(t)\, Pump(t-\tau)\, dt \qquad (1.87a)$$

$$\Delta OD(t) \sim Population(t) \otimes IRF(t) \qquad (1.87b)$$

Clearly, the desired IRF would be the direct result of Fourier limited pump and probe pulses. Barring the availability of custom designed chirped mirrors, spatial light modulators, or grating-prism pairs, the white light, single-filament continuum probe, generally, has a large GVD and is the limiting component of the IRF.

---

[1] Time Resolved Fluorescence spectroscopy often has the IRF defined as the convolution of the excitation pulse and the decay lifetime. Deconvolution of the IRF is pertinent in both transient absorption as well as fluorescence lifetime measurements.

The GVD, or chirp, of the continuum is determined via cross-correlation in a 30 μm 29.2° cut BBO crystal wherein the SFG between a selected spectral region of the probe and a known duration source acting as pump, such as the fundamental of the chirped-pulse amplifier (CPA) or the output of an OPA, is measured in a photomultiplier tube. The SFG is fiber-coupled to a monochrometer, which aids in the separation of the overlapping SHG signals of the 800 nm pump and residual 800 nm within the probe respectively. The process is repeated for the entire probe spectral region of generating a 'chirp-set'. This chirp-set data is then used to physically correct for the differing arrival times of the probe relative to the pump as dictated by the GVD, or:

$$t_0(\lambda) \stackrel{\text{def}}{=} t_{Probe}(\lambda) - t_{Chirp}(\lambda) = t_{Pump}(\lambda) \tag{1.88}$$

The correction is done by adjusting the optical path length of the pump through the Newport Precision delay-stages to ensure an appropriate t_0 for all wavelengths scanned in a transient absorption spectrum. This leads to a 'Chirp-free' transient absorption spectrum.

This correction could be done in post-processing given that the IRF(λ) is known, however, throughout the dissertation the pre-processing 'chirp-free' method was used.

1.4.2.2.5 – Timing Mechanisms and Data Acquisition

While ultimate temporal resolution in a pump-probe experiment is determined by the IRF, data acquisition is fundamentally limited by both the repetition rate of the laser system and the rise-time and response of the given detectors. For example, while the 1 KHz repetition rate of the CPA used through the dissertation marked the maximal data acquisition rate per shot, the scan rate was determined by the relative communication times between the Data Acquisition Card (DAQ), the PXI (DAQ Controller), the delay stages and the software controlling them. Clearly, managing the relative arrival times of pulses and signalling integrators when to operate and delay stages when to move requires an intricate timing scheme.

In order to maximize experimental efficiency as well as provide a stamp for each relative pulse, or shot, (which is pump on and which is pump off, for example) a stable, consistent master clock signal is required. The laser used throughout the dissertation has two possible clock signals: the 76 MHz oscillator output as measured by a photodiode, and the 1 KHz signal delay generator output. The major timing scheme used can be seen in Figure 1.28. The 76 MHz oscillator photodiode output is split through a 1:4 fan-out line-driver which replicates and amplifies the input signal. Two outputs lead to the RF generators for the AOPDFs used for the two-dimensional electronic spectrometer, described in chapter 5, to act as an external clock and the third output leads to the signal delay generator. The signal delay generator divides the 76 MHz output to 1 KHz to trigger both of the Pockel Cells within the amplifier cavity. The signal delay generator may also output a 1 KHz TTL signal which is used as an external trigger for a Pulse-Delay generator (Berkley Electronics). This PDG is the master timing box for both the two-dimensional electronic spectrometer as well as the pump-probe setup. It provides external trigger timing signals for the PXI, the signal integrator, and the RF generators all based on the master trigger from the signal delay generator.

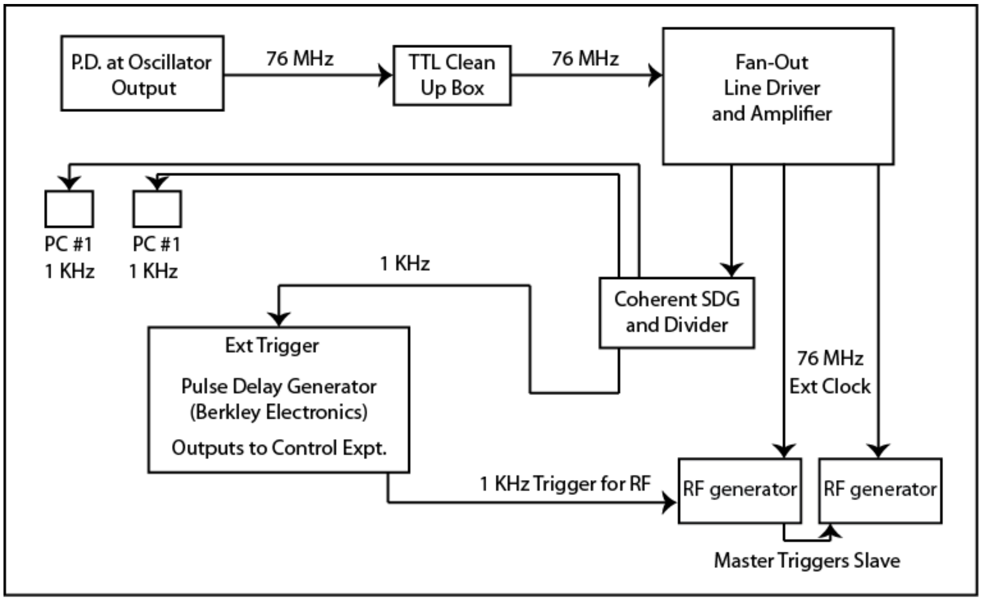

Figure 1.28 – Diagram of major timing scheme components in hybrid two-dimensional electronic and pump-probe spectroscopic instrument.

1.4.2.2.6 – Laser System and Optical Layout

The commercial high intensity femtosecond laser system has become, to belabour a colloquial, 'turnkey'. Traditional CPA systems are now available as one-box devices (pumps, seed and amplifier included) with output energies as high as 5 mJ/pulse at 1 kHz. In point, pump-probe spectroscopic kits are available from Ultrafast Systems. Similarly, the availiablily of optical parametric amplifiers, both co- and non-colinear, greatly simplifies pump sources. The subtleties come in the myriad of options for both detection and the desired geometries for a given signal.

Tip:

Remember that you can move anything. The key in optics is to start straight and flat. Use two irises along the laser table to define a straight and level line, translate your mirror to align the beam through the first iris and twist your mirror to align through the far field iris. Iterate until the beam goes equally through both irises:

You now have a flat and straight beam.

Tip:

Always Check For Clipping!

Remember that your beamwaist measurements assume a Gaussian beam. If you have a hard edge, or an odd focus, your beamwaist will be off.

The laser system used throughout the dissertation was a Legend CPA (2.5 mj/pulse at 1 KHz, λ = 800 nm with 24 nm FHWM) seeded by a MIRA oscilator (~4 nj/pulse at 76 MHz, λ = 800 with ~35 nm FHWM) pumped by an Evolution 30 Nd:YLF (~19 Watt at 1 KHz at 20 Amp, λ = 531 nm) and Verdi V5 (~5 Watt CW, λ = 531 nm) respectively, all supplied through Coherent Inc. The pump beams were derived through one or both OPAs with either SHG or SFG extensions, depending on desired wavelengths, or through directly doubling the fundamental of the CPA in a 0.1 mm BBO crystal. The single filament white light probe was generated through a 2 mm sapphire plate as described above. Post-sample, re-colimated probe was sent through an analyzer and directed towards one of two detection setups:

1) Time Domain Transient Absorption (TDTA) using coupled photodiodes and a roughly 15 nm FHWM portion of the white light probe in signal/reference configuration
2) Transient Absorption Spectra (TAS) using a fiber coupled scanning monochrometer (Jorb Yvion) using the region of the white light probe spanning roughly 500 nm to 700 nm.

Pump delay was achieved through elongaiting the optical path via Newport delay stages.

Generally, optical choppers or shutters may be used, depending on desired acquisition rate, to perform pump-probe measurements. The maximal acquisition rate is a function of both detector response time as well as material hysteresis. For example, assuming a system has an acquisition rate of one kilohertz, if a sample has any dynamic response beyond 1 millisecond the compounded response will be detected from shot to shot. It may be necessary to make use of both optical shutters and choppers to allow for both detector and system response rates.

An example of a simplified chopping scheme is show in Figure 1.29. The design used throughout this dissertation relies on a similar timing mechanism. The shot pattern is managed through direct control of the chopper duty cycle via the PDG.

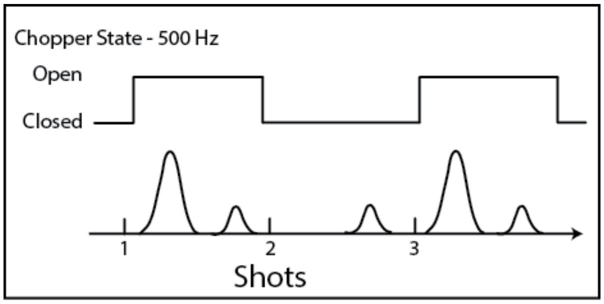

Figure 1.29 – Chopper TTL scheme for single-pump/probe experiment at 500 Hz

1.4.2.2.7 – State-Resolved Ultrafast Optical Spectroscopy

Optical degradation and laser stability are major concerns in ultrafast spectroscopy. Lab temperature, table oscillations, and pointing drift all affect the quality of an acquired signal. Similarly, sample preparation and quality can vary from experiment to experiment and as a function of exposure and lab time. It is beneficial, in all these

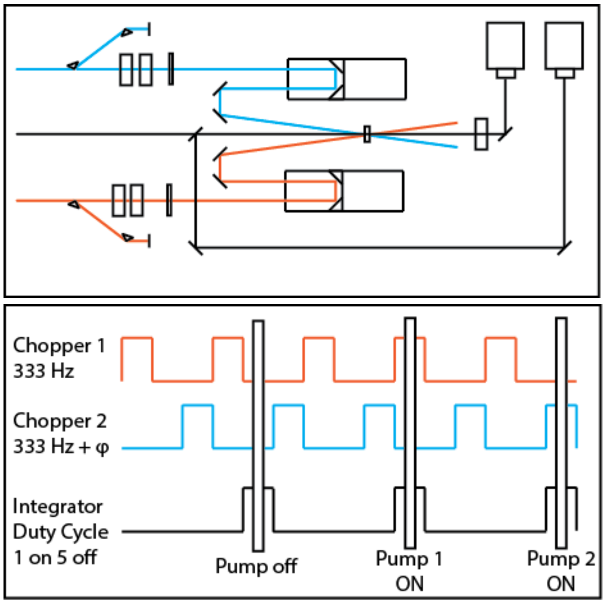

Figure 1.30 – Optical layout for state resolved optical spectroscopy (a). Chopping scheme

cases, to simultaneously investigate competing dynamics of interest. This is possible through a state-resolved multi-pump design.

The multi-pump design simply doubles the requirements of a single pump-probe experiment but greatly increases productivity of the spectroscopic instrument. Beyond this, however, it allows for the direct measurement of relative differential optical density, or ΔΔOD. This particular technique will play a major role in discussions of exciton dynamics in chapter 4.

Tip:

Always Check Chopper Phases in both ΔOD scans as well as on a photodiode. It should go from Noise floor (OFF) to a non-saturating level (ON)

Put a card in the way to block the pump during a test run. If your ΔOD signal doesn't go to 0: you are leaking. Also, in multi-pump experiments, make sure the right trace is going to 0 (red for chopper 1, green for chopper 2)!

The timing for the state-resolved approach is similarly controlled through the PDG as described previously, albeit with a slight increase in complexity. Given the nature of the data acquisition, and the 1 KHz repetition rate of the laser, the maximum acquisition rate is 333 Hz per pump source. The chopping scheme is outlined in Figure 1.30.

1.4.3 – Two-Dimensional Electronic Spectroscopy

Two-dimensional spectroscopy is a powerful non-linear spectroscopic technique which provides information regarding the 3rd order non-linear response of a material.[6, 17] The common analogy is that of multi-dimensional nuclear magnetic resonance imaging (NMR). Wherein 1D proton NMR provides information as to the number and general environment of protons in a given sample, it can be difficult to discern structure for increasingly complex systems. The advent of multi-pulse NMR techniques, such as COSY, allowed for the mapping of the 1D response onto a second frequency axis giving an even greater understanding as to the chemical environment of each proton. Two-dimensional spectroscopy provides the same information: it not only shows absorptive states but also the coupling between states.

Two-dimensional spectroscopy has been used to explore the various charge-transport properties of biological systems,[8, 36-40] protein folding dynamics and structure,[41-45] excitonic environments of semiconductor quantum dots [46, 47] and quantum wells,[48-50] water,[51, 52] and a myriad of other systems. Nearly anything that benefits from linear or pump-probe spectroscopies could benefit from two-dimensional spectroscopy.

While pump-probe, photon-echo, and linear spectroscopies may provide information pertaining to dynamics and relative relaxation rates, and shine some light on the various levels of spectral broadening, they do not necessarily provide information regarding the coherent couplings of states. Two-dimensional electronic spectroscopy provides, through a full mapping of the 3rd order response, just such information.

The development and implementation of a novel two-dimensional electronic spectrometer, and all pertinent experimental details, will be the subject of chapter 5.

1.5 - References

1. Lewis, K.L.M. and J.P. Ogilvie, Probing Photosynthetic Energy and Charge Transfer with Two-Dimensional Electronic Spectroscopy. The Journal of Physical Chemistry Letters, 2012. **3**(4): p. 503-510.

2. Turner, D.B., et al., Quantitative investigations of quantum coherence for a light-harvesting protein at conditions simulating photosynthesis. Phys Chem Chem Phys, 2012. **14**(14): p. 4857-74.

3. Tyagi, P., et al., Two-Color Two-Dimensional Electronic Spectroscopy Using Dual Acousto-Optic Pulse Shapers for Complete Amplitude, Phase, and Polarization Control of Femtosecond Laser Pulses. J Phys Chem A, 2013.

4. Helmut H. Telle, A.G.U., Robert J. Donovan, Laser Chemistry: Spectroscopy, Dynamics and Applications. 2007: Wiley.

5. Fayer, M.D., Elements of Quantum Mechanics. 2001, New York: Oxford Univeristy Press.

6. Zanni, P.H.a.M., Concepts and Methods of 2D Infrared Spectroscopy. 2011: Cambridge University Press.

7. Mukamel, S., Principles of Optical Non-linear Spectroscopy. 1995: Oxford University Press.

8. Schlau-Cohen, G.S., A. Ishizaki, and G.R. Fleming, Two-dimensional electronic spectroscopy and photosynthesis: Fundamentals and applications to photosynthetic light-harvesting. Chemical Physics, 2011. **386**(1–3): p. 1-22.

9. Cheng, Y.C. and G.R. Fleming, Dynamics of light harvesting in photosynthesis. Annu Rev Phys Chem, 2009. **60**: p. 241-62.

10. Feynman, R.P., Quantum Electrodynamics. Advanced Book Classics, ed. W. Press. 1961: Perseus Books Group.

11. Myers, J.A., et al., Two-Dimensional Electronic Spectroscopy of the D1-D2-cyt b559 Photosystem II Reaction Center Complex. The Journal of Physical Chemistry Letters, 2010. **1**(19): p. 2774-2780.

12. Vouilloz, F., et al., Polarization anisotropy and valence band mixing in semiconductor quantum wires. Physical Review Letters, 1997. **78**(8): p. 1580-1583.

13. Jonas, D.M., et al., Pump−Probe Polarization Anisotropy Study of Femtosecond Energy Transfer within the Photosynthetic Reaction Center of Rhodobacter sphaeroides R26. The Journal of Physical Chemistry, 1996. **100**(30): p. 12660-12673.

14. Anderson, K.E.H., et al., Noise analysis and noise reduction methods in kilohertz pump-probe experiments. Review of Scientific Instruments, 2007. **78**(7): p. 073101-6.

15. Tokmakoff, A. Time-dependent quantum mechanics and spectroscopy. MIT Open Courseware 2013 [cited 2013; Available from: http://ocw.mit.edu

16. Cho, M.H., et al., The integrated photon echo and solvation dynamics. Journal of Physical Chemistry, 1996. **100**(29): p. 11944-11953.

17. Jonas, D.M., Two-dimensional femtosecond spectroscopy. Annual Review of Physical Chemistry, 2003. **54**(1): p. 425-463.

18. Zhong, H., et al., Electronic States and Exciton Fine Structure in Colloidal CdTe Nanocrystals. The Journal of Physical Chemistry C, 2009. **113**(24): p. 10465-10470.

19. Smith, A.V., SNLO nonlinear optics code, 2005, AS Photonics: Albuquerque, NM.

20. Barbara, P.F., T.J. Meyer, and M.A. Ratner, Contemporary issues in electron transfer research. The Journal of Physical Chemistry, 1996. **100**(31): p. 13148-13168.

21. Mooney, J., et al., Challenge to the deep-trap model of the surface in semiconductor nanocrystals. Physical Review B, 2013. **87**(8): p. 081201.

22. Abella, I.D., N.A. Kurnit, and S.R. Hartmann, PHOTON ECHOES. Physical Review, 1966. **141**(1): p. 391-&.

23. Klimov, V.I., Optical Nonlinearities and Ultrafast Carrier Dynamics in Semiconductor Nanocrystals. The Journal of Physical Chemistry B, 2000. **104**(26): p. 6112-6123.

24. Chatelain, R.P., et al., Ultrafast electron diffraction with radio-frequency compressed electron pulses. Applied Physics Letters, 2012. **101**(8): p. 081901-081901-4.

25. Manzoni, C., D. Polli, and G. Cerullo, Two-color pump-probe system broadly tunable over the visible and the near infrared with sub-30 fs temporal resolution. Review of Scientific Instruments, 2006. **77**(2): p. 023103-9.

26. Baum, P., et al., Real-time characterization and optimal phase control of tunable visible pulses with a flexible compressor. Applied Physics B, 2002. **74**(1): p. s219-s224.

27. Stone, K., et al., Spatiotemporal femtosecond pulse shaping using a MEMS-based micromirror SLM, in Ultrafast Phenomena XV, P. Corkum, et al., Editors. 2007, Springer Berlin Heidelberg. p. 184-186.

28. Dudley, J.M., G. Genty, and S. Coen, Supercontinuum generation in photonic crystal fiber. Reviews of Modern Physics, 2006. **78**(4): p. 1135-1184.

29. Akozbek, N., et al., White-light continuum generation and filamentation during the propagation of ultra-short laser pulses in air. Optics Communications, 2001. **191**(3-6): p. 353-362.

30. Petersen, P.B. and A. Tokmakoff, Source for ultrafast continuum infrared and terahertz radiation. Opt. Lett., 2010. **35**(12): p. 1962-1964.

31. Corkum, P.B., C. Rolland, and T. Srinivasan-Rao, Supercontinuum Generation in Gases. Physical Review Letters, 1986. **57**(18): p. 2268-2271.

32. Myers, J.A., et al., Two-color two-dimensional Fourier transform electronic spectroscopy with a pulse-shaper. Opt. Express, 2008. **16**(22): p. 17420-17428.

33. Brodeur, A. and S.L. Chin, Ultrafast white-light continuum generation and self-focusing in transparent condensed media. Journal of the Optical Society of America B-Optical Physics, 1999. **16**(4): p. 637-650.

34. Fork, R.L., et al., Femtosecond white-light continuum pulses. Opt. Lett., 1983. **8**(1): p. 1-3.

35. Boyd, R.W., Nonlinear optics. 2nd ed.: Acad. Press, 2003.

36. Brixner, T., et al., Two-dimensional spectroscopy of electronic couplings in photosynthesis. Nature, 2005. **434**(7033): p. 625-628.

37. Wilson, H.D., et al., Two Dimensional Broadband Electronic Spectroscopy of Photosystem II Core Complexes. Biophysical Journal, 2013. **104**(2): p. 653A-653A.

38. Lewis, K.L.M. and J.P. Ogilvie, Probing Photosynthetic Energy and Charge Transfer with Two-Dimensional Electronic Spectroscopy. Journal of Physical Chemistry Letters, 2012. **3**(4): p. 503-510.

39. Myers, J.A., et al., Two-Dimensional Electronic Spectroscopy of the D1-D2-cyt b559 Photosystem II Reaction Center Complex. Journal of Physical Chemistry Letters, 2010. **1**(19): p. 2774-2780.

40. Abramavicius, D. and S. Mukamel, Exciton Delocalization and Transport in Photosystem I of Cyanobacteria Synechococcus elongates: Simulation Study of Coherent Two-Dimensional Optical Signals. Journal of Physical Chemistry B, 2009. **113**(17): p. 6097-6108.

41. Hamm, P., et al., The two-dimensional IR nonlinear spectroscopy of a cyclic penta-peptide in relation to its three-dimensional structure. Proceedings of the National Academy of Sciences of the United States of America, 1999. **96**(5): p. 2036-2041.

42. Hamm, P., M.H. Lim, and R.M. Hochstrasser, Structure of the amide I band of peptides measured by femtosecond nonlinear-infrared spectroscopy. Journal of Physical Chemistry B, 1998. **102**(31): p. 6123-6138.

43. Ganim, Z., et al., Amide I two-dimensional infrared Spectroscopy of proteins. Accounts of Chemical Research, 2008. **41**(3): p. 432-441.

44. Demirdoven, N., et al., Two-dimensional infrared spectroscopy of antiparallel beta-sheet secondary structure. Journal of the American Chemical Society, 2004. **126**(25): p. 7981-7990.

45. Woutersen, S., et al., Subpicosecond conformational dynamics of small peptides probed by two-dimensional vibrational spectroscopy. Proceedings of the National Academy of Sciences of the United States of America, 2001. **98**(20): p. 11254-11258.

46. Moody, G., et al., Influence of confinement on biexciton binding in semiconductor quantum dot ensembles measured with two-dimensional spectroscopy. Physical Review B, 2013. **87**(4).

47. Turner, D.B., Y. Hassan, and G.D. Scholes, Exciton Superposition States in CdSe Nanocrystals Measured Using Broadband Two-Dimensional Electronic Spectroscopy. Nano Letters, 2012. **12**(2): p. 880-886.

48. Kuehn, W., et al., Strong Correlation of Electronic and Lattice Excitations in GaAs/AlGaAs Semiconductor Quantum Wells Revealed by Two-Dimensional Terahertz Spectroscopy. Physical Review Letters, 2011. **107**(6).

49. Davis, J.A., et al., Three-dimensional electronic spectroscopy of excitons in asymmetric double quantum wells. Journal of Chemical Physics, 2011. **135**(4).

50. Stone, K.W., et al., Two-Quantum 2D FT Electronic Spectroscopy of Biexcitons in GaAs Quantum Wells. Science, 2009. **324**(5931): p. 1169-1173.

51. Kolano, C., et al., Watching hydrogen-bond dynamics in a beta-turn by transient two-dimensional infrared spectroscopy. Nature, 2006. **444**(7118): p. 469-472.

52. Hamm, P. and J. Savolainen, Two-dimensional-Raman-terahertz spectroscopy of water: Theory. Journal of Chemical Physics, 2012. **136**(9).

2 Nanocrystals

2.1 – Introduction

An elegantly symbiotic relationship exists between the spectroscopist and the semiconductor nanocrystal (NC): an understanding of the inherent excitonic environment of a given crystal is paramount to developing practical devices and, due to the NCs uniquely size-dependent optical properties, said understanding is readily available through the combination of optical spectroscopies.

The NC field can be partitioned into two worlds: that of the epitaxial quantum dot and quantum well, and that of the colloidal NC, first explored by Brus.[1] It is the second embodiment which will be primary focus of this dissertation.

The colloidal quantum dot exists in a realm between the bulk and the atom and, as such, provides a platform from which one can study a plethora of physical phenomena (Figure 2.1). This is of significant interest to the study of the effect of quantum confinement on processes which occur in bulk material. These processes, such as relaxation dynamics, optical gain, carrier multiplication and multi-exciton generation, will be discussed.

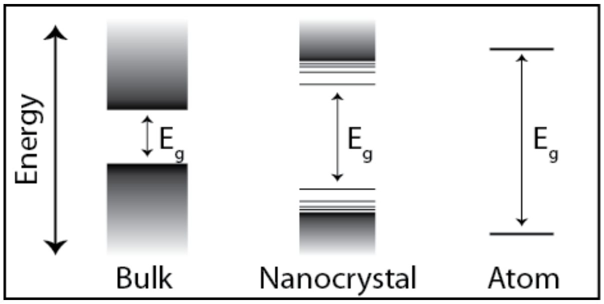

Figure 2.1 - Pictorial representation of band gaps as a function of size.

The goal of this chapter is to guide the reader towards a basic understanding of the size-dependent optical properties of NCs. Through discussion of the varying levels of theoretical treatment, developing a general understanding of the excitonic environment, and introducing a basic nomenclature, the chapter will assist in the interpretation of results presented throughout the thesis.

2.2 – Theory

The theoretical treatment of semiconductor NCs is evolving. At its simplest, there exist two levels of theory: the top-down analytical approach through inclusion of the tight binding, effective mass, and envelop approximations to the Bloch theorem,[2, 3] and the bottom-up atomistic ab initio methods.[4, 5] Each method introduces its own degree of complexity as well as its own descriptive advantages. The former methods drove the spectroscopic description of NCs from their inception, the latter came with increased experimental interest and the evident intricacy of the optical properties. It should be noted that the proceeding theory does not directly account for the surface of the NC which will be discussed, both experimentally and theoretically, in its own introductory section as well as throughout the dissertation.

2.2.1 – A Brief Aside on Band Theory and Nanocrystals

What exactly does it mean to exist between the world of the bulk and the atom? A NC cannot simply be described as a small chunk of bulk, nor is it a collection of independent atoms in a molecule. A NC has its own unique physical properties distinct from those of the bulk and those of the individual atoms. A molecule involves the overlap of atoms individual atomic orbitals to form molecular orbitals, as shown in Figure 2.2. These orbitals form distinct states as described by molecular orbital theory. Bringing together multiple molecules involves the overlap of multiple molecular orbitals. Electrons within these orbitals obey the Pauli Exclusion Principle which slightly broadens the transitions. When N atoms are brought together the transitions broaden into continuous bands as is typical of solids.[6]

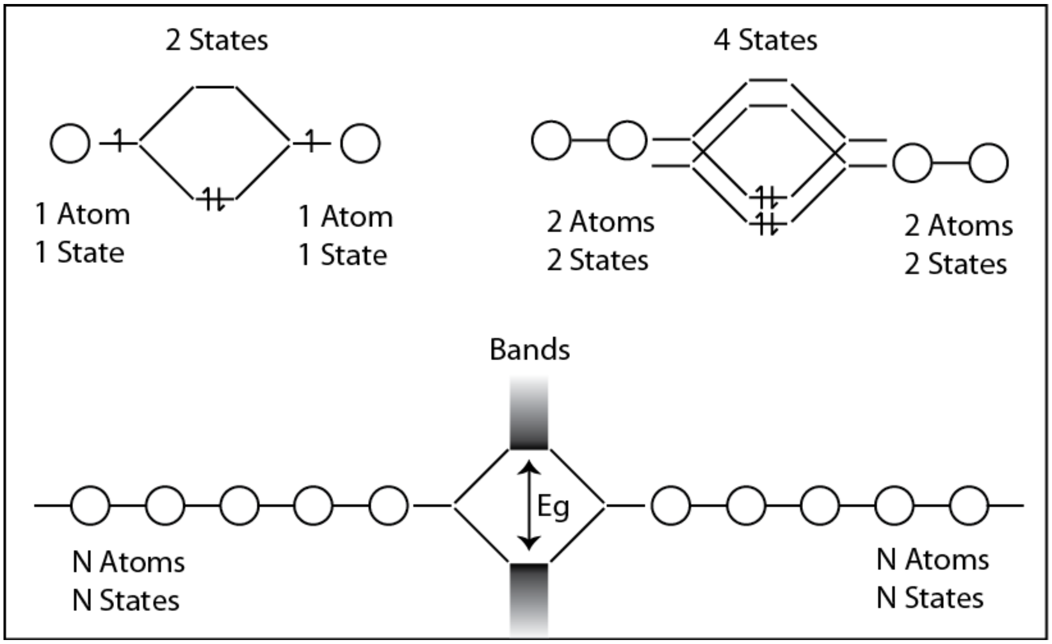

Figure 2.2 – From molecules to bands

Evidently, additional bonding between a few atoms to form larger molecules can have massive consequences on the physical and electronic properties of the system. Conversely, a few additional atoms in a bulk material has little to no effect (assuming they are the same atom which comprises the bulk of the crystal, doping through addition of differing atoms in a crystal is a powerful technique to engineer band structures[7, 8] and will be discussed later): a 1 meter block of steel is, with regards to band structure, much the same as a 500 millimeter block of steel, despite a large reduction in the number of atoms. A NC consists of hundreds to thousands of atoms in a crystal lattice much like a bulk semiconductor, but demonstrates a distinct size-dependence to its optical properties; ie: a few additional monolayers has measureable influence to the emittive and absorptive properties of the material.[9, 10] This is counter to the general description of the bulk.[11]

2.2.2 - Quantum Confinement – From the Bulk to the Atom

Without any theoretical insight, one particular phenomenon is abundantly apparent: when the radius of an NC is shrunk beyond a given limit, its optical spectra radically change.[9, 12] What is causing the shift in the observed band gap and why do seemingly discreet transitions appear in the spectrum? Why do the spectra appear to shift with temperature and composition?[13-16] Why is the addition of as much as a single monolayer affecting the electronic and optical properties of a seemingly bulk crystal lattice?[17]

2.2.2.1 – Simple Band Structures - Sommerfeld Free Electron Gas

A band diagram is a representation of the crystal momentum of a carrier in a lattice[6, 11]. In order to relate the kinetic energy of a carrier in a crystal to its wave vector, k, consider a simple case: a free electron gas confined within a 3-dimensional cube of length L, as shown in Figure 2.3. In the case of a free-particle, the classical kinetic energy is related to the momentum by:

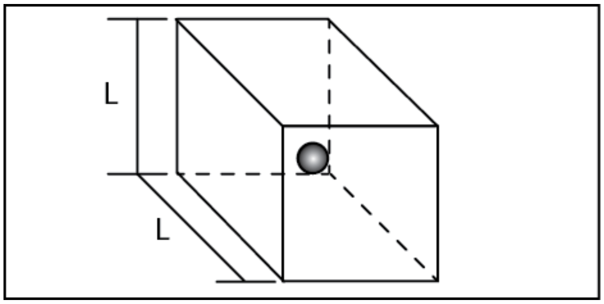

Figure 2.3 – Pictorial representation: a particle in a box

$$\boldsymbol{E = \frac{p^2}{2m^*}} \qquad (2.1)$$

taking the wavevector, k, as related to the momentum of a carrier by:

$$\boldsymbol{p} = \hbar\boldsymbol{k} \tag{2.2}$$

and its relation to the velocity of a carrier as:

$$\boldsymbol{v} = \frac{\boldsymbol{p}}{\boldsymbol{m}} = \frac{\hbar\boldsymbol{k}}{\boldsymbol{m}} \tag{2.3}$$

taking m as the reduced, non-vacuum mass of the electron, or, m* we can relate the classical kinetic energy (1) to the wavevector for a free electron gas as:

$$\boldsymbol{E} = \frac{(\hbar\boldsymbol{k})^{2}}{2\boldsymbol{m}^{*}} \tag{2.4}$$

where k is the wavevector defined as:

$$\boldsymbol{k} = \frac{2\boldsymbol{\pi}}{\boldsymbol{\lambda}} \tag{2.5}$$

and is bound by the potential such that k is of the form:

$$\boldsymbol{k} = \frac{2\boldsymbol{\pi}}{\boldsymbol{L}}\left(\boldsymbol{n}_{x} + \boldsymbol{n}_{y} + \boldsymbol{n}_{z}\right) \tag{2.6}$$

leading to the allowed energies in three dimensions of:

$$\boldsymbol{E} = \frac{\boldsymbol{h}^{2}}{2\boldsymbol{m}^{*}\boldsymbol{L}^{2}}\left(\boldsymbol{n}_{x}^{2} + \boldsymbol{n}_{y}^{2} + \boldsymbol{n}_{z}^{2}\right) \tag{2.7}$$

Note that the reduced Planck's constant has become the standard Planck's constant from the expansion of the wavevector. Immediately, in the case of the Sommerfeld electron gas, three observations are apparent:

1) In the case of bulk crystal of L = 1 cm, The intra-band energy spacing, ΔE(k), is so small, on the order of 10^{-10} eV, as to mimic a continuum of states.
2) The energy depends on the square of k, leading to parabolic bands.
3) ΔE(k) is inversely proportionate to the square of the length of the crystal, L.

The free electron model is limited in its application towards bulk phenomena and is restricted in its scope as it ignores the interaction of electrons with one another, it ignores the configuration of electrons at the moment of collision thereby ignoring configurations involvement in relaxation, and it ignores the role of the metallic ions in the lattice.[11]

This provides a qualitative example for size-dependence in semiconductor NCs, although, as mentioned, it is strictly limited in its physical interpretation of semiconductors. Simply, it demonstrates that limiting the number of lattice sites affects the band structure. These descriptive limitations will be overcome later with the discussion Bloch theorem and application of the effective mass approximation for excitons, the tight binding approximation, and the particle in a sphere boundary condition through the envelope approximation.

2.2.2.2 – Bloch Theorem

In order to move from the fully free electron gas and begin to incorporate the effect on the momentum of a free electron by a periodic lattice we introduce the Bloch theorem: a description of the single-electron in a periodic potential. Specifically, a Bloch function is a solution to the Schrodinger equation for the single electron Hamiltonian [3, 11]

$$H = -\frac{\hbar^2}{2m}\nabla^2 + U(r) \qquad (2.8a)$$

$$U(r+R) = U(r) \qquad (2.8b)$$

where the potential, U(r) is the potential caused by the ions in the crystal lattice and is periodic across the Bravais lattice. Note that at the limit that U(r) vanishes, the Bloch electrons become free electrons and return to the free electron gas description in the previous section.

The Bloch functions themselves are of the form:

$$\psi_{nk}(r) = u_{nk}(r)\, e^{ik\cdot r} \qquad (2.9)$$

where $e^{ik\cdot r}$ represents a plane wave and $u_{nk}(r)$ incorporates the periodic potential of steady-state ions the lattice. A contextually appropriate approximation to extend the Bloch electron treatment is the tight binding approximation. Specifically, the tight binding approximation replaces the perfect site periodicity of u_{nk} in 2.9 with a more general summation over localized atomic wave functions, or a linear combination of atomic orbitals, such that:

$$\psi_{nk}(r) = \textstyle\sum_R \varphi(r-R)\, e^{ik\cdot R} \qquad (2.10)$$

where $\varphi(r-R)$ can be expanded over a small number of atomic orbitals[11].

$$\varphi(r-R) = \textstyle\sum_n b_n \psi_n(r) \qquad (2.11)$$

This approximation will have practical implications when implementing a spherical boundary condition describing a confined carrier as in the case of semiconductor NC.

2.2.2.3 – Free Excitons and the Effective Mass

In the event a bulk semiconductor absorbs a photon, an electron is excited from the valence band to the conduction band. In its wake is left an absence of negative charge, or, a hole as shown in Figure 2.4. This electron-hole pair, called an exciton, experiences a Coulomb attraction whose ionization energy is described by [6, 18, 19]

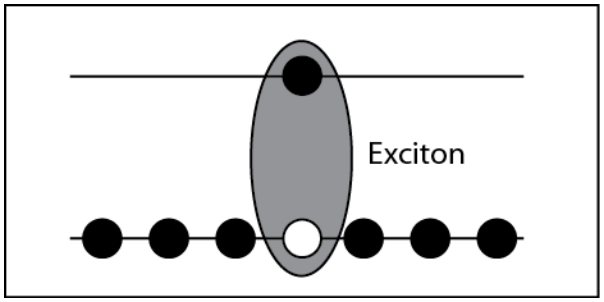

Figure 2.4 - Pictorial representation of an Exciton

$$E_x = \frac{-m_r^* q^4}{2h^2\epsilon^2}\frac{1}{n^2} \tag{2.12}$$

where n is an integer labelling the excitonic states and n ≥ 1 and m_r^* is the reduced mass, or:

$$\frac{1}{m_r^*} = \frac{1}{m_e^*} + \frac{1}{m_h^*} \tag{2.13}$$

This exciton is freely mobile about the crystal under the condition that the electron and hole must move together, ie: their translational velocities must meet the following condition in momentum space [6]:

$$\left[\frac{dE}{dk}\right]_{Electron} = \left[\frac{dE}{dk}\right]_{Hole} \tag{2.14}$$

This approximation accounts for the fact that the center of gravity for the exciton is not located purely on the nucleus. This effective mass approximation, whose influence on NC theory will be described in detail later, lends the following kinetic energy for an exciton in a bulk semiconductor [6, 18, 19]:

$$E_k = \frac{h^2 K^2}{2(m_e^* + m_h^*)} \quad (2.15)$$

where K is a momentum vector describing the exciton restricted such that K = k_e + k_h .[18, 19] The quadratic dependence of K gives shape to the k-space band for a model 2-band direct gap semiconductor. Similar to the discussion of the free electron model, the relative energy spacing is very small in the case of a large crystal, however, this solution arises from a Bloch theorem treatment.[18]

2.2.2.4 – Confined Excitons

What happens when the physical length-scale of the crystal is brought to the nanometer scale and one must further restrict the energy of the exciton? To approach this problem, one must develop a yardstick with which to measure confinement. To this end, three size regimes of interest will be defined: consider the Bohr radius of a particle [2, 3]:

$$a_B = \varepsilon \frac{m}{m^*} a_0 \quad (2.16)$$

where a_0 is the standard Bohr radius of the hydrogen atom and ε the dielectric constant of the semiconductor. This particle may either be the electron, the hole, or the bound exciton. The first region, that of the bulk, unconfined particle, is when the crystal radius, a, is much greater than that of the Bohr radius of any of the three particles.[2] In this situation, the particles are unaffected by their surrounding potential and are free to form bands such as those described by equation 2.4. As the lattice shrinks towards the length of the Bohr radius of the hole, the electron, or the exciton respectively, any or all of the particles may become confined: they begin to be limited by their potential boundary. In the case of CdSe, whose excitonic Bohr radius is on the order of 6 nm [2] , there exist two confinement regimes [3]: the intermediate confinement regime where the electron is confined, and the strong confinement regime where all particles are confined, ie: L << a_B.

2.2.2.5 - Particle in a Sphere Model and its Application to NCs

In order to approach the observed transition between bulk and NC, in terms of the bands of a particle in the strong confinement regime as described in the previous section, an appropriate boundary condition is required. One prospective boundary condition is that of the infinite spherical potential as described by the particle in a sphere model, shown in Figure 2.5. The excitons are confined within the quantum dot – which is addressed through the

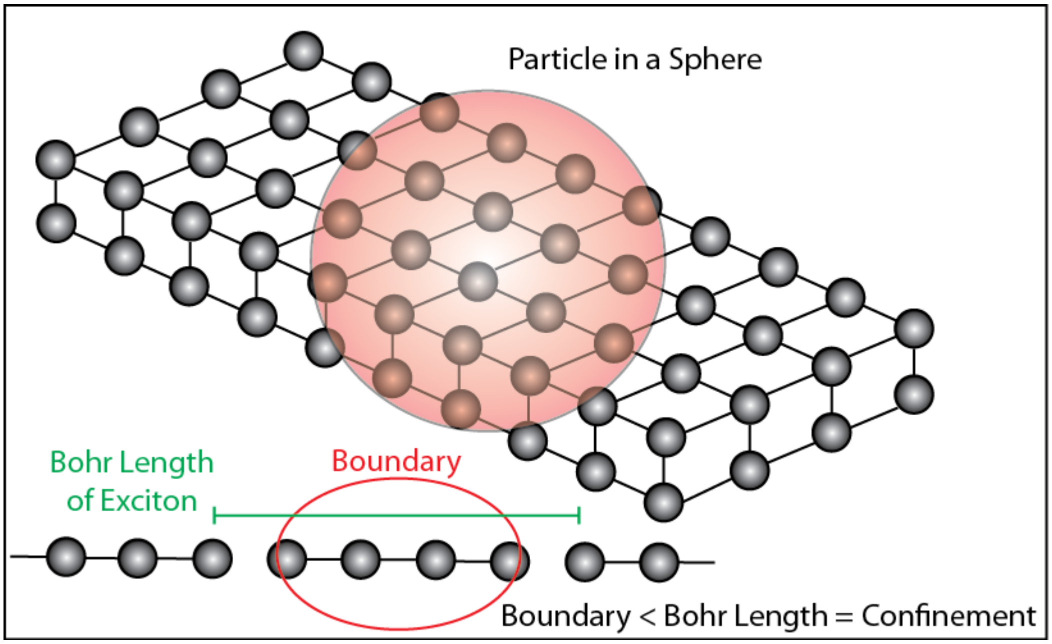

Figure 2.5 – Periodic crystal lattice as bounded by a spherical potential

spherical boundary condition; however the quantum dot is still made up of many periodically aligned atoms within the crystal lattice whose influence on band structure can be addressed through Bloch functions and the tight binding approximation. In this case the single particle wavefunction is expressed as a linear combination of Bloch functions [3]:

$$\psi_{sp}(r) = \sum_k C_{nk} u_{nk}(r) e^{ik \cdot r} \tag{2.17}$$

and the solutions are given by the solutions to the particle in a sphere whose energies are in turn given by [2, 3]:

$$E_{l,n}^{e,h} = \frac{h^2 \varphi_{l,n}^2}{2 m_{e,h} a^2} \tag{2.18}$$

Where $m_{e,h}$ are the mass of the electron and the hole respectively, and $\varphi_{l,n}$ is the n^th^ root of the l^th^ spherical Bessel function. It is these spherical harmonics which give the degeneracies and nomenclature for the optical transitions within the analytical approach.

While this approach provides a qualitative description of the optical properties as well as provides a nomenclature for the optical transitions which will be described shortly, it requires the treatment of the electron and the hole as individual free particles. As discussed in the previous section, the Columbic interaction between a bound electron-hole pair is of measurable influence to the allowable energies of a semiconductor. In fact, the Columbic interaction should itself be size dependent, scaling with 1/a. In the strong confinement regime, the regime of general interest to this dissertation, it is argued that the $1/a^2$ free particle term dominates over the 1/a Columbic term.[3] This holds true when one only considers the size dependence intraband energies, i.e., the relative energy spacing scaled to that of the band-edge transition. However, in order to reconcile the observed size-dependence of the bandgap of CdSe with theory, the Columbic energy must be included as a perturbative addition to the bandgap calculations[2, 3].

2.2.2.6 – Additional terms

While the approximations applied above provide a broad brushstroke, the fine elements must be included in order to style a more complete picture. In the case of CdSe, further expansion of the theory must be applied to understand the fine-structure within the valence band.[3] Primarily, strong spin-orbit coupling splits the degeneracy of the valence band into the heavy-hole, light-hole, and split-off sub-bands.[2] The above calculations also assume a perfectly, monoatomic lattice with inversion symmetry.[2, 3] However, CdSe has wurtsite crystal structure with alternating Cd and Se atoms. This removes the inversion symmetry of the crystal and presents a unique c-axis which further splits the heavy-hole and light-hole near k = 0 through crystal field splitting.[3, 9] Furthermore, in the strong confinement regime, the electron-hole exchange interaction begins to dominate the fine structure. This splitting leads to many closely packed valence band transitions which play a prominent role in Auger recombination discussed later.[20]

Finally, in order to approach a more realistic band structure, further excursion into solid state theory is required. While the spherical boundary conditions provide an elementary description and nomenclature for the observed optical transitions, a more complete picture can be drawn from the invocation of the K · P analytical approach, as well as inclusions of Kane and Luttinger models[3], a discussion of which is beyond the scope of this dissertation.

2.2.3 – ab Initio – Starting from the Atom

Due to the complex nature of the problem, the analytical approach describing the excitonic environment of the semiconductor NC, as discussed above, is inherently filled with approximation in the effort to chip away at the bulk. The approximations lend themselves to interpretations of the transitions which, as will be discussed below, can be in disagreement with experiment.[21] The alternative approach is to start from the ground up: ab initio studies.[21, 22]

While the analytical approach began from the derivation of boundary conditions through approximation, the ab initio studies begin from the atom and builds, through clusters, towards the NC. These calculations are inherently computationally expensive and have been limited in scope until recently. The specific theoretical treatments are well beyond the scope of this dissertation; however, a few key features must be addressed to further discussion of the optical properties. Primarily, the assignment of S-Type character to the 4th transition in the absorption spectrum of CdSe within the effective mass approximation (EMA) approach is in disagreement with pump-probe signatures observed.[21]

While the inclusion of Luttinger and 6-band models allow for excitonic fine-structure and allude to the global Stokes shift between band edge absorption and emission, as well as the narrowing of lineshape with temperature for the core emission state, the Ab initio and psudopotential studies hint at a complex density of states within the NC, especially at high energy. Both theoretical methods, however, agree on a distinct band-edge transition.[23]

2.2.4 – Optical Transitions

The goal of this section is to describe the varied selection rules and degeneracies derived through the given theoretical treatment of the optical properties. Ultimately, an excitonic picture will be presented to provide a universal nomenclature which will be used throughout the dissertation.

A typical linear absorption spectrum with labelled transitions is shown in Figure 2.6. They key features are the relative degeneracies (dictated by the electronic state) and the origin of the hole state.

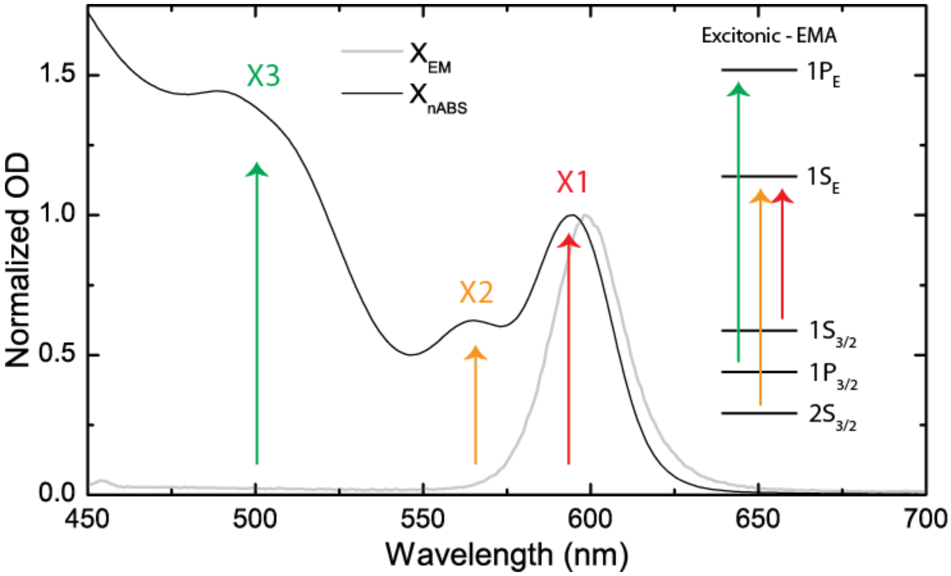

Figure 2.6 – Typical linear absorption spectrum of CdSe in toluene. Coloured lines represent excitonic/EMA treatment for the various transitions.

Through proper optical prescription of the initial excitonic state, state resolved pump-probe studies can provide direct information regarding the relative state filling and Auger recombination rates, as well as indirectly separate hole and electron relaxation.[20, 24, 25]

Immediately apparent from the spectra above is the global Stokes shift between the absorptive and emittive states. This Stokes shift arises from the confinement induced exchange interaction between the electron and the hole of the band-edge exciton as highlighted in Figure 2.7. The EMA assigned 8-fold degenerate $1S_E$-$1S_{3/2}$ band-edge transition is split into two energetically distinct states through the combined angular momentum of the electron and the hole. These states are labelled upper (U) and lower (L) and correspond to total angular momentum of 1 and 2 respectively. These upper and lower states are further split by the crystal asymmetry as described in the theory section. Since the lowest excited fine structure state, the 'dark-exciton', holds two quanta of total angular momentum and therefore cannot directly relax to ground state through emission of a single photon, it must dissipate excess energy through coupling to a phonon.[26-29] This accounts for the long photoluminescent lifetime of the X_{EM} state.[27] The temperature dependence of the core-emission linewidth has similarly been attributed to changes in the thermal distribution of the fine structure.[27-29]

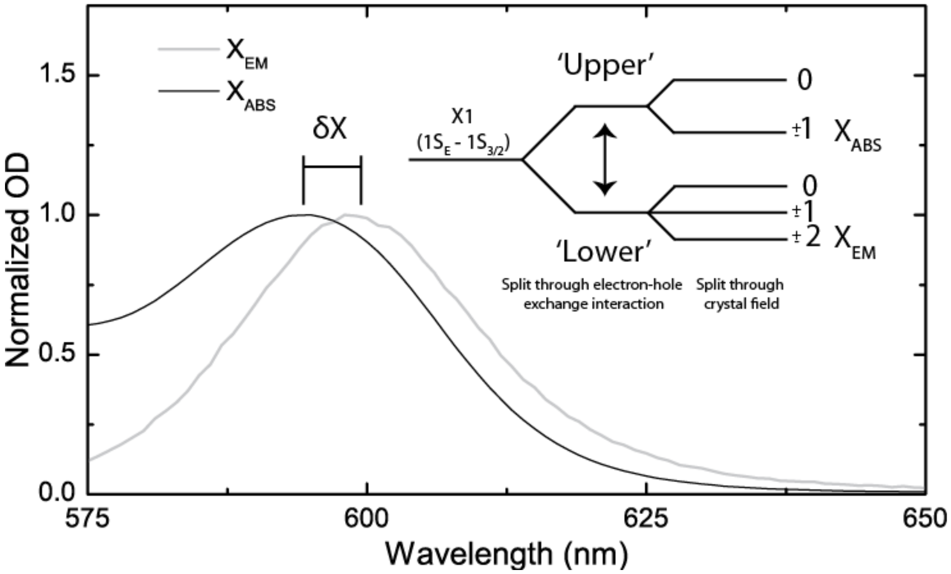

Figure 2.7 – Pictorial representation of the fine-structure splitting of the band-edge exciton

The theoretical assignments of the optical transitions within NC literature have yet to converge.[25] In order to limit obfuscating discussion, the electron and hole may be considered as a single particle: the exciton. In this case, a simplified nomenclature may be introduced: the discreet transitions are considered individual excitonic states and are numbered accordingly. The simplification comes clear when one begins to consider the fine structure for both single and multi-excitonic states.[30]

Beyond the ambiguity in driving forces for observed phenomena, the primary difference between the analytical and ab inito approaches, at least in terms of this dissertation, are the differences in associated electronic states for each given transition. The degeneracies for a given transition are paramount when considering multiple exciting generation (MEG), multi carrier recombination (MCR) or optical gain as they directly dictate the observable relaxation dynamics. For example, in the case of MEG, often the ratio between early and late time band edge bleach dynamics is taken as a measure of the quantum efficiency of the MEG process in a given sample. The principle being that one can analyze the given late and early time ratio to determine how many excitons are created per sample with a low fluence, high energy pump.[31, 32] Given that the theoretically assigned electronic degeneracy of the band edge of CdSe is two, one would ascribe a theoretical maximum 200% yield for a 2:1 ratio. Similarly, in the case of optical gain threshold determination, the relation between the observed differential bleach and average excitation per particle, or <N>, is dependent on direct knowledge of degeneracies.[33]

2.3 - Configurations and Types

With colloidal chemistry the potential for varied chemical morphologies is very real. In the case of semiconductor NCs, there exists a myriad of shapes and sizes, and alloyed compositions, possible: tetrapods,[34-36] heterostructures,[37-39] gradient alloyed systems,[40-48] and even binary superlattices [49] all with their own unique advantages and properties and all realised through controlled colloidal chemistry.

2.3.1 – CdSe: The Quintessential QD

Cadmium Selenide is an II-VI prolate wurtsite NC and, to date, is among the most heavily studied.[50] It was the first NC for which successful, repeatable synthesis was realised.[9] In fact, CdSe synthesis has matured to the commercial level and is readily available through, most notably, Sigma Aldrich, NN-Labs, and Invitrogen. CdSe, or a derivative of, has become a staple in biological imaging,[51-55] optoelectronics,[56-61] photovoltaics,[52, 59, 62-65] and commercial displays.

2.3.2 – Type I vs. Type II Heterostructures

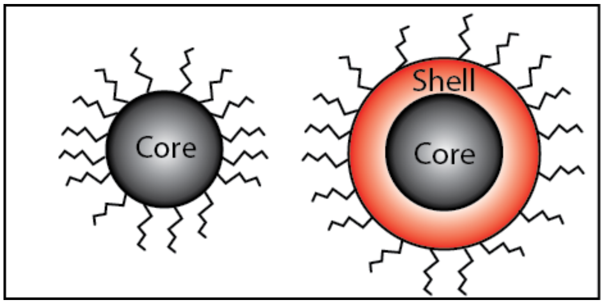

Figure 2.8 – Ligand and ligand/core over-coated nanocrystals

Direct control over the boundary conditions in an effort to affect the band structure itself is the realm of wavefunction engineering in NC. Ligand based systems provide simple barrier control mechanism through electron/hole donor and acceptor choices [66-71]; however, chemical over-coating with an inorganic shell provides another degree of freedom when designing nanostructures (Figure 2.8). The general classification for over-coated nanostructures is identical to that of bulk heterostructures: type I (straddling gap) and type II (staggered gap). Unlike the bulk, however, the ability to tune the gap-width with crystal size provides interesting possibilities. The typical band structures for generic type I and type II NCs are show in Figure 2.9. The predominant type I semiconductor NC is CdSe/ZnS. The direct isolation of the core through wide-gap over-coating provides a simple pathway to limit the effect of surface trapping on observed dynamics.[20] The increased passivation results in increased quantum yield,[72] and subsequently long-lived stimulated emission.[33]

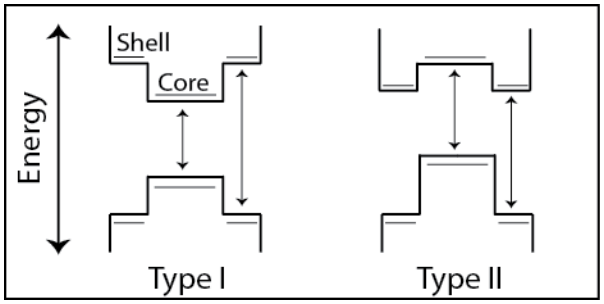

Figure 2.9 - Band Structures for ideal type I and type II heteronanostructures.

More interesting, though, is the subtlety of the band-edge bleach which will be discussed later. Generally, the band-edge bleach of CdSe/ZnS/Ligand is well fit to a bi-exponential decay which is consistent with the doubly-degenerate S-type electronic state.[32] This result holds, in the case of CdSe/ZnS/Ligand, irrespective of fluence or initially excited state.[73] However, in the case of CdSe/Ligand systems, as discussed previously, eased coupling to the surface presents multiple relaxation pathways which impede analysis.[32]

The primary interest in type II heterostructures, beyond simple surface passivation, is the ability to directly alter boundary conditions as a path towards wave function engineering. Through tailoring shell material and size, one can localize either the electron or the hole in the shell thereby manipulating Auger recombination rates as well as multiexcitonic interaction mechanisms.[39, 74]

Due to the level of synthetic control through colloidal chemistry the possibilities for type II configurations span Dot-in-Dot [39, 40, 43, 74, 75] to Dot-in-Rod [76]. The invocation of spatial localization has made single excitonic gain possible [39] and allowed for direct investigation of the involvement of the hole in Auger recombination and phonon-bottlenecks.[74] The ‘1-dimenisonal’ nature of quantum rods also provides interesting polarization dependence to spontaneous emission.[77]

2.3.3 – Exotic and Giant Nanocrystals

The possibility for wavefunction engineering through chemical control is as vast as the imagination, and lattice mismatch, allows. For example, chemical overcoating need not end with barrier/shell systems as in the case of CdSe/ZnS. Multiple barrier/shell combinations, such as those originally demonstrated by Peng et al., can provide dual-colour emission in a single NC system.[78] Similarly, through passivation of a core by a ‘giant’ shell, the sharp potential barrier between core and shell may be smoothed, having important implications in Auger recombination and blinking,[41, 79] as can be seen in Figure 2.10. These exotic NC systems provide two immediate advantages: the core/barrier/shell systems allow for direct investigation of the effect of relative component composition and diameter on the two-colour emission spectrum as well as charge transfer between core and shell, and the giant NCs provide insight into the mechanism behind NC blinking.[79]

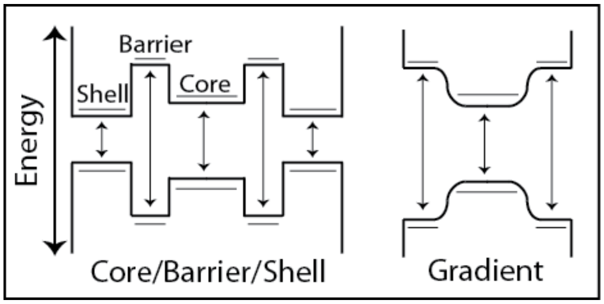

Figure 2.10 – Exotic bandstructures for multi-shell and giant nanocrystals

The interest in core/barrier/shell systems comes through tuning the relative core and shell sizes thereby manipulating the relative core/shell band gaps. Similarly, the wide-gap barrier can be further tuned to span the type-I and type-II regimes through control of hole or electron wavefunction tunnelling between core and shell.[80]

2.3.4 – Doped and Alloyed Nanocrystals

The controlled addition of atomic impurities in bulk semiconductors is known as doping. The now extrinsic semiconductor may have controlled regions which are either electron rich (N-type) or hole rich (P-Type).

As with bulk phenomena, there exists a great deal of interest in doped or alloyed semiconductor NCs, doping represents yet another possible avenue for wave-function engineering within semiconductor NCs.[8, 81, 82] However, the miniscule diameter to which the NC owes its unique optical properties inherently complicates the doping process: the potential exists for dopants to diffuse to the surface thereby muddling their influence on the core system complicates the chemistry.[8]

For example, the interstitial addition of Tellurium to CdSe has led to interesting effect on multiexcitonic interactions.[7] Similar to Type-II systems, the Tellurium defect site acts as a hole-trap, removing the free-exciton Columbic interaction and replacing with confined-hole repulsion. Through tailoring the excitonic interaction from stabilizing to repulsive (and subsequently shifting the parasitic induced absorption away from the single-exciton emittive state), tellurium doping could lead to low-lasing thresholds as demonstrated by Klimov et al.[39]

2.3.5 – Emission from the Near-IR to the Ultra Violet

A NC of a given material emits and absorbs over a given wavelength range. For example, although ultra-small sub 3 nm CdSe NCs have been developed to absorb in the near ultraviolet regime,[12] CdSe NCs tend to absorb through the visible spectrum.[9] While broadband absorption throughout the visible and near-IR is valuable to a photovoltaic, any practical optoelectronic device would require lasing wavelengths within the telecom window of 1.3 μm to 1.6 μm. Luckily, there exists a material-based tailoring scheme to span from the ultraviolet to the near-IR.

CdSe absorbs and emits in the visible spectrum along with InP and CdTe as determined by their bulk band-gap. CdS may also emit within the visible, however, it may be primarily due to surface emission, as will be discussed later.[16] The confined band-gap, and subsequent emission profiles, can only be greater in energy than the bulk-band gap. A few bulk band gaps for materials commonly made into NCs along with their respective NC emission windows are listed in Table 2.1

Table 2.1 – Comparison of common nanocrystals and their respective bulk band-gaps

Material	Bulk Eg (300k)	Bulk Eg	Nanocrystal Absorption
CdSe	1.73 eV	~716 nm	Visible
CdTe	1.49 eV	~832 nm	Visible
ZnS	3.6 eV	~344 nm	Ultraviolet
PbS	0.37 eV	~3.35 μm	Infrared
PbSe	0.27 eV	~4.6 μm	Infrared

The world of telecommunications is dominated by the near-infrared spectrum. Any design involving optical switches or modulators should comfortably operate within the telecommunications window of roughly 1.55 μm. From the Table above, it is immediately apparent that CdSe, barring tailored surface or defect emission, is an inappropriate candidate. The lead salts have demonstrated optical gain in the infrared [83] however; the band-edge transition is 8-fold degenerate, requiring intense photon flux to achieve population inversion.

2.4 – Dynamics

The myriad of radiative and non-radiative pathways present within a given NC leads to a complicated and convoluted discussion of observed exciton dynamics, as summarized in Figure 2.11. The difficulty arises in that a given population lifetime is a combination of both radiative and non-radiative pathways.[24, 25, 84, 85] Radiative kinetics can be investigated through time-resolved photoluminescence techniques.[84, 86] However, in order to investigate nonradiative dynamics, pump-probe transient absorption spectroscopy is required. [24, 25]

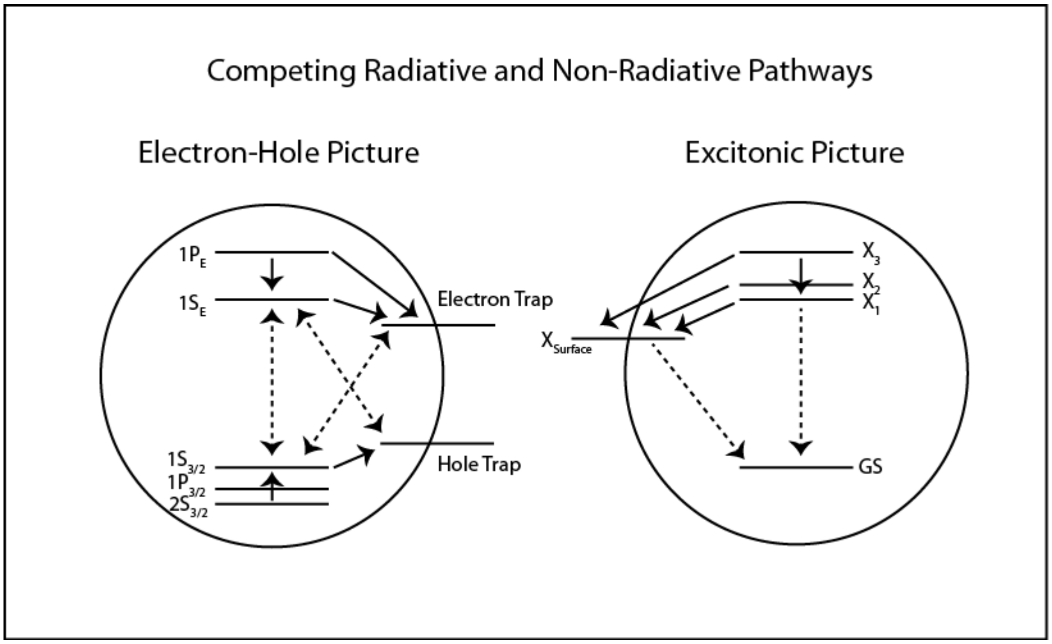

Figure 2.11 – Relaxation pathways for exciton-hole and excitonic pictures respectively.

Great efforts have been made to deconvolve the various contributions in order to provide a complete quantitative picture. Klimov et al. demonstrated the first direct measurement of relaxation dynamics in CdSe films.[85, 87] Knowles et al. provide a description of the radiative and non-radiative relaxation dynamics through combined time-resolved photoluminescence and visible/near-IR transient absorption spectroscopy.[88] Kambhampati et al. made use of state-resolved transient absorption spectroscopy in an effort to isolate given state-filling and auger recombination dynamics [30, 89, 90] to elucidate the relative many-body excitonic interactions.[25, 58] Guyot-Sionnest provides evidence of the holes involvement in auger recombination through spatially localizing the hole in an inorganic over coating thereby greatly increasing the band edge lifetime.[74]

Ultimately, the complex competition kinetics present within a NC muddles discussion. However, through combined spectroscopic methods and careful investigation; one can develop a first order picture of the relative dynamics.

2.4.1 – Continuous wave Photoluminescence and Linear Absorption

Linear absorption, as described in the previous chapter, provides a basic measurement involving only a single light-mater interaction. More specifically, it provides steady-state transition information. In the case of semiconductor NCs, it provides the single-excitonic absorption spectrum, or $OD_{0.}$ Conveniently, the linear spectrum may also provide a simple method for calculating the concentration of a given sample so long as the extinction coefficient is known.[91]

In the case of a few standard NCs, the extinction coefficient has been experimentally determined through empirical investigation and has been found to be strongly size-dependent.[91] Similarly, through rigorous empirical investigation, a yardstick for estimation of particle size as a function of band-edge absorption was provided for CdSe [91]:

$$D = (1.6122 \times 10^{-9}\lambda^4) - (2.6575 \times 10^{-6}\lambda^3) + (1.6242 \times 10^{-3}\lambda^2) - (0.4277\lambda) + 41.57 \qquad (2.19)$$

where D is particle diameter and λ is the bandedge wavelength. When applied in concert with described EMA theory, this sizing curve provides a 1st order approximation of a given particle radius based on OD_0 simplifying size-dependent studies. Of course, this is a first order approximation, albeit a powerful one, and is not an absolute substitute for sizing through transmission electron microscopy.

The linear absorption spectrum is limited to discussing steady-state single excitation regimes, however, through the rich temperature dependent absorption and fluorescence lineshape analysis much can be, and has been, learned. The question remains: what happens in the event of multiple excitons? Is there an analogous fine-structure to the biexciton, or multiple excitonic spectra? Non-linear spectroscopy, or single-dot spectroscopy for that matter, provide just such an avenue of exploration.

2.4.2 – Pump Probe Signatures

The primary spectroscopy technique used throughout this dissertation is pump-probe spectroscopy. The ‘discreet’ nature of the excitonic transitions within the semiconductor NC makes for an intriguing investigation through state-specific pump-probe spectroscopy.[24] For example, hot charge-carrier relaxation dynamics may be directly studied through time-domain transient absorption.[24, 85] Multi-excitonic multiplicity and relative binding energies can be discerned through transient absorption spectroscopy.[25] In order to guide discussion, the signals pertinent to discussion of semiconductor quantum dot dynamics will be discussed below, in terms of pump-probe spectroscopy.

2.4.2.1 –State Filling Dynamics

A typical transient absorption spectrum, for the prototypical system CdSe, after high energy excitation is shown in Figure 2.12; two regions of interest exist:

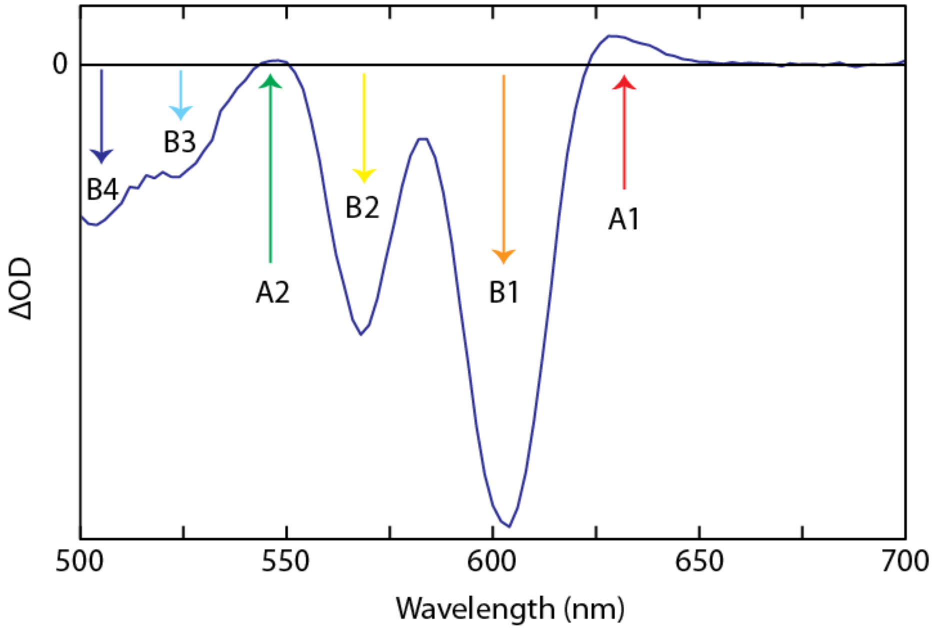

Figure 2.12 - Transient absorption spectrum of CdSe after pumping with low fluence 3.1 eV excitation at t = 0.4 ps.

those involving positive going signals, or, induced absorptions, and those with negative signals: bleach and stimulated emission. The labels given to the prominent features are, as listed, A1 and A2 for the induced absorptions, and B1, B2, B3, and B4 for the bleaches.[87] The bleaches correspond to the excitonic states as described by the linear absorption spectrum.[20, 92] Immediately obvious is the information to be gained through transient lifetimes of the bleaches with proper excitation, Auger recombination rates and state filling dynamics.[20, 24, 25, 84, 87]

A powerful technique to elucidate the intra-band dynamics, barring availability of infrared spectroscopy,[88, 93-96] is the state-dependent differential pump probe technique or, more simply, ΔΔOD.[30, 90] Simultaneously exciting two distinct states, and subsequently probing a third, provides direct comparison between relaxation dynamics of the excited states as shown in Figure 2.13. In the case of CdSe/ZnS, the X_3 and X_1 transitions share separate electronic states; the X_1 arising from a $1S_E$ state and the X_3 arising from a P-type state. Similarly, the X_1 and X_2 state share an electronic state and differ solely in hole states: X_1 being $1S_{3/2}$ and X_2 being $2S_{3/2}$.The state-resolved differential transient absorption technique can, in these cases, be used to isolate the dynamical contributions of interest. For example, the early-time B1 transition, in the case of X_1 and X_2 pumping, is an IRF limited bleach whereas excitation into X_3 or higher shows a build-up of a few picoseconds, consistent with state-filling between $1S_E$ and $1P_E$ states.[24]

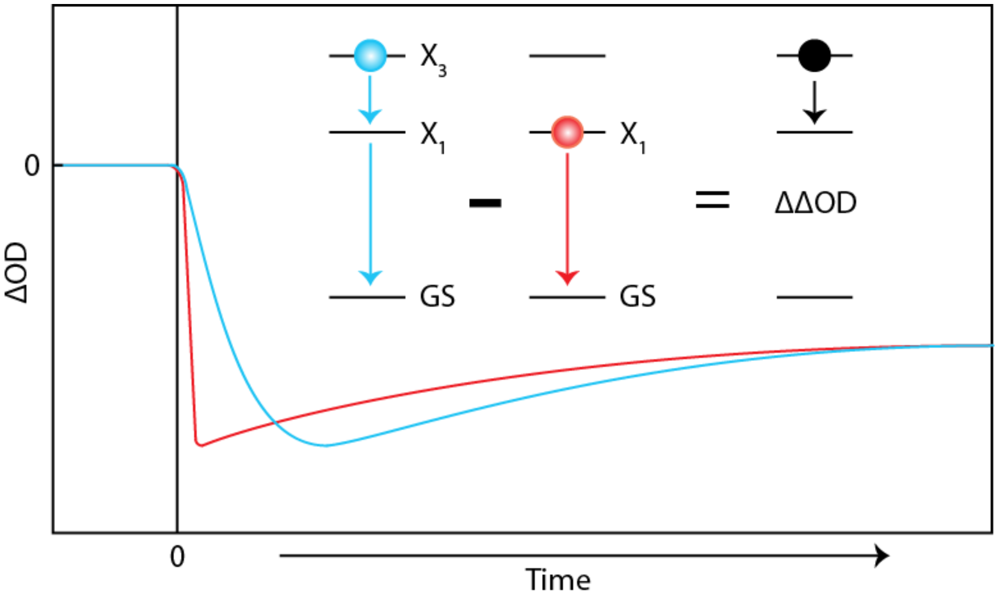

Figure 2.13 – Graphical representation of ΔΔOD measurement. Shared electronic excited state leads to differential method for determining relative relaxation rate of hot hole or hot electron.

The state-resolved technique provides a window into relative coupled transitions within the system not just through decay rates, but also through more subtle spectral signals. For example, the band-edge and X_2 transitions for CdSe/ZnS are nominally considered S-Type within the EMA approximation. If these transitions shared some electronic state with the higher-lying transitions, any reduction in population of the joint electronic state would manifest itself in all the coupled transitions as shown in Figure 2.14. However, no higher-lying states would be populated. This unique shared electronic state can be seen through a so-called isosbestic point in the non-linear spectrum.[33] Pumping the X_1 transition results in slight bleach to the X_2 due to the shared $1S_E$ electronic state, but has no effect on the P-type electronic higher-lying transitions resulting in the isosbestic point just to the blue of the X_2 transition.

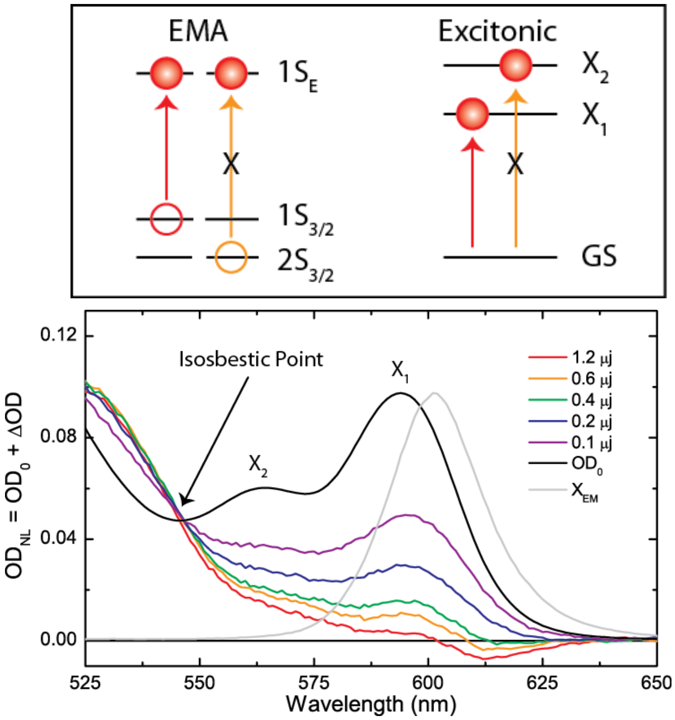

Figure 2.14 – Shared electronic state leads to blocked-absorption. Transient absorption spectra shows isosbestic point between X2 and X3 transitions.

2.4.2.2 –Auger Relaxation and Breaking the Phonon Bottleneck

The symmetry of conduction (electron) and valence (hole) bands in a given semiconductor has strong influence on observed dynamics.[74, 97-101] Unlike in bulk material, hot charge carriers were first thought to be limited in relaxation dynamics as, due to possessing intra-band energy spacing greater than observed phonon frequencies could accommodate, a hot carrier confined within a given CdSe NC would have to couple excess energy through multi-phonon processes in order to relax to the lowest excited state and radiatively recombine. Since the relative intraband spacing is size-dependent, increasing with decreased particle radius, the bottleneck was expected to be pronounced in smaller, strongly confined dots. This was the so-called 'phonon bottleneck'. However, early era work by Klimov et al. demonstrated not only fast electronic relaxation in CdSe NCs,[92] but an increase in electronic relaxation rate with decreased particle size. This was attributed to an Auger up-pumping of the hole by the hot-electron made possible through a more densely packed valence band (Figure 2.15). This new Auger relaxation channel was later supported through work by Guyot-Sionnest via decoupling the hole from the electron thereby slowing electronic relaxation.[74, 95]

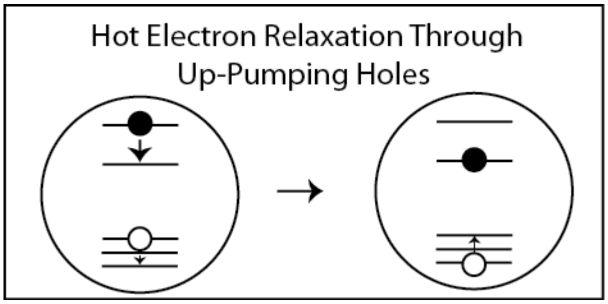

Figure 2.15 – Asymmetric band spacing leads to efficient electronic relaxation through up-pumping hole state

Electronic relaxation, in the case of asymmetric conduction and valence bands, proceeds through Auger process. However, the subsequent relaxation of the hot-hole would then dominate the observed dynamics as, once again, coupling to Longitudinal Optical (LO) phonons provides only roughly 25meV of energy in CdSe (LO frequency being roughly 208 cm^{-1}).[102] Ab initio experiments have similarly suggested the resurgence of the phonon-bottleneck for the final two hole states in CdSe.[99, 103] However, work by Cooney et al.

demonstrated a second relaxation channel for holes in CdSe through a non-adiabatic pathway via coupling to low-frequency phonons assisted by surface ligands.[73] This non-adiabatic channel was further supported by a slowing of the relative hole relaxation dynamics with addition of an inorganic ZnS shell. The inorganic shell acts as a barrier decoupling the ligand assisted non-adiabatic channel.[22, 68, 73]

2.4.2.3 – Phonons in Nanocrystals

The arguments above rely heavily on the knowledge of the relative frequencies of phonon modes of the NC. In fact, phonon coupling dominates a large portion of NC physics from the observed temperature dependence of emission and absorption linewidths, both of the core and the surface state.[24, 28, 68, 70, 71, 104-106] Coupling to acoustic phonons has also been suggested to play a role in the Stokes shift in CdSe along with the valence band splitting discussed earlier.[28, 29]

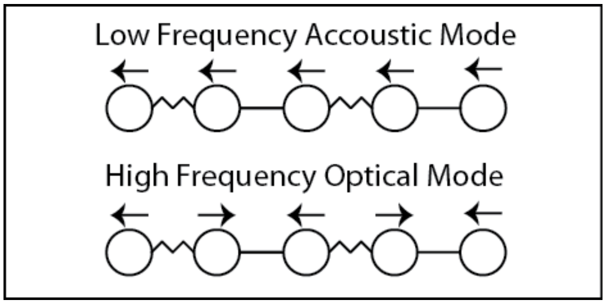

Figure 2.16 – Cartoon representation of two contributing phonon modes.

A phonon is a normal mode of vibration within a crystal lattice. These lattice vibrations provide an efficient mechanism for dissipating excess energy in the bulk. If a given crystal is made up of two differing symmetries, for example two separate atoms, with differing bond strengths, such as CdSe, the phonons dispersion curve will minimally be described by two bands: the acoustic phonon band which represents an in-phase oscillation between two differing interionic bonds, and the optical band, an out of phase oscillation, as depicted in Figure

2.16. Nominally, the optical phonon coupling occurs through the long-range Fröhlich polaron mechanism wherein the optically excited charge-carrier cloud interacts with the vibrations of the ionic lattice.[28, 29, 57, 73, 102] The lower frequency acoustic phonon modes may arise through either piezoelectric coupling or the deformation potential.[28, 29, 57, 107] The acoustic mode, in the case of CdSe NCs, is attributed to a spherical breathing mode.[29]

The significance of stretching and compressing a given unit cell in terms of an NC comes when one considers that the energy spacing, and the band gap itself, is affected by inter-atomic distances. Resonant excitation of a sample through broad-band ultra-short laser pulses can create excited state wave packets [108] as shown in Figure 2.17. As discussed in the previous chapter, these vibrations (and their subsequent influence on the energy-gap) may be described in terms of the displaced harmonic oscillator picture and the appropriate energy-gap correlation functions.[28] The magnitude of the coupling between these excited electronic wavepackets and nuclear vibration is described through the Huang-Rhyse parameter, $S = \Delta^2/2$, within the Frank-Condon approximation [29] where electronic transitions occur at a much faster timescale than nuclear motion.[108] The displacement between ground and excited state along the dimensionless phonon coordinate, Q, is given by Δ.[29] During impulsive pump-probe transient absorption spectroscopy, these

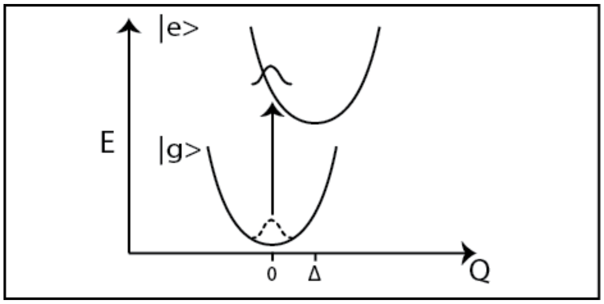

Figure 2.17 – Simplified DHO picture showing launched coherent wavepacket through excitation by impulsive pump pulse.

oscillations manifest themselves through frequency modulation of the differential absorption spectrum,[73, 102] as depicted in Figure 2.18.

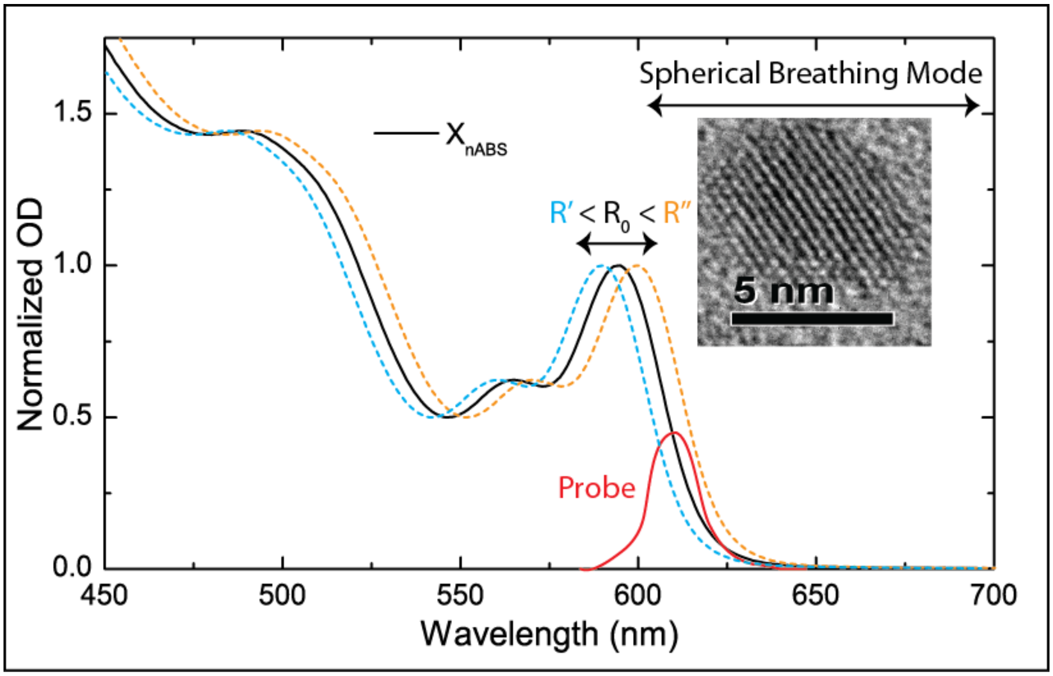

Figure 2.18 – Coherent oscillations, or phonons, launched through impulsive excitation by short optical pulse leads to frequency modulation of the absorption spectrum in nanocrystals.

2.4.2.4 – Multiexcitonic Binding Energies and Induced Absorptions

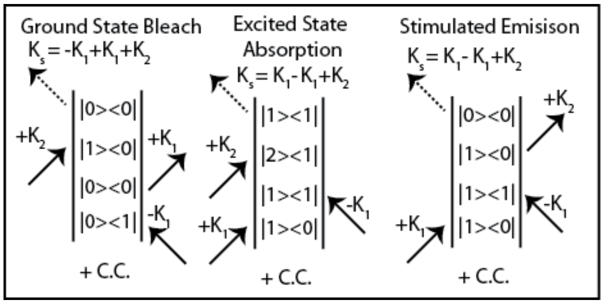

Figure 2.19 - Three of six Feynman diagrams contributing to the pump probe signal. C.C. denotes complex conjugate.

In terms of multiexcitonic interactions, the induced absorption features provide an information rich signal. Consider the two-sided Feynman diagrams, as described in the first chapter, for the three major components to a pump-probe signal as applied to a three-level absorbing system, as shown in Figure 2.19. Further assume that first transition creates a single exciton and the second absorbing transition is that of a bound biexciton. This biexciton is stabilized via cross-Colombic interaction and therefore its transition energy is slightly red-shifted from the single excitonic state, ie: $E_{XX} < E_{X+X}$. A pump pulse of any given intensity incident on the sample can create two situations:

1) Ground state bleaching: where E_1 pump field creates coherence between the ground and excited state. The subsequent E_1^*, decoheres the state.
2) Excited State Absorption/Stimulated emission: The pump fields E_1 and E_1^* create a population through subsequent interaction with the samples.

The probe pulse, or E_2, can then interact in any of three ways:

1) It can cause the stimulated emission of the population created by $E_1E_1^*$ interaction, leading to an increase in the detected signal at the resonant frequency of the inverted transition, leading to a negative going signal in the differential absorption spectrum through heterodyning the third order polarization with the probe pulse.
2) It can be absorbed into the higher-lying state and create a coherence between the |2> and |1>, resulting in a reduction of the detected signal at the second transition frequency leading to a positive going signal in the differential absorption spectrum through heterodyning the third order polarization with the probe pulse.
3) It can create a coherence between |1> and <0| leading to a reduction in the detected signal at the first transition frequency, leading to a negative-going signal in the differential absorption spectrum through heterodyning the third order polarization with the probe pulse.

These three competing processes all contribute to the overall transient absorption spectrum. The effect of the relative overlap between the two transitions, ΔXX, can be seen in Figure 2.20.

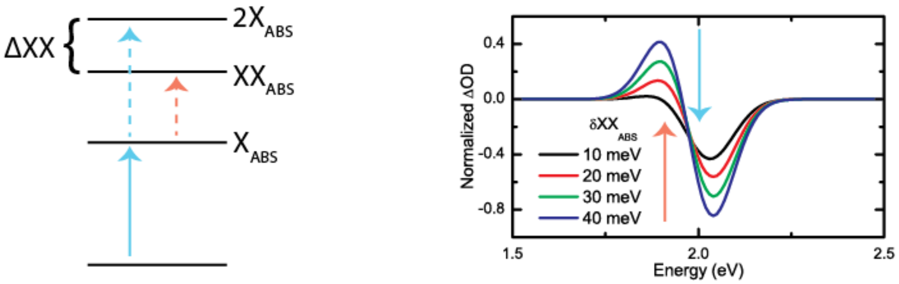

Figure 1.20 – Simplified three-level system involving single and multi-excitonic absorption. Spectral dependence of bi-excitonic binding energy.

The early time transient absorption spectrum for CdSe can be intuitively interpreted by this simple, 0th order model, excluding surface trapping which will be discussed in later sections. The binding energy for a given multiexciton is measured through the A1 transition. In NCs, the biexciton binding energy is dependent on the initially pumped state, ie, $\Delta XX_{|1Pe:1Se>} > \Delta XX_{|1Se:1Se>}$. In this case, the increased ΔXX comes through the state-dependence of the combined biexcitonic energy, as shown in Figure 2.19. The use of CdSe/ZnS is subtly pertinent as it limits the contribution of the surface trapping signal to the A1 transition. While the excited-state absorption features, at least under low fluence, can be readily visualized in the transient absorption spectrum, the difficulty comes in extracting the relative contributions between stimulated emission and bleach.

Valuable information, however, can be established from the linear absorption spectrum described in the previous section. The linear absorption spectrum, in the case of NCs, provides the single-excitonic absorption spectrum, or, OD_0. This is analogous to the 'pump off' spectrum in a pump-probe experiment. Consider the respective Feynman diagrams as depicted in Figure 2.19. With the absence of the pump pulse, $E_{pump} = E_1 + E_1^*$, and its subsequent interactions, the diagram regresses to that of the first order, or linear absorption, spectrum. Now, with the inclusion of a resonant pump, the difference between stimulated emission and bleach can be demonstrated. The pump-off, or linear spectrum, represents the maximum absorption as experienced by the probe pulse, as shown in Figure 2.6. This signal can then be added to the differential absorption spectrum (ΔOD) to obtain the non-linear spectrum:

$$OD_{NL} = OD_0 + \Delta OD \tag{2.20}$$

The main features of interest, in the case of OD_{NL}, are when $OD_{NL} < 0$ as this represents a net-gain of detected signal over and above the intensity of the probe, which is indicative of stimulated emission. Therefore, through direct consideration of both the differential absorption spectrum (ΔOD) and the non-linear spectrum (OD_{NL}), one can directly observe the contributions of ground state bleach, excited state absorption, and stimulated emission to the pump-probe signal.

2.4.2.5 – Optical Gain and Lasing

With the discovery of the semiconductor NC, all eyes were on the promising prize of a size-tunable gain medium with low lasing thresholds, simple processing, and incredibly small size.[109] The pioneering work in optical gain, and its subsequent improvement, was performed by Bawendi and Klimov.[110-115] Though this work demonstrated optical gain, it brought about a harsh reality. Lasing thresholds were high, the previously solvated NCs had to be embedded in films and the most sought after size-tunability and universality was lost. In order to explain the discrepancies, the parasitic induced absorption of a multiexciton (as discussed in previous sections) and its competition with the emission from a given excitonic state was proposed by Malko et al.[111] to be the limiting factor when considering optical gain in semiconductors. In order to circumvent this competing signature, Klimov et al. developed type-II CdS/ZnSe NCs [39] which spatially localized the hole in the ZnSe shell. This separation and spatial localization removed the cross-columbic stabilization between excitons thereby tailoring the multiexcitonic interaction towards favoring single excitonic emission. These type-II heteronanostructures demonstrated low-threshold optical gain and amplified stimulated emission, as well as tuneability between single and multiexcitonic stimulated emission.[39] This was, in many ways, a definite example of the importance of wavefunction engineering on NCs as a platform for optical gain. Although powerful, the work by Klimov et al. failed to address two key degrees of freedom presented by NCs: the state-specific prescription of excitonic populations, and, the surface.

Through state-resolved prescription of the population inversion, Cooney et al.[33, 116] demonstrated size-independent, universal optical gain for colloidal CdSe and CdSe/ZnS in solution, albeit with high fluence excitation. Moreover, they demonstrated the finer elements of the interplay between multiexcitonic emission and absorption. This understanding led to the demonstration of optical gain in novel core/barrier/shell NCs demonstrating broad bandwidths.[56] In fact, colloidal quantum dots have been manufactured into Vertical Cavity Surface Emitting Lasers (VCEL) [117] and have demonstrated optical logic [61] which will be discussed in detail later. With the increasingly broad NC synthesis literature, a qualitative description of the exctionics behind optical gain would provide a roadmap towards intelligent design of future, novel nanostructures. This understanding can only come through careful, state-specific spectroscopic analysis of the excitonic environment.[58]

The care comes when one considers that optical gain, as discussed in the previous chapter, requires a population inversion. In the case of the engineered emitter CdSe/ZnSe as described by Klimov et al. [39], population inversion was tunable between single and biexcitonic with increased photon flux leading to distinguishable stimulated emission spectra. The intrigue comes when one considers the mechanism. The excitonic interactions were such that there was a strong Stark effect blue shifting the XX_{ABS} transition away from the X_{EM} resulting in two distinct possible transitions whose stimulated emission were spectrally separated. In the case of the basic CdSe NC, as described by Cooney et al., the population inversion was multiexctionic in nature with its specific multiplicity dictated by the degeneracy of the state being populated.[33, 116] In other words, there existed a state-to-state degree of freedom when studying optical gain. The reason for this comes when one considers the exciton-excition interactions within the NC, or, the multiexcitonic fine structure.[30] This will be discussed in length in later chapters.

2.4.2.6 – Multiple Exciton Generation

Multiple exciton generation (MEG) represents a vast portion of the applied semiconductor literature. The broad visible absorption typical of NCs and proposed generation of multiple excitons per single photon absorbed represents an ideal photovoltaic.[31, 118-120] While MEG has been demonstrated for various NC systems, there remains controversy with the disclosed yields [121] and measurement methods.[32]

Multiple exciton generation (MEG) is the process where a high energy photon creates an exciton deep in the manifold of states; this high-energy exciton then generates another exciton of lesser energy through leaving a net gain of two excitons for a single photon. The multiple low-energy excitons may relax through multi-carrier recombination processes. In fact, it is the presence of multi-exponential character to the decay for low fluence excitiation (<N> ~ ½) and the relative A/B ratio which was used as evidence for MEG in NCs.[32]

2.5 – Surface Treatments

As the previous sections have made abundantly clear: the surface of the NC is paramount in all discussions of dynamics, applications, and theory. In fact, due to a NCs diameter, through simple surface area to volume arguments, the surface of the NC must be a predominant topic in any discussion of semiconductor NCs. Ultimately, the surface of the crystal is not a static, perfectly infinite potential barrier to its surroundings as there exist mobile, vibrant, and very real ligands which can not only directly affect the optical properties of the dot in the steady state, but play a role in the charge trapping dynamics as well.[16, 24, 32, 68, 70, 71, 84, 105, 107, 122-131] In fact, the 'real' surface dictates most of the desired practical applications of the NC. For example, surface trapping limits emission lifetimes and increases fluence requirements for optical gain.[33, 116] Similarly, in order to construct an efficient and functional photovoltaic, collected charges must be extractable: this process will inherently incorporate the surface. Emission energies and bandwidths can be tailored through an understanding of the surface energy landscape, from using ligands to quench emission entirely [70, 122, 128, 132-134], to developing broadband, white light emitters.[10, 12, 135]

2.5.1 – Ligands: Forgotten, but not Lost.

The ideal picture of a semiconductor NC, at least in terms of the original analytical approach to its theory, embodies a complete energetic isolation to surroundings through benevolent, non-interacting ligands. This is the particle in a sphere approximation. Despite its descriptive convenience, the invocation of infinite potential barriers is, at its core, an over simplification of the physical reality.[10, 101, 125, 129, 133, 136-140] The ligands, present due to the colloidal chemistry required, are themselves dynamic and either through small conformational changes or solution equilibrium can generate strong dipole moments [22, 68, 101, 141, 142], quench emission [133], and greatly impact optical and electrochemical properties and solubility of the dot.[143-146]

Due to the nature of colloidal chemistry, and the solubility of the relevant precursor materials, the ligands involved are often surfactants necessary for the solvation of the NC. Removal of these ligands could result in the aggregation of the NCs to more stable bulk material which would subsequently drop out of solution.

Of course, the seemingly direct method to avoid the obfuscating effects of the ligands on the study of core of the NC is to make use of a wide band-gap inorganic shell as discussed in the previous sections. However, these shells themselves, if not properly controlled, can impact the optical properties and dynamics through directly affecting the excitonic interactions within the system.[147] Fundamentally, the surface has a strong role to play in any and all discussions of wavefunction engineering.[10, 16]

2.5.2 – Temperature Dependence of Surface Emission

The temperature dependence of the broadband surface emission lends a wealth of information pertaining to the interaction of the core with the surface state. The relative intensities of the surface and core emission, as well as the respective linewidths, provide information pertaining to the excitonic environment and kinetic equilibrium of the surface.

A number of studies have been performed [15, 16, 28], and subsequent models proposed [15, 16, 28, 148-150], in an effort to both qualitatively and quantitatively described the surface/core energy landscape. Initially, the temperature dependence was ascribed to deep-trap states caused by the surface of the NC, for example, through hole-trapping at Se dangling bonds. Similarly, the 'dark-exciton' state was proposed in light of the core emission state narrowing with temperature.[13, 151] A classical Marcus-type electron transfer model was proposed by Scholes et al. in an effort to explain the observed temperature dependence on the observed spectral features.[28]

Recently, a thorough temperature dependent investigation of the steady-state absorptive and emittive properties of the core and surface state for various NCs has led to a semi-classical Marcus-Jortner electron-transfer treatment of the surface state.[16] This model extends the classical Marcus treatment as provided by Scholes with the inclusion of quantum mechanical treatment of the vibronic coupling between surface and excited excitonic states, as discussed in chapter 1. It not only provides a pathway for engineering the core emission properties of a given designer NC, but also alludes to the potential for engineering the surface emission profiles for white-light emission.[10] This model could be further extended through state and temperature-dependent ultrafast phonon studies.

2.5.3 – Pump Probe Surface Signatures

In previous sections the contribution of multiexcitonic induced absorption to the transient absorption spectrum was discussed but it was not the complete picture. What about the surface?

Since, inherently, a transient signature of a given state is governed by the population in that state, and said population is dependent on both the relative radiative and non-radiative relaxation processes occurring within the system, any subsequent competitive population reducing channel would manifest itself in the decay rate. Assuming Auger recombination and state filling processes dominate the ‘band-edge’ bleach dynamics, if pumped at higher energy, would only demonstrate, at most, bi-exponential decay: a quick recovery for XX into X, and a slower recover of X to ground state. Now, if we include a new channel, that of surface trapping, the bleach dynamics may be multi-exponential in character. This vary issue surrounds the controversy behind the multiple exciton generation phenomena.[32] The MEG literature may, in many ways, act as a cautionary tale in terms of over-reaching interpretation of a given spectroscopic result.[32, 121]

Surface trapping signatures are not limited to transient decay rates. Consider a charge trapped impulsively at the surface, assuming the charge cloud was not uniformly distributed; this charge would create a local electric field. This electric field could alter the selection rules through symmetry breaking and present new optically allowed transitions.[152] These transitions would manifest themselves in the transient absorption spectrum. In fact, this phenomena has been recently demonstrated in CdSe/ligand NCs, along with control studies involving capped CdSe/ZnS.[57] The trapping, in this case, was attributed to hole trapping at the surface. The involvement of possible electron trapping, as well as further investigation of the pump-probe signatures involved in charge trapping, will be discussed in chapter 4.

2.7 – References

1. Rossetti, R., S. Nakahara, and L.E. Brus, Quantum size effects in the redox potentials, resonance Raman spectra, and electronic spectra of CdS crystallites in aqueous solution. The Journal of Chemical Physics, 1983. **79**(2): p. 1086-1088.
2. Efros, A.L. and M. Rosen, The electronic structure of semicondutor nanocrystals 1. Annual Review of Materials Science, 2000. **30**(1): p. 475-521.
3. Norris, D.J., Electronic Structure in Semiconductor Nanocrystals. Semiconductor and Metal Nanocrystals: Synthesis and Electronic and Optical Properties, ed. V.I. Klimov. 2005: CRC Press.
4. Wang, L.W. and A. Zunger, Pseudopotential-based multiband k center dot p method for similar to 250000-atom nanostructure systems. Physical Review B, 1996. **54**(16): p. 11417-11435.
5. Prezhdo, O.V., et al., Photoexcitation dynamics on the nanoscale. Quantum Dynamics of Complex Molecular Systems, 2007: p. 5-30.
6. Pankove, J.I., Optical Processes in Semiconductors. 1975: Dover.
7. Avidan, A. and D. Oron, Large blue shift of the biexciton state in tellurium doped CdSe colloidal quantum dots. Nano Letters, 2008. **8**(8): p. 2384-2387.
8. Erwin, S.C., et al., Doping semiconductor nanocrystals. Nature, 2005. **436**(7047): p. 91-94.
9. Murray, C.B., D.J. Norris, and M.G. Bawendi, Synthesis and characterization of nearly monodisperse CdE (E = sulfur, selenium, tellurium) semiconductor nanocrystallites. Journal of the American Chemical Society, 1993. **115**(19): p. 8706-8715.
10. Peng, Z.A. and X.G. Peng, Formation of high-quality CdTe, CdSe, and CdS nanocrystals using CdO as precursor. Journal of the American Chemical Society, 2001. **123**(1): p. 183-184.
11. N.W. Ashcroft, N.D.Mermin., Solid State Physics. 1976. Holt, Rinehart and Winston.
12. Harrell, S.M., J.R. McBride, and S.J. Rosenthal, Synthesis of Ultrasmall and Magic-Sized CdSe Nanocrystals. Chemistry of Materials, 2013.

13. Califano, M., A. Franceschetti, and A. Zunger, Temperature dependence of excitonic radiative decay in CdSe quantum dots: The role of surface hole traps. Nano Letters, 2005. **5**(12): p. 2360-2364.

14. Kazes, M., et al., Temperature dependence of optical gain in CdSe/ZnS quantum rods. Journal of Physical Chemistry C, 2007. **111**(22): p. 7898-7905.

15. Valerini, D., et al., Temperature dependence of the photoluminescence properties of colloidal CdSe⁄ZnS core/shell quantum dots embedded in a polystyrene matrix. Physical Review B, 2005. **71**(23): p. 235409.

16. Mooney, J., et al., Challenge to the deep-trap model of the surface in semiconductor nanocrystals. Physical Review B, 2013. **87**(8): p. 081201.

17. Jasieniak, J. and P. Mulvaney, From Cd-Rich to Se-Rich − the Manipulation of CdSe Nanocrystal Surface Stoichiometry. Journal of the American Chemical Society, 2007. **129**(10): p. 2841-2848.

18. Dresselhaus, G., Effective mass approximation for excitons. Journal of Physics and Chemistry of Solids, 1956. **1**(1–2): p. 14-22.

19. Elliott, R.J., Intensity of Optical Absorption by Excitons. Physical Review, 1957. **108**(6): p. 1384-1389.

20. Kambhampati, P., State-resolved exciton dynamics in quantum dots. 2010: p. 77580R-77580R.

21. Sewall, S.L., R.R. Cooney, and P. Kambhampati, Experimental tests of effective mass and atomistic approaches to quantum dot electronic structure: Ordering of electronic states. Applied Physics Letters, 2009. **94**(24): p. 243116.

22. Prezhdo, O.V., Photoinduced Dynamics in Semiconductor Quantum Dots: Insights from Time-Domain ab Initio Studies. Accounts of Chemical Research, 2009. **42**(12): p. 2005-2016.

23. Prezhdo, O.V., Multiple excitons and the electron-phonon bottleneck in semiconductor quantum dots: An ab initio perspective. Chemical Physics Letters, 2008. **460**(1-3): p. 1-9.

24. Kambhampati, P., Hot Exciton Relaxation Dynamics in Semiconductor Quantum Dots: Radiationless Transitions on the Nanoscale. The Journal of Physical Chemistry C, 2011. **115**(45): p. 22089-22109.

25. Kambhampati, P., Unraveling the Structure and Dynamics of Excitons in Semiconductor Quantum Dots. Accounts of Chemical Research, 2010. **44**(1): p. 1-13.

26. Fernee, M.J., et al., Acoustic phonon contributions to the emission spectrum of single CdSe nanocrystals. Journal of Physical Chemistry C, 2008. **112**(6): p. 1878-1884.

27. Kuno, M., et al., The band edge luminescence of surface modified CdSe nanocrystallites: Probing the luminescing state. The Journal of Chemical Physics, 1997. **106**(23): p. 9869-9882.

28. Salvador, M.R., M.W. Graham, and G.D. Scholes, Exciton-phonon coupling and disorder in the excited states of CdSe colloidal quantum dots. Journal of Chemical Physics, 2006. **125**(18).

29. Takagahara, T., Electron-phonon interactions in semiconductor nanocrystals. Journal of Luminescence, 1996. **70**: p. 129-143.

30. Sewall, S.L., et al., Direct observation of the structure of band-edge biexcitons in colloidal semiconductor CdSe quantum dots. Physical Review B, 2009. **80**(8): p. 081310.

31. Beard, M.C., et al., Multiple Exciton Generation in Colloidal Silicon Nanocrystals. Nano Letters, 2007. **7**(8): p. 2506-2512.

32. Tyagi, P. and P. Kambhampati, False multiple exciton recombination and multiple exciton generation signals in semiconductor quantum dots arise from surface charge trapping. The Journal of Chemical Physics, 2011. **134**(9): p. 094706-10.

33. Cooney, R.R., et al., State-resolved manipulations of optical gain in semiconductor quantum dots: Size universality, gain tailoring, and surface effects. Journal of Chemical Physics, 2009. **131**(16).

34. Newton, M.C. and P.A. Warburton, ZnO tetrapod nanocrystals. Materials Today, 2007. **10**(5): p. 50-54.

35. Manna, L., et al., Controlled growth of tetrapod-branched inorganic nanocrystals. Nature Materials, 2003. **2**(6): p. 382-385.

36. Chen, S.H., et al., Monopod, bipod, tripod, and tetrapod gold nanocrystals. Journal of the American Chemical Society, 2003. **125**(52): p. 16186-16187.

37. Dias, E.A., et al., Improving Optical Gain Performance in Semiconductor Quantum Dots via Coupled Quantum Shells. The Journal of Physical Chemistry C, 2012. **116**(9): p. 5407-5413.

38. Dias, E.A., S.L. Sewall, and P. Kambhampati, Light Harvesting and Carrier Transport in Core/Barrier/Shell Semiconductor Nanocrystals. The Journal of Physical Chemistry C, 2006. **111**(2): p. 708-713.

39. Klimov, V.I., et al., Single-exciton optical gain in semiconductor nanocrystals. Nature, 2007. **447**(7143): p. 441-446.

40. Hollingsworth, J.A., et al., 'Giant' multishell CdSe nanocrystal quantum dots with suppressed blinking: Novel fluorescent probes for real-time detection of single-molecule events. Colloidal Quantum Dots for Biomedical Applications Iv, 2009. **7189**.

41. Wang, X.Y., et al., Non-blinking semiconductor nanocrystals. Nature, 2009. **459**(7247): p. 686-689.

42. Bae, W.K., et al., Controlled Alloying of the Core-Shell Interface in CdSe/CdS Quantum Dots for Suppression of Auger Recombination. ACS Nano, 2013.

43. Kaniyankandy, S., S. Rawalekar, and H.N. Ghosh, Charge carrier cascade in Type II CdSe-CdTe graded core-shell interface. Journal of Materials Chemistry C, 2013. **1**(15): p. 2755-2763.

44. Qin, W., R.A. Shah, and P. Guyot-Sionnest, CdSeS/ZnS Alloyed Nanocrystal Lifetime and Blinking Studies under Electrochemical Control. Acs Nano, 2012. **6**(1): p. 912-918.

45. Wang, R., et al., Homogeneously-Alloyed CdTeSe Single-Sized Nanocrystals with Bandgap Photoluminescence. Journal of Physical Chemistry C, 2009. **113**(9): p. 3402-3408.

46. Ouyang, J., et al., Gradiently alloyed ZnxCd1-xS colloidal photoluminescent quantum dots synthesized via a noninjection one-pot approach. Journal of Physical Chemistry C, 2008. **112**(13): p. 4908-4919.

47. Tan, G.L., et al., Linear and non-linear optical properties of capped CdTe nanocrystals prepared by mechanical alloying. Optical Materials, 2004. **27**(3): p. 579-584.

48. Wang, L.G. and A. Zunger, Dilute nonisovalent (II-VI)-(III-V) semiconductor alloys: Monodoping, codoping, and cluster doping in ZnSe-GaAs. Physical Review B, 2003. **68**(12).

49. Dong, A., et al., Binary nanocrystal superlattice membranes self-assembled at the liquid-air interface. Nature, 2010. **466**(7305): p. 474-477.

50. Rosenthal, S.J., et al., Synthesis, surface studies, composition and structural characterization of CdSe, core/shell and biologically active nanocrystals. Surface Science Reports, 2007. **62**(4): p. 111-157.

51. Samanta, A., Z.T. Deng, and Y. Liu, Aqueous Synthesis of Glutathione-Capped CdTe/CdS/ZnS and CdTe/CdSe/ZnS Core/Shell/Shell Nanocrystal Heterostructures. Langmuir, 2012. **28**(21): p. 8205-8215.

52. Smyder, J.A. and T.D. Krauss, Coming attractions for semiconductor quantum dots. Materials Today, 2011. **14**(9): p. 382-387.

53. Zhao, M.X., et al., Targeted Cellular Uptake and siRNA Silencing by Quantum-Dot Nanoparticles Coated with beta-Cyclodextrin Coupled to Amino Acids. Chemistry-a European Journal, 2011. **17**(18): p. 5171-5179.

54. Sharma, S.N., et al., Surface modification of CdSe quantum dots for biosensing applications: Role of ligands. Thin Solid Films, 2010. **519**(3): p. 1202-1212.

55. Raymo, F.M. and I. Yildiz, Luminescent chemosensors based on semiconductor quantum dots. Physical Chemistry Chemical Physics, 2007. **9**(17): p. 2036-2043.

56. Dias, E.A., et al., Improving Optical Gain Performance in Semiconductor Quantum Dots via Coupled Quantum Shells. Journal of Physical Chemistry C, 2012. **116**(9): p. 5407-5413.

57. Tyagi, P., et al., Controlling Piezoelectric Response in Semiconductor Quantum Dots via Impulsive Charge Localization. Nano Letters, 2010. **10**(8): p. 3062-3067.

58. Kambhampati, P., Multiexcitons in Semiconductor Nanocrystals: A Platform for Optoelectronics at High Carrier Concentration. The Journal of Physical Chemistry Letters, 2012. **3**(9): p. 1182-1190.

59. Guyot-Sionnest, P., Electrical Transport in Colloidal Quantum Dot Films. Journal of Physical Chemistry Letters, 2012. **3**(9): p. 1169-1175.

60. Choi, J.H., et al., Bandlike Transport in Strongly Coupled and Doped Quantum Dot Solids: A Route to High-Performance Thin-Film Electronics. Nano Letters, 2012. **12**(5): p. 2631-2638.

61. Saari, J.I., et al., Terahertz Bandwidth All-Optical Modulation and Logic Using Multiexcitons in Semiconductor Nanocrystals. Nano Letters, 2013. **13**(2): p. 722-727.

62. McDaniel, H., et al., Engineered CuInSexS2-x Quantum Dots for Sensitized Solar Cells. Journal of Physical Chemistry Letters, 2013. **4**(3): p. 355-361.

63. Tang, J., et al., Colloidal-quantum-dot photovoltaics using atomic-ligand passivation. Nat Mater, 2011. **10**(10): p. 765-771.

64. Lin, Z.B., A. Franceschetti, and M.T. Lusk, Size Dependence of the Multiple Exciton Generation Rate in CdSe Quantum Dots. Acs Nano, 2011. **5**(4): p. 2503-2511.

65. Huynh, W.U., J.J. Dittmer, and A.P. Alivisatos, Hybrid nanorod-polymer solar cells. Science, 2002. **295**(5564): p. 2425-2427.

66. Frederick, M.T., V.A. Amin, and E.A. Weiss, Optical Properties of Strongly Coupled Quantum Dot-Ligand Systems. Journal of Physical Chemistry Letters, 2013. **4**(4): p. 634-640.

67. Frederick, M.T., et al., Control of Exciton Confinement in Quantum Dot-Organic Complexes through Energetic Alignment of Interfacial Orbitals. Nano Letters, 2013. **13**(1): p. 287-292.

68. Kilina, S., et al., Surface Ligands Increase Photoexcitation Relaxation Rates in CdSe Quantum Dots. Acs Nano, 2012. **6**(7): p. 6515-6524.

69. Knowles, K.E., M. Malicki, and E.A. Weiss, Dual-Time Scale Photoinduced Electron Transfer from PbS Quantum Dots to a Molecular Acceptor. Journal of the American Chemical Society, 2012. **134**(30): p. 12470-12473.

70. Zenkevich, E.I., et al., Influence of single dye molecules on temperature and time dependent optical properties of CdSe/ZnS quantum dots: Ensemble and single nanoassembly detection. Chemical Physics, 2012. **406**: p. 21-29.

71. Archana, J., et al., Effects of multiple organic ligands on size uniformity and optical properties of ZnSe quantum dots. Materials Research Bulletin, 2012. **47**(8): p. 1892-1897.

72. Talapin, D.V., et al., Highly Luminescent Monodisperse CdSe and CdSe/ZnS Nanocrystals Synthesized in a Hexadecylamine−Trioctylphosphine Oxide−Trioctylphospine Mixture. Nano Letters, 2001. **1**(4): p. 207-211.

73. Cooney, R.R., et al., Breaking the Phonon Bottleneck for Holes in Semiconductor Quantum Dots. Physical Review Letters, 2007. **98**(17): p. 177403.

74. Pandey, A. and P. Guyot-Sionnest, Slow Electron Cooling in Colloidal Quantum Dots. Science, 2008. **322**(5903): p. 929-932.

75. Dennis, A.M., et al., Suppressed Blinking and Auger Recombination in Near-Infrared Type-II InP/CdS Nanocrystal Quantum Dots. Nano Letters, 2012. **12**(11): p. 5545-5551.

76. Dorfs, D., et al., ZnSe quantum dots within CdS nanorods: A seeded-growth type-II system. Small, 2008. **4**(9): p. 1319-1323.

77. Carbone, L., et al., Synthesis and micrometer-scale assembly of colloidal CdSe/CdS nanorods prepared by a seeded growth approach. Nano Letters, 2007. **7**(10): p. 2942-2950.

78. Battaglia, D., B. Blackman, and X. Peng, Coupled and Decoupled Dual Quantum Systems in One Semiconductor Nanocrystal. Journal of the American Chemical Society, 2005. **127**(31): p. 10889-10897.

79. Chen, Y., et al., “Giant” Multishell CdSe Nanocrystal Quantum Dots with Suppressed Blinking. Journal of the American Chemical Society, 2008. **130**(15): p. 5026-5027.

80. Tyagi, P. and P. Kambhampati, Independent Control of Electron and Hole Localization in Core/Barrier/Shell Nanostructures. The Journal of Physical Chemistry C, 2012. **116**(14): p. 8154-8160.

81. Liu, H., S. Keuleyan, and P. Guyot-Sionnest, n- and p-Type HgTe Quantum Dot Films. Journal of Physical Chemistry C, 2012. **116**(1): p. 1344-1349.

82. Shim, M., et al., Doping and charging in colloidal semiconductor nanocrystals. Mrs Bulletin, 2001. **26**(12): p. 1005-1008.

83. Schaller, R.D., M.A. Petruska, and V.I. Klimov, Tunable Near-Infrared Optical Gain and Amplified Spontaneous Emission Using PbSe Nanocrystals. The Journal of Physical Chemistry B, 2003. **107**(50): p. 13765-13768.

84. Knowles, K.E., E.A. McArthur, and E.A. Weiss, A Multi-Timescale Map of Radiative and Nonradiative Decay Pathways for Excitons in CdSe Quantum Dots. Acs Nano, 2011. **5**(3): p. 2026-2035.

85. Klimov, V., et al., Carrier relaxation dynamics and ultrafast optical nonlinearities in semiconductor quantum dots. Nonlinear Optics: Materials, Fundamentals, and Applications, 2000. **46**: p. 140-142.

86. Jones, M., S.S. Lo, and G.D. Scholes, Signatures of Exciton Dynamics and Carrier Trapping in the Time-Resolved Photoluminescence of Colloidal CdSe Nanocrystals. Journal of Physical Chemistry C, 2009. **113**(43): p. 18632-18642.

87. Klimov, V.I., et al., Quantization of multiparticle Auger rates in semiconductor quantum dots. Science, 2000. **287**(5455): p. 1011-1013.

88. Knowles, K.E., E.A. McArthur, and E.A. Weiss, Multi-timescale map of radiative and nonradiative decay pathways for excitons in CdSe quantum dots. Abstracts of Papers of the American Chemical Society, 2011. **242**.

89. Cooney, R.R., et al., Unified picture of electron and hole relaxation pathways in semiconductor quantum dots. Physical Review B, 2007. **75**(24): p. 245311.

90. Sewall, S.L., et al., State-to-state exciton dynamics in semiconductor quantum dots. Physical Review B, 2006. **74**(23): p. 235328.

91. Yu, W.W., et al., Experimental Determination of the Extinction Coefficient of CdTe, CdSe, and CdS Nanocrystals. Chemistry of Materials, 2003. **15**(14): p. 2854-2860.

92. Klimov, V.I., et al., Mechanisms for intraband energy relaxation in semiconductor quantum dots: The role of electron-hole interactions. Physical Review B, 2000. **61**(20): p. 13349-13352.

93. McArthur, E.A., et al., Charge Carrier Resolved Relaxation of the First Excitonic State in CdSe Quantum Dots Probed with Near-Infrared Transient Absorption Spectroscopy. Journal of Physical Chemistry B, 2010. **114**(45): p. 14514-14520.

94. Wehrenberg, B.L., C.J. Wang, and P. Guyot-Sionnest, Interband and intraband optical studies of PbSe colloidal quantum dots. Journal of Physical Chemistry B, 2002. **106**(41): p. 10634-10640.

95. Guyot-Sionnest, P., et al., Intraband relaxation in CdSe quantum dots. Physical Review B, 1999. **60**(4): p. R2181-R2184.

96. Guyot-Sionnest, P. and M.A. Hines, Intraband transitions in semiconductor nanocrystals. Applied Physics Letters, 1998. **72**(6): p. 686-688.

97. Hyeon-Deuk, K., A.B. Madrid, and O.V. Prezhdo, Symmetric band structures and asymmetric ultrafast electron and hole relaxations in silicon and germanium quantum dots: time-domain ab initio simulation. Dalton Transactions, 2009. **0**(45): p. 10069-10077.

98. Kilina, S.V., et al., Ab initio time-domain study of phonon-assisted relaxation of charge carriers in a PbSe quantum dot. Journal of Physical Chemistry C, 2007. **111**(12): p. 4871-4878.

99. Kilina, S.V., D.S. Kilin, and O.V. Prezhdo, Breaking the Phonon Bottleneck in PbSe and CdSe Quantum Dots: Time-Domain Density Functional Theory of Charge Carrier Relaxation. Acs Nano, 2009. **3**(1): p. 93-99.

100. Achermann, M., et al., The effect of Auger heating on intraband carrier relaxation in semiconductor quantum rods. Nature Physics, 2006. **2**(8): p. 557-561.

101. Guyot-Sionnest, P., B. Wehrenberg, and D. Yu, Intraband relaxation in CdSe nanocrystals and the strong influence of the surface ligands. Journal of Chemical Physics, 2005. **123**(7).

102. Sagar, D.M., et al., State-resolved exciton - Phonon couplings in CdSe semiconductor quantum dots. Journal of Physical Chemistry C, 2008. **112**(25): p. 9124-9127.

103. Kilina, S.V., et al., Theoretical Study of Electron-Phonon Relaxation in PbSe and CdSe Quantum Dots: Evidence for Phonon Memory. Journal of Physical Chemistry C, 2011. **115**(44): p. 21641-21651.

104. Jaeger, H.M., S. Fischer, and O.V. Prezhdo, The role of surface defects in multi-exciton generation of lead selenide and silicon semiconductor quantum dots. Journal of Chemical Physics, 2012. **136**(6).

105. Qin, W. and P. Guyot-Sionnest, Evidence for the Role of Holes in Blinking: Negative and Oxidized CdSe/CdS Dots. Acs Nano, 2012. **6**(10): p. 9125-9132.

106. Fischer, S.A., C.M. Isborn, and O.V. Prezhdo, Excited states and optical absorption of small semiconducting clusters: Dopants, defects and charging. Chemical Science, 2011. **2**(3): p. 400-406.

107. Saari, J.I., et al., Ultrafast Electron Trapping at the Surface of Semiconductor Nanocrystals: Excitonic and Biexcitonic Processes. The Journal of Physical Chemistry B, 2012.

108. Kumar, A.T.N., et al., Investigations of ultrafast nuclear response induced by resonant and nonresonant laser pulses. The Journal of Chemical Physics, 2001. **114**(15): p. 6795-6815.

109. Krauss, T.D., Laser technology: Less excitement for more gain. Nature, 2007. **447**(7143): p. 385-386.

110. Maskaly, G.R., et al., Amplified spontaneous emission in semiconductor-nanocrystal/synthetic-opal composites: Optical-gain enhancement via a photonic crystal pseudogap. Advanced Materials, 2006. **18**(3): p. 343-+.

111. Malko, A.V., et al., Interplay between optical gain and photoinduced absorption in CdSe nanocrystals. Journal of Physical Chemistry B, 2004. **108**(17): p. 5250-5255.

112. Malko, A.V., et al., From amplified spontaneous emission to microring lasing using nanocrystal quantum dot solids. Applied Physics Letters, 2002. **81**(7): p. 1303-1305.

113. Klimov, V.I. and M.G. Bawendi, Ultrafast carrier dynamics, optical amplification, and lasing in nanocrystal quantum dots. Mrs Bulletin, 2001. **26**(12): p. 998-1004.

114. Klimov, V.I., et al., Stimulated emission and lasing in nanocrystal quantum dots. Quantum Confinement Vi: Nanostructured Materials and Devices, 2001. **2001**(19): p. 321-333.

115. Klimov, V.I., et al., Optical gain and stimulated emission in nanocrystal quantum dots. Science, 2000. **290**(5490): p. 314-317.

116. Cooney, R.R., et al., Gain Control in Semiconductor Quantum Dots via State-Resolved Optical Pumping. Physical Review Letters, 2009. **102**(12): p. 127404.

117. Dang, C., et al., Red, green and blue lasing enabled by single-exciton gain in colloidal quantum dot films. Nat Nano, 2012. **7**(5): p. 335-339.

118. Ellingson, R.J., et al., Highly efficient multiple exciton generation in colloidal PbSe and PbS quantum dots. Nano Letters, 2005. **5**(5): p. 865-871.

119. Talapin, D.V., et al., Prospects of Colloidal Nanocrystals for Electronic and Optoelectronic Applications. Chemical Reviews, 2010. **110**(1): p. 389-458.

120. Schaller, R.D., V.M. Agranovich, and V.I. Klimov, High-efficiency carrier multiplication through direct photogeneration of multi-excitons via virtual single-exciton states. Nature Physics, 2005. **1**(3): p. 189-194.

121. Nair, G., et al., Perspective on the Prospects of a Carrier Multiplication Nanocrystal Solar Cell. Nano Letters, 2011. **11**(5): p. 2145-2151.

122. Gallagher, S.A., et al., Efficient Quenching of TGA-Capped CdTe Quantum Dot Emission by a Surface-Coordinated Europium(III) Cyclen Complex. Inorganic Chemistry, 2013.

123. Wei, H.H.-Y., et al., Colloidal Semiconductor Quantum Dots with Tunable Surface Composition. Nano Letters, 2012. **12**(9): p. 4465-4471.

124. Gomez-Campos, F.M. and M. Califano, Hole Surface Trapping in CdSe Nanocrystals: Dynamics, Rate Fluctuations, and Implications for Blinking. Nano Letters, 2012. **12**(9): p. 4508-4517.

125. Chen, O., et al., Surface-Functionalization-Dependent Optical Properties of II-VI Semiconductor Nanocrystals. Journal of the American Chemical Society, 2011. **133**(43): p. 17504-17512.

126. Califano, M., Photoinduced Surface Trapping and the Observed Carrier Multiplication Yields in Static CdSe Nanocrystal Samples. Acs Nano, 2011. **5**(5): p. 3614-3621.

127. Lokteva, I., et al., Surface Treatment of CdSe Nanoparticles for Application in Hybrid Solar Cells: The Effect of Multiple Ligand Exchange with Pyridine. The Journal of Physical Chemistry C, 2010. **114**(29): p. 12784-12791.

128. Dorokhin, D., et al., Photoluminescence Quenching of CdSe/ZnS Quantum Dots by Molecular Ferrocene and Ferrocenyl Thiol Ligands. Journal of Physical Chemistry C, 2009. **113**(43): p. 18676-18680.

129. Schreuder, M.A., et al., Control of Surface State Emission via Phosphonic Acid Modulation in Ultrasmall CdSe Nanocrystals: The Role of Ligand Electronegativity. Journal of Physical Chemistry C, 2009. **113**(19): p. 8169-8176.

130. Kim, Y., et al., Ligand-dependent blinking of zinc-blende CdSe/ZnS core/shell nanocrystals. Physical Chemistry Chemical Physics, 2009. **11**(18): p. 3497-3502.

131. Lange, H., et al., Experimental investigation of exciton-LO-phonon couplings in CdSe/ZnS core/shell nanorods. Physical Review B, 2008. **77**(19).

132. Baker, D.R. and P.V. Kamat, Tuning the Emission of CdSe Quantum Dots by Controlled Trap Enhancement. Langmuir, 2010. **26**(13): p. 11272-11276.

133. Liu, I.S., et al., Enhancing photoluminescence quenching and photoelectric properties of CdSe quantum dots with hole accepting ligands. Journal of Materials Chemistry, 2008. **18**(6): p. 675-682.

134. Hutchins, B.M., A.H. Latham, and M.E. Williams, Chemically functional semiconductor nanocrystals: Electrochemistry and self-assembly on surfaces. Quantum Confined Semiconductor Nanostructures, 2003. **737**: p. 169-174.

135. Schreuder, M.A., et al., Control of Surface State Emission via Phosphonic Acid Modulation in Ultrasmall CdSe Nanocrystals: The Role of Ligand Electronegativity. The Journal of Physical Chemistry C, 2009. **113**(19): p. 8169-8176.

136. Munro, A.M., et al., Quantitative study of the effects of surface ligand concentration on CdSe nanocrystal photoluminescence. Journal of Physical Chemistry C, 2007. **111**(17): p. 6220-6227.

137. Wang, M.F., et al., Colloidal CdSe nanocrystals passivated by a dye-labeled multidentate polymer: Quantitative analysis by size-exclusion chromatography. Angewandte Chemie-International Edition, 2006. **45**(14): p. 2221-2224.

138. Guo, J., W.L. Yang, and C.C. Wang, Systematic study of the photoluminescence dependence of thiol-capped CdTe nanocrystals on the reaction conditions. Journal of Physical Chemistry B, 2005. **109**(37): p. 17467-17473.

139. Kalyuzhny, G. and R.W. Murray, Ligand effects on optical properties of CdSe nanocrystals. Journal of Physical Chemistry B, 2005. **109**(15): p. 7012-7021.

140. Comparelli, R., et al., Improved optical properties of US quantum dots by ligand exchange. Materials Science & Engineering C-Biomimetic and Supramolecular Systems, 2003. **23**(6-8): p. 1083-1086.

141. Hyeon-Deuk, K. and O.V. Prezhdo, Photoexcited electron and hole dynamics in semiconductor quantum dots: phonon-induced relaxation, dephasing, multiple exciton generation and recombination. Journal of Physics-Condensed Matter, 2012. **24**(36).

142. Li, S., M.L. Steigerwald, and L.E. Brus, Surface States in the Photoionization of High-Quality CdSe Core/Shell Nanocrystals. Acs Nano, 2009. **3**(5): p. 1267-1273.

143. Liu, X.F., et al., Preparation of Stable, Water-Soluble, Highly Luminescence Quantum Dots with Small Hydrodynamic Sizes. Journal of Nanoscience and Nanotechnology, 2011. **11**(3): p. 1941-1949.

144. Zhai, C.X., et al., One-Pot Synthesis of Biocompatible CdSe/CdS Quantum Dots and Their Applications as Fluorescent Biological Labels. Nanoscale Research Letters, 2011. **6**.

145. Wang, M.F., et al., Water-soluble CdSe quantum dots passivated by a multidentate diblock copolymer. Macromolecules, 2007. **40**(17): p. 6377-6384.

146. Wang, M.F., et al., Surface modification of CdSe and CdSe/ZnS semiconductor nanocrystals with Poly(N,N-dimethylaminoethyl methacrylate). Macromolecules, 2006. **39**(10): p. 3664-3672.

147. Pal, B.N., et al., 'Giant' CdSe/CdS Core/Shell Nanocrystal Quantum Dots As Efficient Electroluminescent Materials: Strong Influence of Shell Thickness on Light-Emitting Diode Performance. Nano Letters, 2012. **12**(1): p. 331-336.

148. Chen, L.L., et al., Shape and Temperature Dependence of Hot Carrier Relaxation Dynamics in Spherical and Elongated CdSe Quantum Dots. Physical Chemistry of Interfaces and Nanomaterials Ix, 2010. **7758**.

149. Bao, H., et al., Temperature Dependence of Hot Carrier Relaxation in a Pbse Quantum Dot: An Ab Initio Study. Ht2009: Proceedings of the Asme Summer Heat Transfer Conference 2009, Vol 1, 2009: p. 129-136.

150. Kamisaka, H., et al., Ab initio study of temperature- and pressure dependence of energy and phonon-induced dephasing of electronic excitations in CdSe and PbSe quantum dots. Journal of Physical Chemistry C, 2008. **112**(21): p. 7800-7808.

151. Crooker, S.A., et al., Multiple temperature regimes of radiative decay in CdSe nanocrystal quantum dots: Intrinsic limits to the dark-exciton lifetime. Applied Physics Letters, 2003. **82**(17): p. 2793-2795.

152. Tyagi, P., et al. Quantized Extrinsic Piezoelectricity in Quantum Dots Revealed by Coherent Acoustic Phonons. in International Conference on Ultrafast Phenomena. 2010. Optical Society of America.

Page Intentionally Left Blank

Page Intentionally Left Blank

Section 2: Experimental Results

Chapter 3 – Nanocrystals: A Platform for Optical Signal Processing

Chapter 4 – The Surface: Multiexcitonic Carrier Trapping

Chapter 5 – Two-Dimensional Electronic Spectrometer

Chapter 6 – Concluding Remarks and Future Works.

3 Nanocrystals: A Platform for Optical Signal Processing

This chapter is in part a reproduction of a peer-reviewed and published article:

Saari J.I., Krause M. M., Walsh B.R., Kambhampati P. "**Terahertz Bandwidth All-Optical Modulation and Logic Using Multiexcitons in Semiconductor Nanocrystals".** *Nano Letters.* 722–727. DOI: 10.1021/nl3044053. Publication Date (Web): January 22, 2013.

Contributions by J.I. Saari represents the bulk of the technological and theoretical development of the manuscript. B.R. Walsh and M.M. Krauss provided assistance throughout experimentation. P. Kambhampati assisted in editing the manuscript and was the principle investigator.

The manuscript represents a novel scientific contribution by the first author and has been expanded for this dissertation by J.I. Saari.

All required wavers and permissions are attached as appendices at the end of the dissertation.

3.1 Introduction

An increasing demand on existing communication infrastructure drives movement towards all-optical signal processing.[1] The unique size-dependent electronic structure, rich materials variability, and good chemical processability of semiconductor nanocrystals (NC) have demonstrated their promise and impact in a variety of optoelectronic applications spanning photovoltaics [2, 3], lasers [4, 5], photodetectors [6], and for LEDs.[7] Many of these same characteristics suggest their promise as a new enabling platform for all-optical modulators, switches, and ultimately a step towards optical logic gates. In contrast to their enormous impact upon a wide variety of applications, semiconductor nanocrystals have yet to demonstrate their impact upon the realization of novel platforms for all-optical switching and logic.

Owing to strong carrier confinement, as described in the previous section, NC have a unique electronic structure which arises from excitons.[8-12] This electronic structure has several characteristics that are advantageous for optoelectronic applications. Their transitions are tunable from the visible to the technologically relevant mid-infrared both by particle size as well as composition.[12] These transitions are moreover intense and narrow, thereby facilitating efficient optical pumping.[4, 5, 13, 14] A key characteristic of these NC is the degeneracies of the lower excitonic state. These NC can absorb multiple photons thereby creating multi-excitons (MX) by state filling of the excitonic levels.[8, 15]

Multiexcitons in NC have been well investigated due to their role in nanocrystal lasing.[4, 5, 8, 10, 13, 14] The key point towards nanocrystal lasing is that a minimal model of optical gain suggests it proceeds via stimulated emission (SE) from biexcitons (XX).[5, 8, 13, 14] It has been shown that populating higher MX results in a qualitatively unique effect of gain control.[8, 13, 14] Specifically, higher MX recombine at new wavelengths [8-10, 16-18] thereby resulting in the capacity to control the optical gain spectrum by prescribing specific MX states.[8, 13, 14]

In existing applications which utilize MX in NC such as lasing and photovoltaics, the main constraint is the short lifetime of these states. Pioneering work by Klimov and Bawendi first showed that the multiexciton recombination (MER) rates were ultrafast, size dependent, and quantized based upon the MX multiplicity.[15] For typical NC sizes and compositions, one finds τ_{XX} ~ 50 ps, τ_{XXX} ~ 20 ps, τ_{4X} ~ 5 ps. This situation poses a problem in that the optical gain lifetime is now too short as to be useful.

This section will demonstrate that by modulating the multiplicity of multiexcitons using femtosecond laser pulse sequences, semiconductor nanocrystals may be used as a material platform for optical switching, enabled by the physics of confinement induced multiexcitonic interactions. These experiments reveal that two key aspects of multiexcitons in nanocrystals facilitate these operations: fast recombination rates and large interaction strengths due to strong quantum confinement effects.

3.2 Experimental Details

The state-resolved pump/probe experimental technique was used as described in previous chapters. Pump pulses were derived from two optical parametric amplifiers (OPA) or the second harmonic of a Ti:sapphire chirped pulse amplification system (2.5 mJ, 1 kHz, 70 fs, 800 nm; Coherent). OPA derived pulse durations were determined via autocorrelation in a 30 μm BBO and maintained to roughly 40-50 fs for all wavelengths used via prism compression. Pump beam-waists were kept to 300-400 μm through-out experiments.

Multi-pulse sequences were achieved via beam splitters placed after pump delay stages. Readout was performed via single filament white-light continuum, generated in a 2 mm sapphire plate, and a scanning monochromater (Horiba Jobin-Yvon) as described in detail in the previous chapters. The chirp across the continuum was determined via cross-correlation with 800nm fundamental in a 100 μm BBO at the sample area. During readout, the continuum chirp was compensated for by appropriately delaying pump arrival for a given wavelength using the ‘chirp-free’ technique described previously. Pump delays for the respective pump lines were achieved with computer controlled delay stages with 0.1 μm precision (Newport PM500). Optical density was determined *in situ* via absorption of the un-pumped sample by white-light continuum as read by the scanning monochrometer. The resultant spectrum was compared against the linear absorption spectrum acquired from a Varian Cary 300 UV-Vis spectrophotometer.

Samples were diluted to an OD_0 of between 0.1 and 0.2. Both *in situ* and external steady-state spectra were acquired before and after experiment to ensure the absence of a photoproduct. The samples had no apparent deep trap emission and emission line widths were characteristic of an ensemble dispersity of $\sigma < 10$ %. The photoluminescence (PL) spectra were acquired via a Spex Fluromax-2 spectrofluorometer. (Δ)ΔOD measurements were made by appropriately chopping pump pulses at 500Hz or 333Hz, as described previously. The sample was circulated via peristaltic pump through a 1mm thick quartz flow-cell (Starna Cells).

3.3 Results and Discussion

In order to achieve all optical modulation, two energetically and temporally separated pump pulses: a *saturator* pulse to initialize the system for stimulated emission from biexcitons [8, 13, 14] and a *modulator* pulse which creates the signal from higher multiexcitons [8, 13, 14, 16] to be subsequently read out, as shown in Figure 3.1a were employed. Tuning the saturator resonant to the band-edge exciton (X_1) yields a nominally 1S-type exciton, whereas the modulator pulse pumps X_4, yielding a nominally 1P type exciton,[23] as seen in Figure 3.1b.

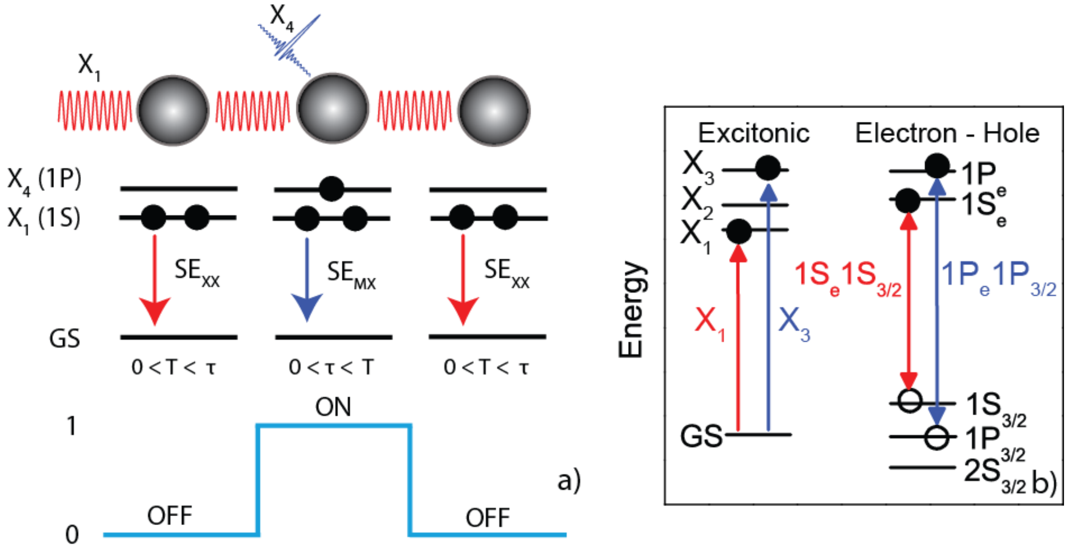

Figure 3.1 – (a) Schematic illustration of modulated stimulated emission via multiexcitons in semiconductor nanocrystals. (b) The level structure of excitons in NC in the exciton and the electron/hole representation.

The CdSe/ZnS linear absorption spectrum (OD_0), photoluminescence (PL), relevant excitonic states and corresponding pump spectra are shown in Figure 3.2a. The stimulated emission (SE) spectra, upon pumping into X_1 and X_4 with high fluence, are shown in Figure 3.2b. The SE spectra correspond to the negative portion of the nonlinear absorption spectra:

$$OD_{NL} = OD_0 + \Delta OD \tag{3.1}$$

The SE spectra here were obtained at a time delay of 2 ps, with fluences ~ $5\text{x}10^{14}$ photons/cm^2. The broadening and redshifting of the SE spectra with hot exciton (X_4) pumping is consistent with prior works.[8, 13, 14] It has previously been shown that this effect arises from the interaction of multiexcitons, [8, 13, 14, 16] and forms the basis of the switching approach used here. Specifically, higher multiexcitons emit at different wavelengths. Hence modulating the multiplicity of the multiexciton should result in modulation of the SE signal at these red-most wavelengths.

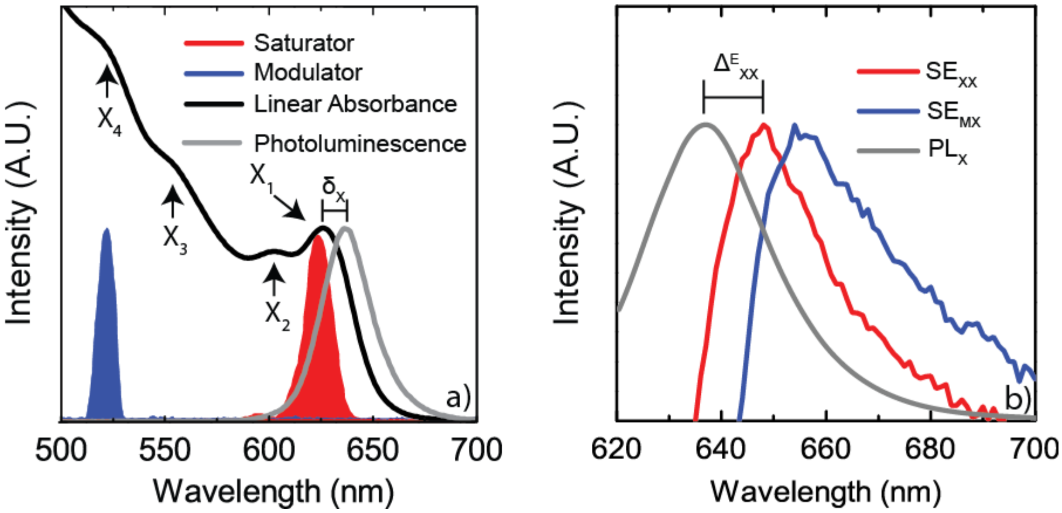

Figure 3.2 - (a) Linear absorption and photoluminescence (PL) spectra of CdSe/ZnS NC, R = 2.8 nm. Shown are the excitonic transitions and the exciton Stokes shift, δ_X. (b) PL and stimulated emission (SE) spectra. The PL arises from excitons (X), whereas the SE upon pumping into X_1 (S-Type) arises from biexcitons (XX) and the SE from X_4 (P-type) pumping arises from higher multiexcitons (MX). Indicated is the biexciton binding energy for emissive transitions, Δ_{XX}^E. The SE spectra were obtained at t = 2 ps.

The modulation scheme used, along with timing scheme definitions, can be seen in Figure 3.3a. The time between saturator and modulator pulses, **τ**, has a positive value if the saturation pulse arrives at the sample before the modulator pulse. The time between the saturator and the readout (or probe pulse), **T**, is positive when the saturator arrives at the sample prior to the probe. The idea behind the pulse sequences being that the saturator pulse creates a biexciton (XX) thereby saturating the band edge. The modulator adds population by pumping into the unfilled X_4 state. Hence the modulator creates MX of higher multiplicity. The two time orderings are such that the OFF state, or the purely XX state, is created when only the saturating pulse arrives prior to readout ($\tau > T$). The ON state, or MX state, is defined by both the saturator and modulator pulses arriving prior to readout in succession ($\tau < T$).

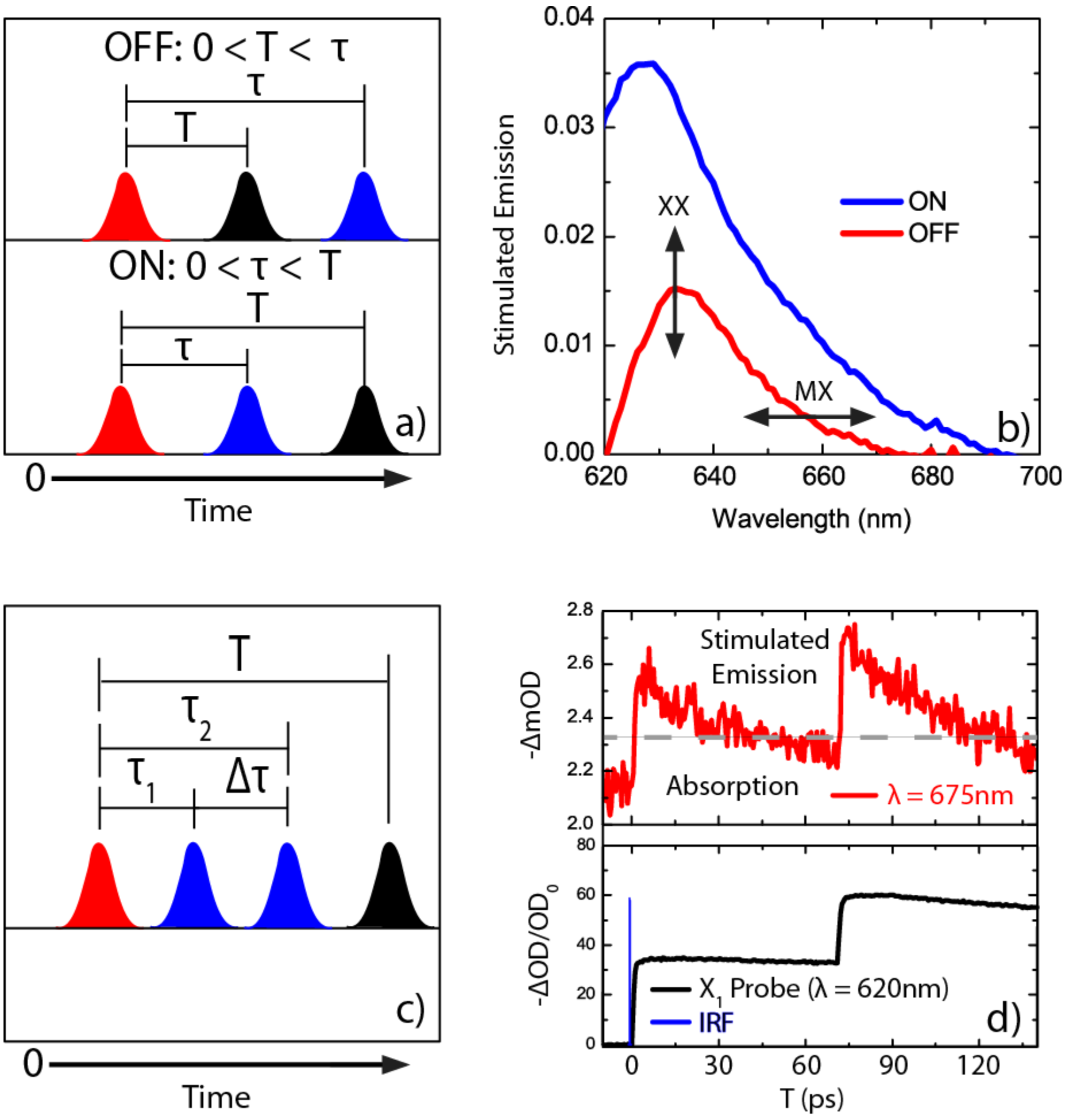

Figure 3.3 - (a) Pumping scheme for optical modulation using saturator (X_1 pump), modulator (X_4 pump), and readout (probe) pulses depicted in red, blue, and black, respectively. (b) SE spectra in ON/OFF pulse sequences. (c) A modulation scheme illustrating two ON bits. (d) Experimental realization of two ON bits at a 13 GHz modulation frequency. SE transient (red trace, λ_{probe} = 675 nm) showing 75ps peak-to-peak separation for ~13 GHz modulation rate. Modulator arrival times were verified *in situ* by monitoring the band edge bleaching of the X_1 transition (black trace, λ_{probe}= 620 nm).

With this time ordering, the modulation signal as well as its contrast was obtained. Figure 3.3b reveals that these pulse sequences produce SE signals which are consistent with XX or higher MX created by a single pulse. The SE from the OFF pulse sequence is identical to the SE_{XX} from a single high fluence X_1 pump. The SE from the ON pulse sequence is nearly identical to the SE_{MX}

from a single high fluence X_4 pump along with a contribution from the saturator pulse. The difference between the ON and OFF states enables amplitude modulation of the SE signal as illustrated by the amplitude at 630 nm. Here, the SE_{XX} is being modulated with poor contrast. Due to gain bandwidth control from higher multiexcitons, [8, 13, 14] the modulation effect is most pronounced at the red edge of the SE spectra. Near 670 nm, the modulation contrast ratio is greatly improved.

In order to directly determine modulation rates and depths, the readout is spectrally tuned to a wavelength with high contrast between ON and OFF (λ = 675nm), while a double modulator sequence is applied, Figure 3.3c. Figure 3.3d shows experimental realization of this modulation scheme. The arrival time of the X_4 modulator pulses is measured *in situ* by probing the band edge exciton bleaching signal (B_1). This B_1 signal, discussed in detail in the previous chapters and elsewhere [8, 9, 20, 24], has some amplitude of instrument response limited rise time [20, 24] thereby providing *in situ* timing of the modulator pulses. The X_1 30% fractional bleach ($\Delta OD/OD_0$) per modulator pulse is proportional to the number of carriers excited by the modulator pump and is consistent with <N>/pulse ~ 0.6. The modulated signal is read out at 675 nm due to minimal overlapping signal from SE_{XX}, Figure. 3d. From these data it is clear that the ON state is synchronized with the modulator pump. With this double pumping scheme of modulators separated by 75 ps, modulation rates of 13 GHz bandwidth at a modulation depth of > 20 dB were achieved.

By modulating an intermediary pulse, the resultant stimulated emission from multiexcitons can form a switching signal. In this case, the switch corresponds to the multiexciton multiplicity of the NC. In order to evaluate if this switching phenomenon can form a Boolean logic gate, the dual binary input states are correlated with the single SE output, Figure 3.4.

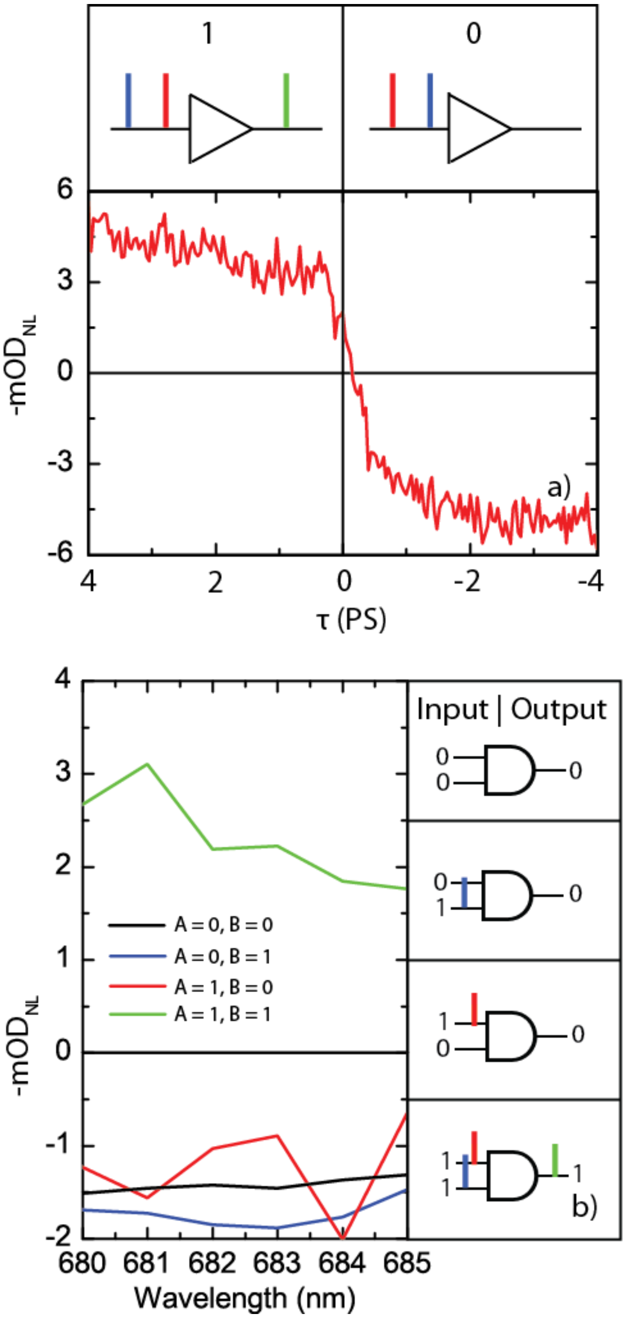

Figure 3.4 . (a) The modulator arrival time is swept from τ = 4 ps to -4 ps to determine pump-ordering dependence corresponding to an ON-OFF bit pattern, with T = 6 ps. The switching transient shows an ON-OFF (stimulated emission/absorption) response due to time encoding of the pulses in an inverter scheme. (b) Logic table and output of all-optical AND gate. Inputs were fixed to T = 3 ps, τ = 1 ps and altered via optical chopping. Stimulated emission, denoted by –mOD$_{NL}$ > 0, occurred only in the event of both optical inputs.

Shown is a bit pattern with the inputs corresponding to X_1 and X_4 pumps, and an output of SE$_{MX}$, Figure. 3.4a. The SE$_{MX}$ wavelength was chosen for the point of high contrast at 675 nm. By sweeping the modulator pulse from τ = 4ps to -4ps with the saturator pulse at T = 6ps, an inverter switch via time encoding, analogous to voltage encoding in electronic inverters, is demonstrated. Notably, this inverter switch responds on a sub-ps timescale due to the relaxation time of hot excitons in NC.[8, 9, 20, 24] The sharp response time produces insensitivity to timing jitter of the input signals.

To demonstrate Boolean logic, the dual inputs were optically chopped according to the logic table depicted in Figure 3.4b. Stimulated emission is denoted by a positive value for $-\mathrm{mOD}_{NL}$. These spectra reveal that any single input, be it saturator or modulator, yields a 0 (OFF) output. Only the presence of dual inputs yields a 1 (ON) output, thereby showing realization of an all-optical AND gate.

The switch itself acts as an amplitude modulator by virtue of modulating the amplitude of the SE at some readout wavelength as shown in Figure 3.5. With the presence of multiple excitonic states there exists the possibility of additional channels in a wavelength division multiplexing scheme. Figure 3.5a shows the SE signal as a function of the amplitude of the modulator pulse. The normalized SE spectra reveal the presence of additional SE bandwidth at the red that may be used to generate additional modulation channels.

Amplitude modulation of SE_{XX} at 635 nm shows a sub-linear fluence dependence (inset) due to saturation of X_1 with N = 2. The linear fluence dependence for SE_{MX} amplitude at 675 nm is consistent with a primarily SE_{XXX} signal: increasing modulator fluence increases XXX population without saturating. From these saturation curves, one finds that higher pulse energies enable faster modulation speeds and higher contrast.

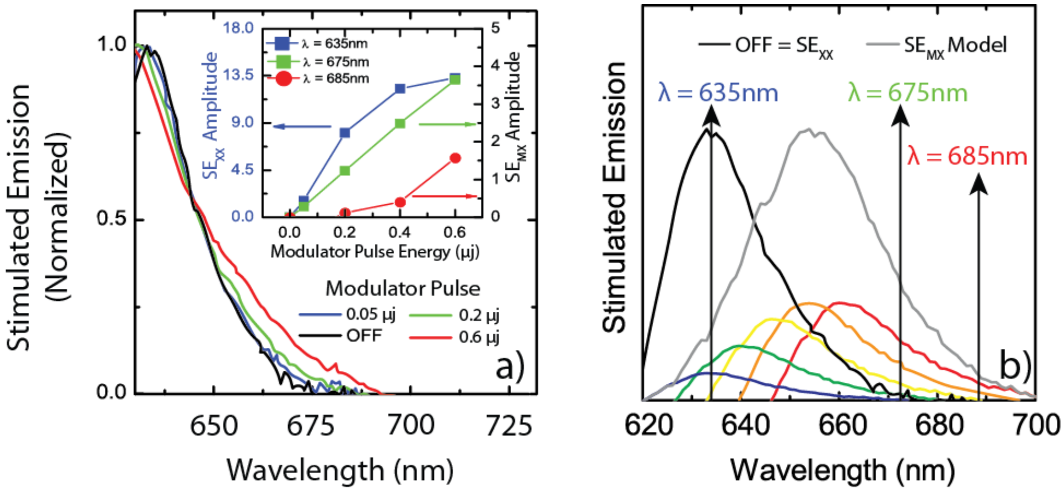

Figure 3.5 - (a) Fluence dependence of SE modulation amplitude with τ = 2 ps and T = 4 ps. The inset shows the wavelength dependence, revealing increasing nonlinearity due to higher multiexcitons. (b) The modulation channels as well as the contrast ratios are dictated by the MX spectra. The saturator produces SE_{XX} (OFF) whereas the modulator produces a Poisson distribution of MX which sums to SE_{MX}.

The contrast of the switch arises from the overlap of the multiexcitonic signals as shown in Figure 3.5b. In an effort to elucidate the contributions to the ON signal, a simple model for SE_{MX}, as described elsewhere [16], was used. The SE_{XX} derived from X_1 population inversion can only be due to biexcitons as the X_1 transition is doubly degenerate [8, 14] and is used as a carrier signal. To model the higher excitonic contributions in SE_{MX}, the SE_{XX} was shifted by the excitonic binding energy of 30 meV, as measured through the A1 feature in a transient absorption spectrum. The amplitude of the lineshape for each subsequent excitonic contribution was scaled to the probability as dictated by a Poisson distribution for a given <N>:

$$P_N = \langle N\rangle^N \frac{e^{-\langle N\rangle}}{N!} \tag{3.2}$$

for <N> from 1-6. The scaled and shifted lineshapes were then summed to represent the SE_{MX}. The modeled SE_{MX} for an <N> of 2, 4, and 6 are depicted in Figure 3.6 a, b, and c respectively. The spectral shift caused by increasing excitonic multiplicity becomes evident when modeled SE_{MX} spectra are compared as in figure 3.6d. Increasing X_4 pump fluence not only increases modulation rates but also enables fluence dependent multiplexing schemes.

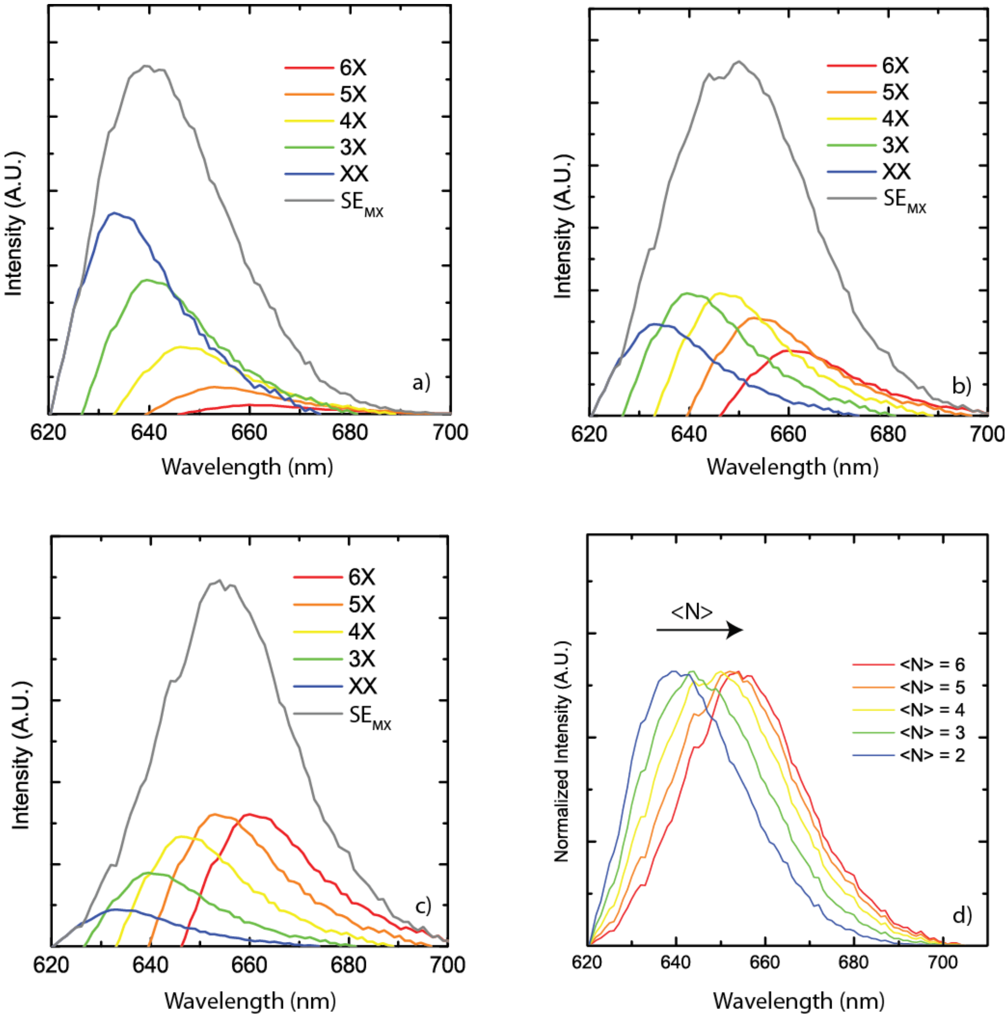

Figure 3.6 - (a) (b) (c) SE_{MX} model for <N> = 2, 4, and 6 respectively. (d) Comparison of lineshape for SE_{MX} model with increasing <N> showing redshift as expected.

To summarize, the Poisson distribution of higher MX prepared by the modulator pulse creates the signal on top of the background from the SE_{XX} created by the saturator pulse. This decomposition of SE into contributions from specific multiexcitons rationalizes the contrast ratio of the switch. Due to spectral overlap between MX states [16], contrast is diminished. This contrast can be improved by increasing MX interaction strengths or decreasing the SE linewidths.

However, the signal will also have contributions from decreased self-absorption as well as increased multiplicity. In order to define the true on and off states, the interplay between increased sample saturation and increased excitonic multiplicity with X_4 fluence was investigated, as shown in Figure 3.7.

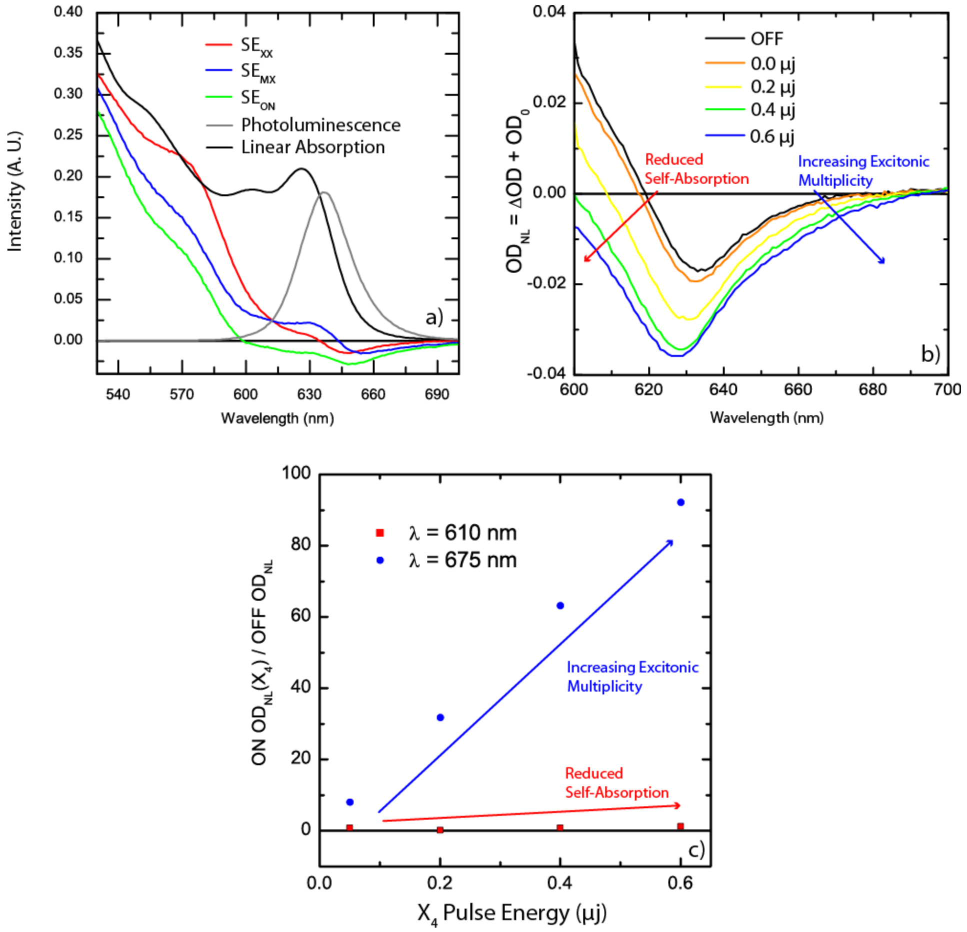

Figure 3.7 - (a) SE$_{XX}$ and SE$_{MX}$ as acquired by sole pumping of X_1 or X_4 respectively at 2 μj. Simultaneous pumping removes all self-absorption and leads to a broad SE which nearly perfectly recreates the PL. (b) Increasing X4 fluence opens up new multiexcitonic multiplicity which represent the true ON/OFF states for the all optical AND gate. (c) Contrast comparison between contributions to ON signal.

The red-shift of the spectrum is directly linked to increased excitonic multiplicity [13] and is therefore the signal of interest, whereas the increase intensity to the blue is due to decreased self-absorption. A comparison of the respective contrast with increased fluence for both self-absorption and increased multiplicity is shown in Figure 3.7c. Two respective wavelengths, λ = 675 nm and λ = 610 nm, were chosen. The stark increase in contrast with fluence for the λ = 675 nm trace compared to the λ = 610 nm trace is in agreement with increasing excitonic multiplicity.

The modulation bandwidth is dictated by MX recombination rates which correspond to the ON and OFF states. To directly determine these rates, The SE curves for R = 2.8 nm CdSe/ZnS and R = 1.3 nm CdSe/ZnS were taken, as shown in Figure 3.8a. At longer wavelengths, the SE curves decay faster. This response is anticipated from knowledge of the quantized Auger recombination rates of multiexcitons in these nanocrystals.[15] Probing at 635 nm demonstrates SE decay in agreement with the XX lifetime and the SE at 685 nm decays more rapidly, consistent with higher MX multiplicity. The noteworthy point is that the 675 nm SE transient is perfectly reproduced as a sum of 635 nm and 685 nm

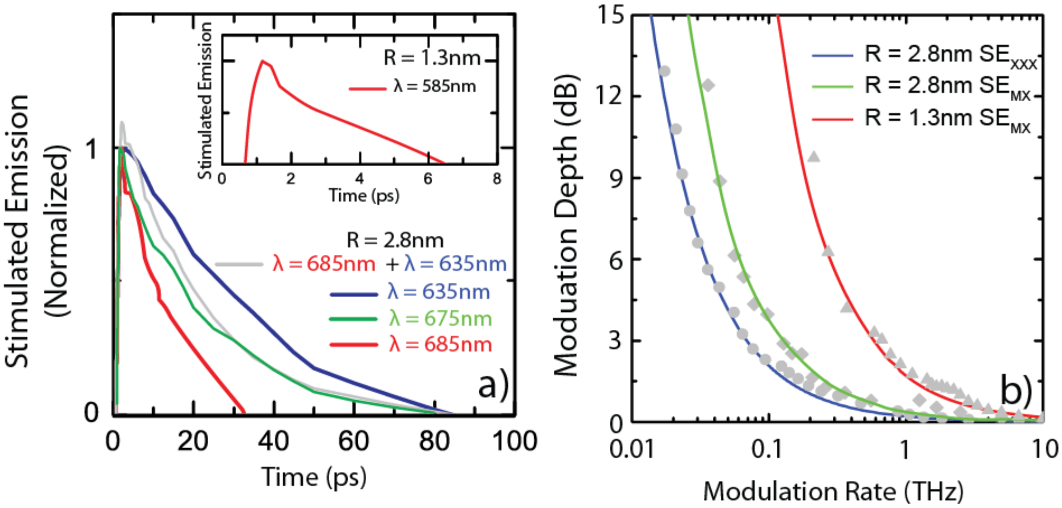

Figure 3.8 - (a) The modulation rate is dictated by the MX recombination rates. The transient at 635 nm corresponds to XX state, whereas the transient at 685 nm corresponds to higher MX. The intermediate 675 nm transient is well described as a sum of XX and MX transients due to spectral overlap. The inset shows a faster response for smaller NC (R = 1.3 nm). (b) Modulation spectra can be controlled by both NC size and MX multiplicity. The colored curves correspond to a simulation, and the grey points correspond to contrast ratios obtained from the experimental SE transients.

transients, corresponding to the signal arising as a sum of XX and higher MX contributions, as shown in 3.5b. As expected, the smaller nanocrystal has a faster recovery time, enabling higher modulation bandwidths.

The switching mechanism was analyzed by modeling as well as directly from the data, Figure 3.8b. The modulation spectrum is dictated by the lifetimes of the multiexcitonic states[15] and also the spectral overlap between the SE signals from the XX and MX states.[14, 16] Based upon published recombination rates and the MX spectral decomposition above, one may simulate the switching spectrum:

$$ON(T) = \sum_{N=2}^{6} P_N \, e^{-T/\tau_{NX}} \tag{3.3}$$

To recreate the experimentally observed transients and extract modulation rates, a two simulated transients were swept with increasing Δτ. Modulation rate and depth were then calculated as a function of Δτ:

$$Depth(dB) = 10\log_{10}\left(A/_{B}\right) \tag{3.4a}$$

$$Rate\ (THz) = \frac{1}{\Delta\tau} \tag{3.4b}$$

In addition, the SE data was directly analyzed to extract the time dependent contrast ratios which determine the switch spectrum. Both are shown in Figure 3.8b with near perfect agreement. This analysis shows that higher multiexcitons enable faster switching as does smaller nanocrystals. Notably, the 3 dB modulation bandwidths can approach 1 THz.

3.5 Conclusion

In summary, multiexcitons in semiconductor nanocrystals can form the basis of ultrafast all optical switching at THz rates. Based upon dual inputs and time ordering, this approach has enabled realization of Boolean logic with an AND gate as well as signal inversion. The mechanism driving the modulation rate is multiexcitonic (Auger) recombination. This room temperature AND gating is made possible by the large interaction energies unique to these NC. This work reveals a completely new mechanism by which optical signals may be modulated, as well as a new area of impact for semiconductor nanocrystals.

3.6 References

1. Miller, D.A.B., Are optical transistors the logical next step? Nat Photon, 2010. **4**(1): p. 3-5.
2. Gur, I., et al., Air-stable all-inorganic nanocrystal solar cells processed from solution. Science, 2005. **310**(5747): p. 462-5.
3. Huynh Wendy, U., J. Dittmer Janke, and A.P. Alivisatos, Hybrid nanorod-polymer solar cells. Science, 2002. **295**(5564): p. 2425-7.
4. Klimov, V.I., et al., Single-exciton optical gain in semiconductor nanocrystals. Nature, 2007. **447**(7143): p. 441-446.
5. Klimov, V.I., et al., Optical gain and stimulated emission in nanocrystal quantum dots. Science, 2000. **290**(5490): p. 314-317.
6. Konstantatos, G. and E.H. Sargent, Nanostructured materials for photon detection. Nat Nano, 2010. **5**(6): p. 391-400.
7. Coe, S., et al., Electroluminescence from single monolayers of nanocrystals in molecular organic devices. Nature, 2002. **420**(6917): p. 800-803.
8. Kambhampati, P., Unraveling the Structure and Dynamics of Excitons in Semiconductor Quantum Dots. Accounts of Chemical Research, 2011. **44**(1): p. 1-13.
9. Kambhampati, P., Hot Exciton Relaxation Dynamics in Semiconductor Quantum Dots: Radiationless Transitions on the Nanoscale. The Journal of Physical Chemistry C, 2011. **115**(45): p. 22089-22109.
10. Klimov, V.I., Spectral and dynamical properties of multilexcitons in semiconductor nanocrystals. Annual Review of Physical Chemistry, 2007. **58**: p. 635-673.

11. Efros, A.L. and M. Rosen, The electronic structure of semiconductor nanocrystals. Annual Review of Materials Science, 2000. **30**: p. 475-521.

12. Norris, D.J. and M.G. Bawendi, Measurement and assignment of the size-dependent optical spectrum in CdSe quantum dots. Physical Review B: Condensed Matter, 1996. **53**(24): p. 16338-16346.

13. Cooney, R.R., et al., Gain Control in Semiconductor Quantum Dots via State-Resolved Optical Pumping. Physical Review Letters, 2009. **102**(12): p. 127404.

14. Cooney, R.R., et al., State-Resolved Manipulations of Optical Gain in Semiconductor Quantum Dots: Size Universality, Gain Tailoring, and Surface Effects. Journal of Chemical Physics, 2009. **131**: p. 164706.

15. Klimov, V.I., et al., Quantization of multiparticle Auger rates in semiconductor quantum dots. Science, 2000. **287**(5455): p. 1011-1013.

16. Sewall, S.L., et al., State-resolved observation in real time of the structural dynamics of multiexcitons in semiconductor nanocrystals. Physical Review B, 2011. **84**(23): p. 235304.

17. Fisher, B., et al., Multiexciton fluorescence from semiconductor nanocrystals. Chemical Physics, 2005. **318**(1-2): p. 71-81.

18. Osovsky, R., et al., Continuous-Wave Pumping of Multiexciton Bands in the Photoluminescence Spectrum of a Single CdTe-CdSe Core-Shell Colloidal Quantum Dot. Physical Review Letters, 2009. **102**(19): p. 197401-4.

19. Sewall, S.L., et al., State-to-state exciton dynamics in semiconductor quantum dots. Physical Review B: Condensed Matter and Materials Physics, 2006. **74**(23): p. 235328.

20. Cooney, R.R., et al., Breaking the Phonon Bottleneck for Holes in Semiconductor Quantum Dots. Physical Review Letters, 2007. **98**(17): p. 177403.

21. Sewall, S.L., et al., State-resolved studies of biexcitons and surface trapping dynamics in semiconductor quantum dots. Journal of Chemical Physics, 2008. **129**(8): p. 084701.

22. Sewall, S.L., et al., Direct observation of the structure of band-edge biexcitons in colloidal semiconductor CdSe quantum dots. Physical Review B (Condensed Matter and Materials Physics), 2009. **80**(8): p. 081310(R).

23. Sewall, S.L., R.R. Cooney, and P. Kambhampati, Experimental tests of effective mass and atomistic approaches to quantum dot electronic structure: Ordering of electronic states. Applied Physics Letters, 2009. **94**(24): p. 243116-3.

24. Cooney, R.R., et al., Unified picture of electron and hole relaxation pathways in semiconductor quantum dots. Physical Review B (Condensed Matter and Materials Physics), 2007. **75**(24): p. 245311-14.

4 The Surface

This chapter is in part a reproduction of a peer-reviewed and published article:

Saari, J. I., Dias E.A., Reifsnyder D., Krause M.M., Walsh B. R., Murray C.B., and Kambhampati, P. “**Ultrafast Electron Trapping at the Surface of Semiconductor Nanocrystals: Excitonic and Biexcitonic Processes.**” *The Journal of Physical Chemistry: B*. DOI**:** 10.1021/jp307668g. Publication Date (Web): November 27, 2012. **Copyright © 2012 American Chemical Society**

Contribution by J.I. Saari represents the bulk of the technological and theoretical development of the manuscript. D. Reifsnyder and E.A. Dias provided samples. B.R. Walsh and M.M. Krauss provided assistance throughout experimentation. P. Kambhampati assisted in writing and editing the manuscript and was the principle investigator.

Synthetic details, as written in the manuscript, were provided by D. Reifsnyder and E.A. Dias.

The manuscript represents a novel scientific contribution by the first author and has been expanded for this dissertation by J.I. Saari.

All required wavers and permissions are attached as appendices at the end of the dissertation.

4.1 – Introduction

Semiconductor nanocrystals have been under intense investigation for their novel properties arising from quantum confinement.[1-9] Moreover these properties may be exploited for a variety of device applications ranging from light emitting diodes,[10, 11] optical gain and lasing,[12-17] and photovoltaics.[18] A commonly studied aspect of nanocrystal (NC) research is the structure and dynamics of quantized excitons whose behavior is dictated by the core of the NC. The excitonics of the core states of NC has been discussed in detail in recent reviews, as well as in previous chapters.[6-8] Specific aspects of the excitonics of NC include electronic structure, hot exciton relaxation, multiexciton recombination and generation, exciton-phonon coupling, photoluminescence and optical gain.

Despite progress in our understanding of the quantized core states of NC, there remains a poor understanding of one of their main characteristic features – their surface.

By virtue of their size, a large fraction of the atoms in a NC are at the surface. In particular, the overlap of the excitonic wavefunctions with the surface of the NC becomes larger as the particle becomes smaller as anticipated from a simple hard sphere calculation. This behavior is pronounced upon inclusion of tunneling.[19-21] Hence the surface of the NC is of clear importance by simple inspection of the size of the system. This situation is unique to the NC form of the QD as their epitaxial (self-organized) variants are typically buried within a host semiconductor thereby passivating the surface.[14]

While the surface of the NC is of clear structural importance, its understanding as well as exploitation in application has lagged behind relative to the advancements in the core of the NC. The surface of the NC is largely considered to be an unwanted part of the system, with properties to be mitigated rather than engineered for use.

For example, passivating the surface is a commonly used approach to improve the photoluminescence (PL) quantum yield.[22, 23] Similarly, trapping to the surface by hot excitons has been identified as a culprit in blocking optical gain in NC.[8, 15, 16, 24] In the multiple exciton generation (MEG) or carrier multiplication (CM) process, [25-33] this hot exciton surface trapping is now becoming seen as a culprit for inconsistency in measurements of the yield of this key process.[34-42] In the MEG literature, this surface trapping process is commonly referred to as photocharging. The surface of the NC is also appearing to be a culprit in the origin of blinking in single NC PL experiments.[43-46] Hence an understanding of the manner in which the core excitonic states are coupled to the surface of the NC is of clear importance to advancing our understanding and application of these processes.

An alternative view of the surface is that it represents an *opportunity* to engineer the functionality of the NC, rather than merely serve as a problem to be mitigated. For example, charge extraction and injection using adsorbed molecules should involve the surface. The most common such example is the dye sensitized NC solar cell.[47, 48] Charge extraction is a key process for photovoltaic (PV) applications, with recent experiments revealing the capacity to extract multiple excitons from NC via adsorbed electron acceptors.[49-57] Whether in PV or in photoconductive films, the surface of the NC should be a key factor. The surface is moreover of explicit importance for NC based sensing[58-61] and photocatalysis applications.[62-64] Finally, the surface of small NC is now being used as a path to generating white light emitting NC for LED applications.[65-72]

In light of the importance of surface trapping in NC, one aims for additional spectroscopic signals which may assist in providing a microscopic picture of the factors which control charge trapping at the surface. In this chapter, excitonic state-resolved pump/probe data on CdTe NC are presented. It is shown that surface alteration during aging CdTe NC can support very fast surface trapping rates. In particular, fast trapping rates for electrons in aged CdTe NC are demonstrated. Specifically, faster electron trapping for the single exciton than for fresh CdTe is observed. In these aged CdTe samples, biexcitons have enhanced surface trapping rates. The electron transfer trapping times from the ground biexcitonic state to the surface of the nanocrystal is sufficiently fast as to launch coherent acoustic phonons on the electronic ground state. These results illustrate that coherent phonons can serve as a reporter for interfacial charge transport,[73] in support of simpler decays from kinetic transients which can be ambiguous.[39] These results furthermore suggest that trapping rates may be distinct for higher multiexcitons, informing the design of acceptor systems for multiple exciton dissociation across the nanocrystal interface.[51, 54-57]

4.2 Experimental Details

4.2.1 Synthesis

For a typical reaction, A stock tributylphosphine tellurium (TDPTe) injection solution was prepared by dissolving 0.1 g of Tellurium shot (Te, Aldrich, shot 1-2 mm, 99.999%) in 2.35 mL tributylphosphine (TBP, Aldrich, 97%) at room temperature and then diluting with 7.6 mL 1-octadence (ODE, Sigma-Aldrich, 90% technical grade). In a 50-mL three-neck round-bottom reaction flask, 0.0384 g (0.3 mmol) cadmium oxide (CdO, Acros, 99%), 0.171 g (0.614 mmol) n-tetradecylphosphonic acid (TDPA, Strem, ≥97%), and 15.2 mL ODE were combined. Under nitrogen, the reaction flask was heated to 300 °C for 30 minutes, with a 21 gauge needle as an outlet through a septum. After 30 minutes, the heating mantle and outlet were removed, and 3 mL of the TBPTe stock was rapidly injected. The reaction flask was allowed to cool to room temperature with no additional heating. The samples were then dispersed in toluene after a period of roughly 72 hours. In order to elucidate the effect of the surface, this work focuses on CdTe NC with radii of ~ 1.5 nm. The size of the CdTe nanocrystals was determined empirically from the wavelength of the first absorption peak.[74] The aged samples were stored in powder form for a month in a standard chemical fridge at 4°C protected from light in an aluminium-foil wrapped closed glass vial under argon. The samples were redispersed in toluene when needed for experiment. The fresh samples were not redispersed, and were used immediately.

4.2.2 Spectroscopy

The experimental approach used here has been discussed in previous chapters, as well as earlier works. [15, 16, 19-21, 24, 39, 75-81] Linear absorption and photoluminescence spectra were acquired in-situ before, during, and after femtosecond experiments to ensure absence of photo-degradation. The NC were dispersed in spectral grade toluene and flown through a 1 mm path length quartz flow cell via peristaltic pumping.[80] The flow rate was set to minimize bubble formation and noise as well as ensure novel sample for each optical shot through observation of a steady stream (> 2 mL/Min) of solution at output. This ensured sufficient flow between shots at 1 kHz (1 ms). The optical density of the sample was between 100 and 200 mOD at the X_1 transition (band edge exciton).

The pump pulses were derived from optical parametric amplifiers. Pulse durations were determined via intensity autocorrelation in a 30 μm BBO and maintained at durations of between 30 and 40 fs throughout the experiment. Prism compressors were used to compensate for temporal chirp of the OPA derived pump pulses. Pump beam waists were 300 to 400 μm. Probe pulses were obtained via single-filament white light continuum generated in a 2 mm sapphire plate. A fused silica prism compressor was used to compensate for temporal chirp of the probe. The pump pulses were chopped at 333 Hz with appropriate phase shift to acquire transients with alternating pump wavelengths at a shot by shot level. [81] The chirp-free transient absorption spectra were acquired through a scanning monochrometer. [15, 16, 21, 76] The spectral chirp of the probe was determined via cross-correlation with the pump pulses in a 30um BBO crystal at the sample stage. The chirp was compensated for by simultaneously adjusting the relative pump-probe delay according to the calibrated chirp.

4.3 Results

Optical excitation of the NC creates a single exciton (X) at low excitation intensity and can create multiexcitons (MX) at high intensities.[5, 7, 8] The simplest MX is the biexciton (XX), which is the focus of this work. One aims to measure the rate at which electrons and/or holes experience trapping to the surface of the NC,[21, 39, 75, 82-85] and the factors that govern these rates. Figure 4.1 illustrates these processes. At low intensities, a single photon is absorbed which creates X, Figure 4.1a. Illustrated schematically is trapping of the

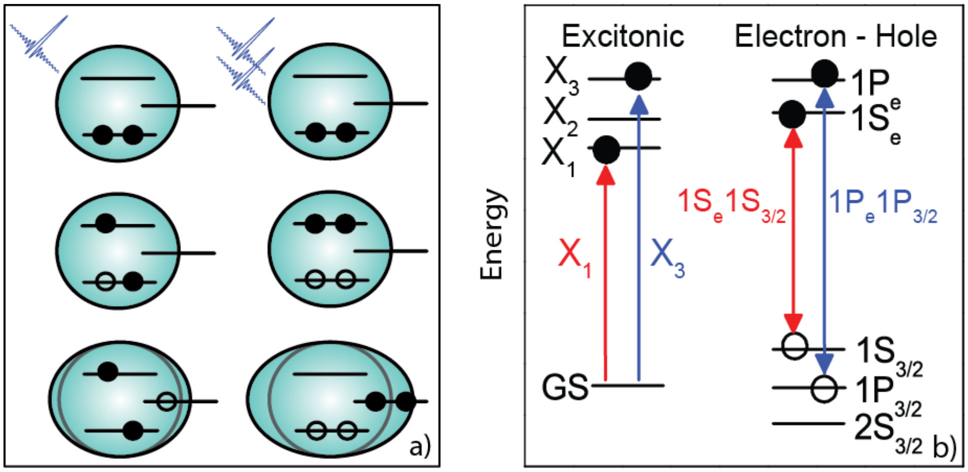

Figure 4.1 - Schematic illustration of relevant multiexcitonic surface trapping and optical pumping processes. (a) Weak excitation conditions result in creation of a single exciton (X) which can experience either electron or hole trapping at the surface of the nanocrystal. Stronger excitation conditions result in absorption of multiple photons from a pump pulse yielding creation of a multiexciton (MX). (b) The electronic structure of nanocrystals can be depicted in either the exciton or the electron/hole picture. In the excitonic picture, the lower states (e.g. X_1) are two-fold degenerate based upon the S-type symmetries of the electron/hole states. The higher states (e.g. X_3) can have higher degeneracies thereby supporting higher MX multiplicities.

hole to the surface state creating a state previously described as a surface trapped exciton. [21, 39, 75] The same process is alternatively referred to as photocharging in the PL blinking and MEG / CM literature. [35, 44, 45, 86-90]. At higher intensities, multiple photons may be absorbed[5-8, 15, 16, 21, 24, 39, 76, 81, 91-93] thereby creating an MX state such as the XX state illustrated here. In the XX schematic, the electrons undergo surface trapping to illustrate the possibility of either carrier becoming strongly coupled to the surface of the NC.

In order to focus specifically on the XX state, one can exploit the known electronic structure of these II-VI NC. [3, 5, 7, 77, 94, 95] Commonly, one pumps at 400 nm (3.1 eV) due to convenience. [4, 5] Excitation into the continuum, however, will create a Poisson distribution of MX thereby obfuscating an excitation dependent investigation. Recognizing the degeneracies of the excitonic states, one can spectroscopically prescribe specific MX states. Figure 4.1b shows a schematic electronic structure of these II-VI (common to CdS, CdSe, CdTe) NC in the electron/hole as well as the exciton representation using the multiband effective mass approach. [3, 94-96] The X_1 excitonic state can be described within the multiband effective mass approach as arising from a $1S_e$ - $1S_{3/2}$ electron-hole state and the X_3 state as a $1P_e$ -$1P_{3/2}$ electron-hole state. The key point is that the X_1 state is two-fold degenerate whereas the X_3 state is six-fold degenerate. Hence pumping directly into the X_1 state rather than the continuum enables creation of a MX population with a maximum multiplicity of $\langle N \rangle = 2$. Here, $\langle N \rangle$ refers to the mean exciton occupancy.

Prior work on CdSe revealed that a full pump/probe transient absorption (TA) spectrum can be unraveled to identify whether it is the electron or the hole that gets trapped at the surface. Briefly, the band edge bleach recovery (B1 signal) monitors the electron population in the band edge exciton due to state filling. Hence decay of the B1 signal reflect detrapping of electrons from the 1S band edge state to the surface of the NC. In contrast, the A1 signal to the red of the band edge bleach arises from absorption from X into XX and spectroscopically manifests itself as a photoinduced absorption (PA), as discussed in the previous section.

In the case of fresh CdSe with amine ligands, it has been previously shown that the hole rather than the electron undergoes surface trapping on the 10 – 100 ps timescale, [21] with slower rates for larger NC as anticipated by surface fraction arguments. In those experiments, the CdSe NC were pumped directly into the band edge exciton to focus on surface trapping dynamics without obfuscation from exciton cooling. The work subsequently demonstrated the effect of surface passivation on surface trapping in CdSe NC. [39] In those experiments, pumping into the excitonic continuum at 400 nm enabled evaluation of hot exciton surface trapping in competition with exciton cooling. Those experiments revealed that the degree of surface passivation dictates the rate of hot exciton surface trapping. In those CdSe experiments, the TA signals always revealed hole trapping to the surface.

CdTe NC are similar in electronic structure to CdSe NC, [96] but are less well studied.[97] This section aims to evaluate the trapping dynamics of CdTe NC as a function of sample aging. Figure 4.2 shows linear absorption spectra and photoluminescence (PL) spectra of the freshly synthesized as well as aged CdTe samples. Shown are representative spectra from different syntheses. The linear absorption spectra are similar to each other and to the well-known spectroscopy of CdSe NC as anticipated from theory.

The main difference is that the aged CdTe show very weak PL (~100x smaller than fresh CdTe) as expected from poor surface passivation due to trap states. However, it is not clear whether this aging process and passivation quality in general results in electron or hole trapping and the timescales and pathways for this charge transfer process. Hence one aims for a more clear picture of the carrier trapping processes that take place at the surface of the NC than is afforded by simple PL measurements.

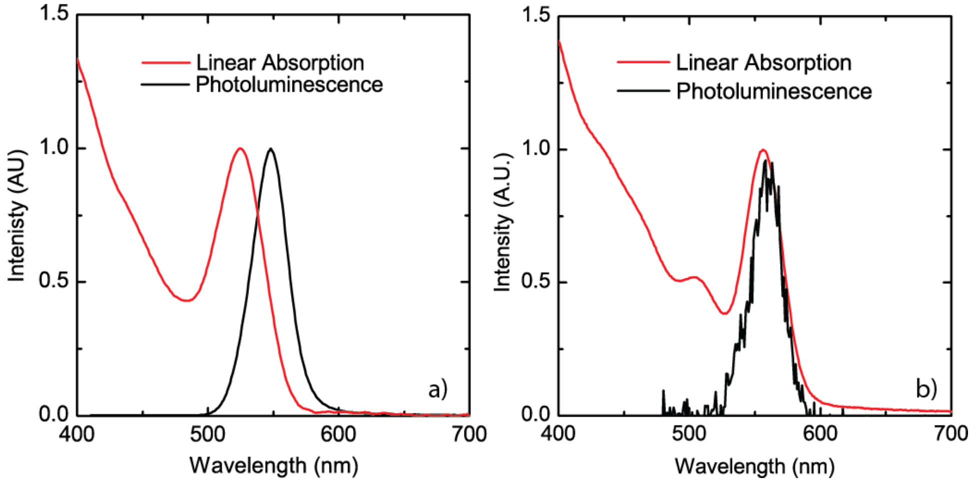

Figure 4.2- Linear absorption and spontaneous photoluminescence (PL) spectra of fresh (a) and aged (b) CdTe nanocrystals. Both samples show discrete transitions in the linear absorption spectra characteristic to confined excitons in nanocrystals. The PL from the aged CdTe has been increased by 100x for comparison.

4.3.1 Transient Absorption Spectra of Fresh and Aged CdTe

Figure 4.3 shows representative transient absorption (TA) spectra of fresh and aged CdTe NC with excitation into the X_3 state (1P exciton) with an excitation density of <N> = 0.5. The exact transition energies between the fresh and aged samples are not identical, as they were obtained from representative data sets across a synthetic runs. <N> refers to the mean number of absorbed photons and therefore the mean exciton occupancy. The fresh samples show TA signals qualitatively consistent with prior work on CdSe NC. [6-8, 15, 16, 19-21, 24, 39, 75-79, 81] There is a band edge bleach in the blue which slowly recovers. As well there is a narrowband photoinduced absorption (PA) immediately to the red of the band edge bleach. This narrowband PA arises from biexciton induced level shifting. [6-8, 21, 24, 76]

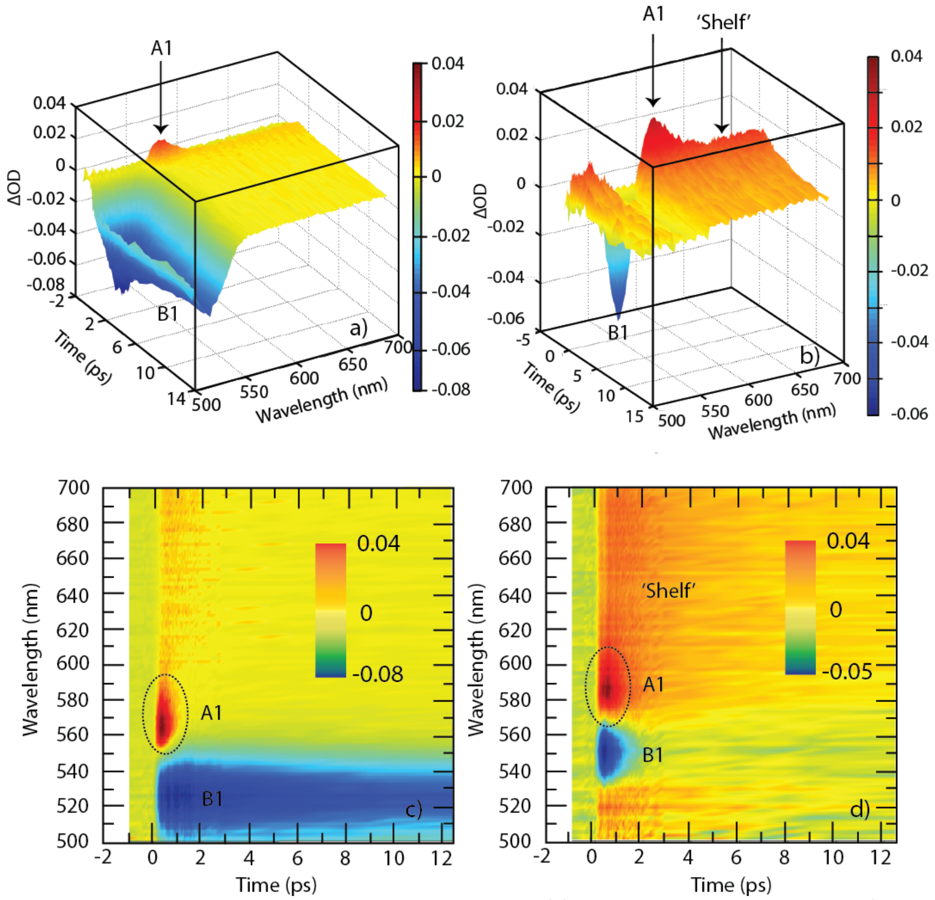

Figure 4.3 - Transient absorption (TA) spectra of fresh (a, b) and aged (c, d) CdTe nanocrystals shown as 3D surfaces (upper panels) and contour plots (lower panels).The pump pulse was tuned to the X_3 initial excitonic state with <N> = 0.5. The main features of note are the band edge bleach signal (B1) feature, the narrowband photoinduced absorption (A1) feature, and the broadband photoinduced absorption (PA). The aged sample shows faster decay of the B1 feature and larger amplitude of the broadband PA at the red of the TA spectrum.

The TA spectra for the aged CdTe NC are qualitatively different than of the fresh samples. In the case of the aged NC, the B1 bleach signal recovers on the 1-2 ps timescale, orders of magnitude faster than in the fresh samples and in CdSe. The narrowband A1 signal is considerably larger. Also, to the red of the A1 signal is a large broadband PA. This PA "shelf" feature has been seen by a variety of researchers[39, 91, 93, 98] and its origin remains unclear, however It has recently been assigned as arising from intraband absorption from the quantized excitonic states into the excitonic continuum.[39] These transitions should have a large energy spectrum due to the continuum of final states thereby manifesting themselves spectroscopically as a shelf-like feature. It was proposed that these transitions, not normally seen in TA spectra, become allowed by some surface trapping induced perturbation to the intraband selection rules, as hinted to in the introductory sections.

4.3.2 Electron Dynamics via Band Edge Bleach.

The band edge bleach recovery (B1 signal) has been well reported. [4-8, 19, 20, 39, 77, 81] This signal monitors the population of electrons in the 1S band edge exciton. It has been previously shown that excitation directly into X_1 yields an instrument response limited bleach by directly populating the 1S electron for the case of CdSe NC. [19, 20, 81] These results on CdTe show the same response, Figure 4.4a. Since the X_1 excitonic state has its electron already in the 1S state, there is no further relaxation that is possible within the quantized manifold of states. Hence any decay of this signal is due to electron depopulation whether via radiative recombination or electron transfer to trap states, typically assigned as the source of non-radiative recombination.

Well passivated CdSe NC show small amplitude decay of the B1 signal on the 30 ps timescale due to a small fraction of the NC undergoing surface trapping on this timescale. In contrast, the CdTe NC show faster decay and larger amplitude to the decay for both fresh and aged samples. The main observation in the B1 signal is a large amplitude to the B1 decay thereby revealing that the aging of the NC produces efficient electron traps at the surface of the NC. Figure 4.4b-c further focuses on the B1 signals on the aged CdTe to more closely inspect the electron dynamics as determined by aging. The results on fresh CdTe samples are consistent with prior work on CdSe[19-21, 81] and will not be further discussed here. Figure 4.4b shows the B1 signal as a function of initial excitonic state in the manner previously described in detail for CdSe NC using the excitonic state-resolved pump/probe approach. [6, 7, 19-21, 81] Comparison of the X_1 and X_2 pumping conditions reveals identical B1 signals as previously shown for CdSe. Hence both excitonic states share

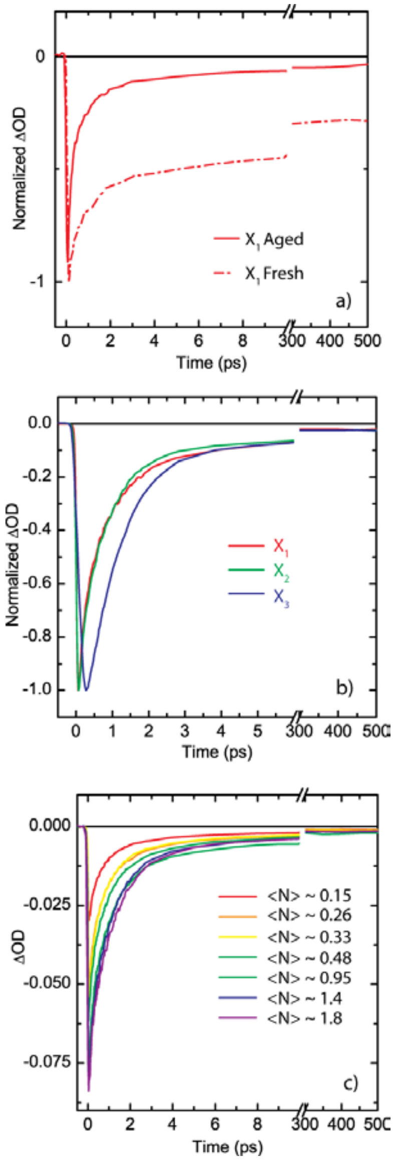

Figure 4.4 - Femtosecond pump/probe transients, probing at the band edge exciton (B1 feature). (a) Comparison of fresh and aged samples upon pumping into X_1 or X_3. In both samples, X_3 pumping delays the buildup of the B1 feature due to hot electron relaxation. For both pumping conditions, the aged samples show a faster B1 decay. This decay arises from electron rather than hole trapping (see text for details). (b) Initial excitonic state-dependence to the B1 bleach dynamics for the aged CdTe. X_1 and X_2 pumping show identical response, indicating a common electron state. X_3 pumping shows a buildup and slowed decay due to hot electron relaxation from 1P to 1S states. (c) Pump fluence dependence to B1 dynamics for the aged sample with X_1 pumping. <N> refers to the mean exciton occupancy. N_{max} = 2 due to the degeneracy of the X_1 state.

a common 1S electron state as predicted by theory. X_3 pumping shows a buildup time in a manner completely consistent with CdSe NC. These CdTe NC show a fast sub-ps buildup of the B1 signal due to fast electron relaxation from 1P to 1S states. Hence CdTe NC also shows a clear “breaking of the phonon bottleneck”, [2, 4] due to the presence of additional relaxation pathways. [6, 7, 19, 20, 81]

The additional relaxation pathways include Auger electron relaxation as well as ligand based (non-adiabatic) channels, as discussed in the introductory sections and elsewhere. [6, 7, 19, 20, 81] Based upon the excitonic state-resolved approach to evaluating electron/hole state-to-state transition rates, the 1P to 1S electron transition takes place in 200 fs for CdTe NC (aged as well as fresh). Finally, Figure 4.4c shows the fluence dependence to the decay of the B1 signal upon pumping directly into the two-fold degenerate X_1 excitonic state. At higher excitation the decay is more rapid, a point that will be discussed in detail below.

This similarity in these electron transition times between CdSe and CdTe NC is not necessarily obvious from inspection of the electronic structure of II-VI NC. [3, 96] Specifically, CdTe is known to have larger spin-orbit split off for the valence band (VB) thereby decreasing the VB density of states (DOS). It is the asymmetry in the conduction band (CB) and VB DOS that enables this unidirectional electron cooling process. Hence one might anticipate slower electron cooling for CdTe relative to CdSe NC. The similarity between the two NC suggest that the real atomistic electronic structure may still maintain a large VB DOS. Similar arguments were made by Zunger on co-workers in the case of PbSe NC. [99] In the case of PbSe, the situation is more striking in that the CB and VB are symmetric within the multiband effective mass approximation (EMA) [3, 96, 100-102] thereby blocking the Auger channel's requirement of larger VB DOS. In contrast, atomistic empirical pseudopotential methods[99] (EPM) revealed that PbSe NC have a larger VB DOS thereby maintaining their capacity for ultrafast Auger based electron to hole energy transfer.

4.3.3 Hole Dynamics and Biexciton Formation via Photoinduced Absorption Signals

Figure 4.5 shows the photoinduced absorption (PA) signals. These PA signals can be grouped in two: the now well understood narrowband PA arising from biexciton (XX) based level shifting, [5-8, 21, 24, 76, 103] and the poorly understood broadband PA "shelf" signal. TA spectra of the fresh and aged NC are shown in Figure 5a-b and kinetic transients in Figure 5c-f. The TA spectra show clear differences for both the A1 PA as well as the shelf PA. The A1 PA arises from biexciton formation and enables extraction of biexciton binding energies. Here, the binding energy for the ground state (band edge) biexciton is 35 meV for the aged samples, qualitatively consistent with prior works on CdSe NC.[6-8, 21, 24, 76]

The main difference is the broadband shelf PA that is noticeable for fresh CdTe NC and is pronounced on the aged samples. This broadband PA was observed in early CdSe experiments at high intensity pumping by El-Sayed and co-workers[93] and Alivisatos and co-workers[91] as well as in recent experiments by Weiss and co-workers. [98] It has been previously proposed that this signal arises from a surface trapping induced perturbation to the intraband selection rules which enables transitions from the quantized excitonic states into the continuum at high energy[39]. In fresh CdSe, the samples had to be degraded by illumination in order to produce the broadband PA due to surface trapping. In contrast, the fresh CdTe NC show this surface trapping signal readily.

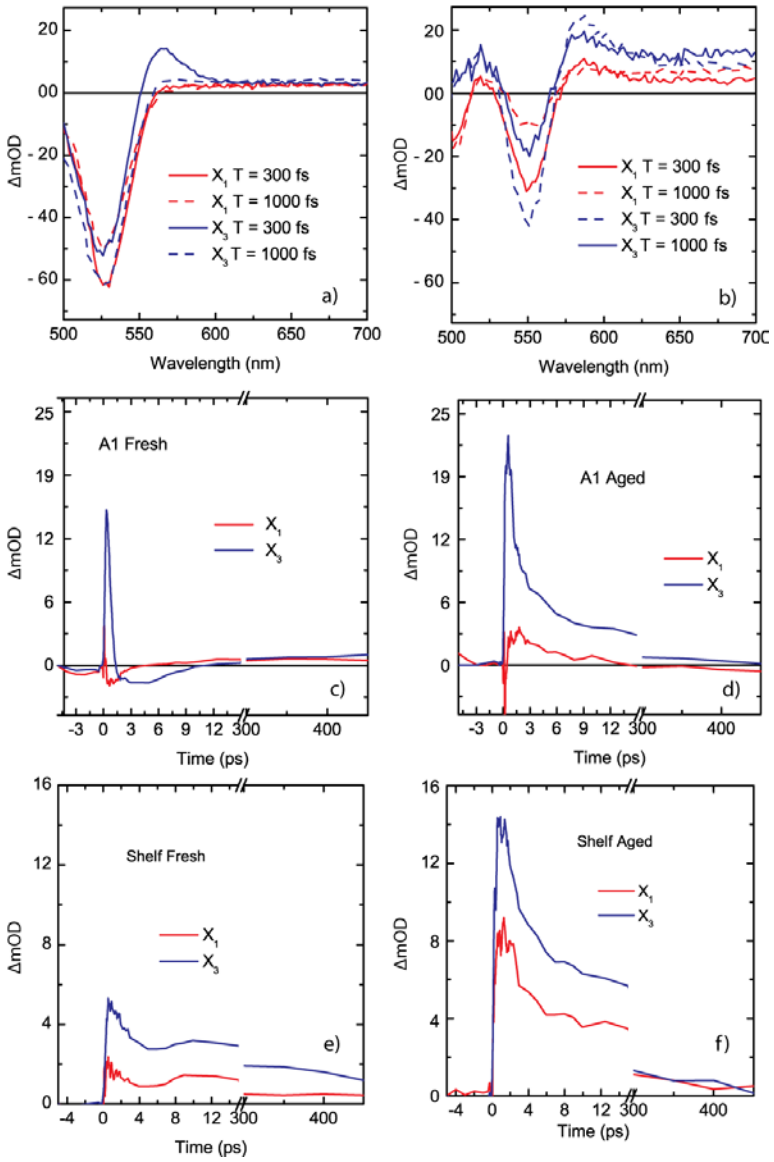

Figure 4.5 - TA spectra of fresh (a) and aged (b) samples with X_1 and X_3 pump at t = 100 / 300 / 1000 fs. Femtosecond pump/probe transients, probing at the narrowband PA (A1 feature) for fresh (λ_{probe} = 564 nm) (c) and aged (λ_{probe} = 577 nm) (d) samples. Femtosecond pump/probe transients, probing at the broadband PA (λ_{probe} = 661 nm) for fresh (e) and aged (f) samples

This broadband PA may be used as a spectroscopic signature of carrier trapping at the surface of the NC. In the case of prior work CdSe, [21] it was straightforward to assign this PA as arising from hole trapping. Here, such analysis is complicated by the presence of electron as well as hole trapping. These TA spectra which focus upon the PA signals clearly show that there is efficient surface trapping in CdTe and this trapping is further enhanced due to aging.

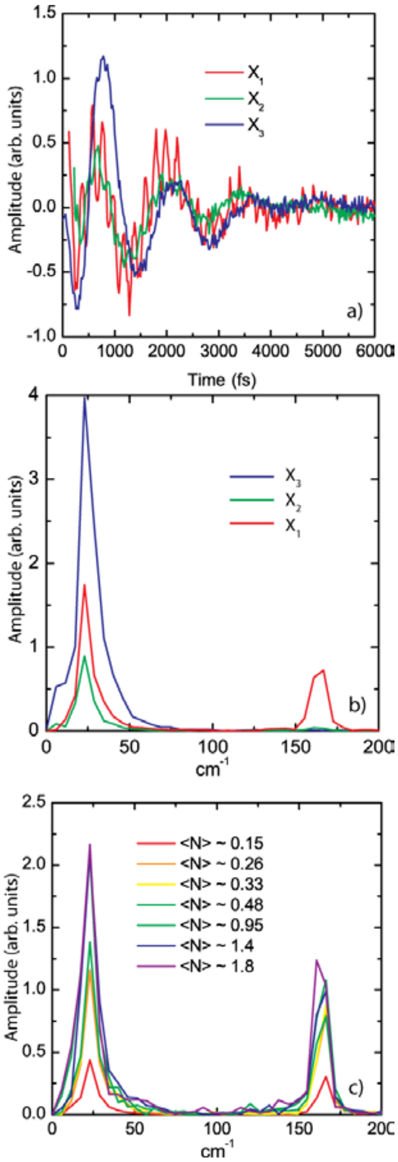

Figure 4.6 - Real time observation of coherent phonons as a direct measure of fast carrier trapping. (a) Initial excitonic state-dependence to the residual oscillations in the B1 transients for the aged CdTe. (b) FFT of the oscillations recovers the high frequency optical and the low frequency acoustic phonons. X_1 pumping uniquely enables simultaneous observation of both optical and acoustic phonons. (c) Excitation dependence to phonon spectra with X_1 pumping of aged CdTe.

4.3.4 Coherent Phonons

The excitonic state-dependence of the coupling of longitudinal optical (LO) and acoustic (LA) phonons in CdSe NC has been previously explored [6, 7, 78, 79] In particular, those results revealed specific excitonic state-dependence to optically excited coherent phonons in NC. Subsequently, it was found that additional non-optical carrier dynamics based mechanism can as well prepare coherent phonons.[75] Specifically, hot exciton surface trapping in phototreated CdSe created large amplitude coherent acoustic phonons by vibrationally impulsive hole capture at the surface of the NC. This hole capture creates a large piezoelectric effect across the NC interface thereby coupling the LA phonons. [75] Hence the observation of coherent phonons may serve as a marker for carrier dynamics (e.g. trapping), [73, 75] in addition to their more common use as means to evaluate exciton-phonon coupling via optical excitation. [78, 79, 104]

These experiments reveal that coherent optical and acoustic phonons are launched as revealed in the oscillations in the TA spectra. Subtraction of the non-oscillatory signal reveals the coherent phonons in detail, Figure 4.6. Figure 4.6a shows the state-dependence to the coherent oscillations for the first three excitonic states with an exciton density of <N> = 0.5 and probing at the peak of the derivative of the linear absorption spectrum. Figure 4.6b shows the FFT spectrum of these oscillations thereby showing simultaneous observation of both modes, enabling analysis of the manner in which they are excited as well as their coupling strengths. The coherent phonons show a clear state-dependence that is consistent with our prior work. [78, 79] Specifically, higher excitonic states do not reveal coherent LO phonons but do reveal the coherent LA phonons. The fluence dependence with excitation into the 1S type band edge exciton (X_1) reveals that the relative intensities do not scale equally, Figure 4.6c. Specifically, the LA intensity increases whereas the LO intensity saturates as discussed below.

4.4 Discussion: Excitation Induced Surface Trapping Dynamics

Whereas high quality CdSe NC passivated by organic ligands have been available for some time, a counterpart for CdTe has proved difficult to achieve, due to the presumed poorer surface quality of CdTe NC. Surface quality is further degraded during the course of aging. Hence one aims for spectroscopic signatures of surface trapping as well as aging so as to characterize the surface quality of the system as well as the ways in which surface conditions can dictate carrier relaxation and migration processes. Below we suggest how these various spectroscopic signals are connected via a simple electron transfer picture.

The band edge bleach (B1 signal) decays in these aged CdTe NC with a faster response than in fresh CdTe and CdSe NC. The decay at all fluences is well fit to a biexponential with two time constants, Figure 4.7a. The slow time constant of T_1 ~ 1.3 ps is fairly independent of excitation conditions. In contrast, the fast component, T_2, monotonically decreases up with fluence. The oscillation amplitudes of the LO and LA phonons also show a fluence dependence, represented by the mean occupancy, <N>. Figure 4.7b shows the ratio of the LA/LO amplitudes thereby using ratiometry of the oscillations as measure of any carrier trapping dynamics induced mechanism by which the phonons are triggered. The LA/LO ratio increases monotonically with <N>, much like the fast B1 decay component thereby suggesting correlation. Such a correlation between electron trapping and acoustic phonon coupling may be consistent with a simple electron transfer picture of surface trapping. Similar correlations were recently observed by Wachtvietl and co-workers for coherent optical phonons triggered by ultrafast electron transfer to adsorbed molecules[73].

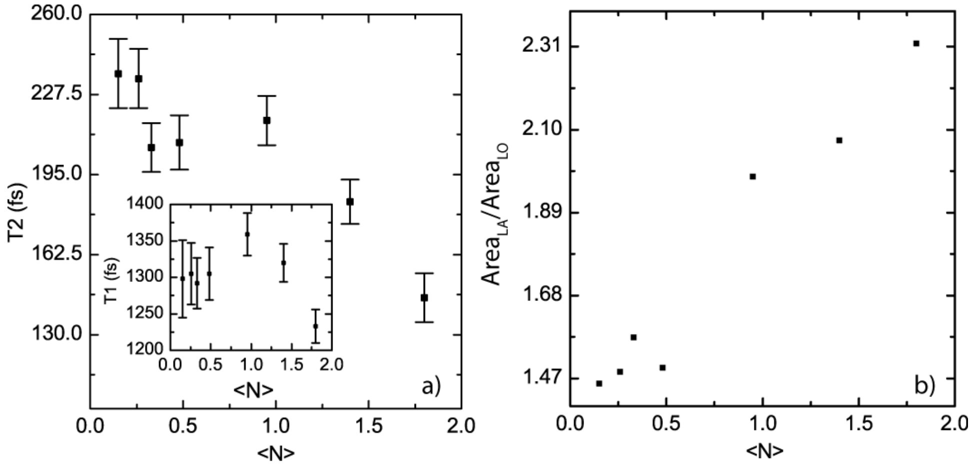

Figure 4.7 - Pump fluence dependence reveals a relation between the decay time and coherent phonon response in terms of the mean exciton occupancy, <N>. (a) Fluence dependence to the fast component of the B1 decay of aged CdTe with X_1 pumping. The inset shows the slow component has no fluence dependence. (b) Fluence dependence to the ratio of the integrated areas for the longitudinal acoustic (LA) / longitudinal optic (LO) phonons.

In a Marcus type electron transfer (ET) picture, [105] population transfer between the excitonic states and a surface trapped state implies a thermally activated process by which electrons and/or holes are transported from their excitonic core states to some surface state. Recent work by Jones and Scholes[106-108] has confirmed the applicability of this classically activated transport process as revealed by the temperature dependence of the photoluminescence (PL) decay times in CdSe based NC. This model has been recently[109] extended to a semiclassical Marcus-Jortner ET picture[105] which can explain the temperature dependence of the trap PL as well as the excitonic PL (Figure 4.8). The relevant point is that a classical activation barrier will produce a constraint on the rate at which surface trapping takes place. For CdSe NC, it was shown that surface trapping takes place on the 10-100 ps timescale.[21] In contrast, electron trapping from the band edge exciton in these

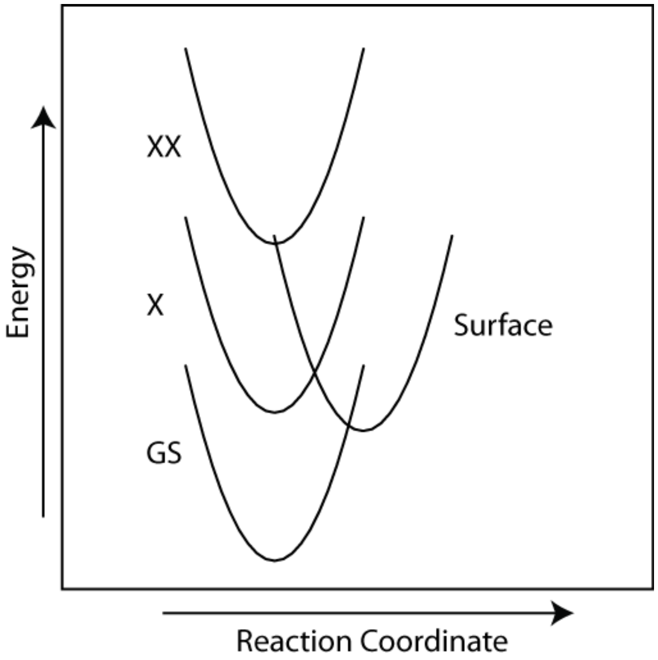

Figure 4.8 - Schematic illustration of surface trapping in an electron transfer scheme. Charge carrier trapping (electron or hole) from X to the surface as an activated electron transfer process. A biexciton (XX) has higher total energy ($E_{XX} = 2E_X - \Delta_{XX}$), with Δ_{XX} representing the biexciton

aged CdTe NC takes place on the timescale of 2 ps. This picture enables rationalization of the coherent phonon response.

At high fluence, sequential absorption from the single exciton (X) to the biexciton (XX) yields a state at high total energy. The total energy is twice the exciton energy minus the biexciton binding energy, $E_{XX} = 2E_X - \Delta_{XX}$.[7, 8, 21, 24, 76] With this amount of excess energy, the ET reaction can proceed in a barrierless manner[105] thereby increasing the trapping rate. The phenomenology of trap PL consistently reveals that it becomes more prominent at low temperatures. [109-111] Recent work provides a quantitative treatment of these observations in light of semiclassical Marcus-Jortner ET theory.[109] Qualitatively, one expects a barrier of ~ k_BT due to the temperature dependence of the trap PL over the range of 10 – 300 K. With an electron trapping time from the single exciton taking place in ~ 1.3 ps, barrier removal by absorption into XX predicts a trapping time of 200 – 300 fs, thereby rationalizing these observations.

4.5 Conclusions

Aging of semiconductor nanocrystals is well known to reduce the photoluminescence intensity by creating non-radiative traps at the surface. These simple PL experiments do not reveal the microscopic details by which the surface conditions dictate carrier relaxation and trapping processes. These femtosecond pump/probe experiments on fresh and aged CdTe semiconductor nanocrystals reveal a variety of carrier dynamical processes and the way in which they are influenced by the surface of the NC due to aging. It is shown that many of the core exciton dynamics of fresh and aged CdTe are consistent with CdSe NC – fast electron relaxation thereby breaking the phonon bottleneck, and strongly bound biexcitons. In addition, surface trapping related processes that arise due to aging of the NC are demonstrated. Specifically, aging alters the surface so as to produce efficient electron traps. These electron traps at the surface of the NC become more efficient for higher states, e.g. the biexcitons probed here. Trapping from the biexcitonic state is sufficiently rapid as to trigger coherent acoustic phonons as revealed in the pump/probe transients. These experiments reveal a rich manifold of signals available in pump/probe spectroscopy can be used to characterize surface trapping processes in semiconductor nanocrystals.

4.6 References

1. Alivisatos, A.P., Semiconductor clusters, nanocrystals, and quantum dots. Science (Washington, D. C.), 1996. **271**(5251): p. 933-7.
2. Nozik, A.J., Spectroscopy and hot electron relaxation dynamics in semiconductor quantum wells and quantum dots. Annual Review of Physical Chemistry, 2001. **52**: p. 193-231.
3. Efros, A.L. and M. Rosen, The electronic structure of semiconductor nanocrystals. Annual Review of Materials Science, 2000. **30**: p. 475-521.
4. Klimov, V.I., Optical Nonlinearities and Ultrafast Carrier Dynamics in Semiconductor Nanocrystals. Journal of Physical Chemistry B, 2000. **104**(26): p. 6112-6123.
5. Klimov, V.I., Spectral and dynamical properties of multilexcitons in semiconductor nanocrystals. Annual Review of Physical Chemistry, 2007. **58**: p. 635-673.
6. Kambhampati, P., Hot Exciton Relaxation Dynamics in Semiconductor Quantum Dots: Radiationless Transitions on the Nanoscale. The Journal of Physical Chemistry C, 2011. **115**(45): p. 22089-22109.
7. Kambhampati, P., Unraveling the Structure and Dynamics of Excitons in Semiconductor Quantum Dots. Accounts of Chemical Research, 2011. **44**(1): p. 1-13.
8. Kambhampati, P., Multiexcitons in Semiconductor Nanocrystals: A Platform for Optoelectronics at High Carrier Concentration. The Journal of Physical Chemistry Letters, 2012. **3**(9): p. 1182-1190.
9. Scholes, G.D. and G. Rumbles, Excitons in nanoscale systems. Nature Materials, 2006. **5**(9): p. 683-696.

10. Coe, S., et al., Electroluminescence from single monolayers of nanocrystals in molecular organic devices. Nature, 2002. **420**(6917): p. 800-803.

11. Rogach, Andrey L., et al., Light-Emitting Diodes with Semiconductor Nanocrystals. Angewandte Chemie International Edition, 2008. **47**(35): p. 6538-6549.

12. Klimov, V.I., et al., Single-exciton optical gain in semiconductor nanocrystals. Nature, 2007. **447**(7143): p. 441-446.

13. Klimov, V.I., et al., Optical gain and stimulated emission in nanocrystal quantum dots. Science, 2000. **290**(5490): p. 314-7.

14. Kambhampati, P., Z. Mi, and R. Cooney Ryan, Colloidal and Self-Assembled Quantum Dots for Optical Gain., in Comprehensive Nanoscience and Technology,, D.L. Andrews, D. Scholes Gregory, and G.P. Wiederrecht, Editors. 2011, Academic Press: Oxford. p. 493-542.

15. Cooney, R.R., et al., State-Resolved Manipulations of Optical Gain in Semiconductor Quantum Dots: Size Universality, Gain Tailoring, and Surface Effects. Journal of Chemical Physics, 2009. **131**: p. 164706.

16. Cooney, R.R., et al., Gain Control in Semiconductor Quantum Dots via State-Resolved Optical Pumping. Physical Review Letters, 2009. **102**(12): p. 127404.

17. Dias, E.A., et al., Improving Optical Gain Performance in Semiconductor Quantum Dots via Coupled Quantum Shells. The Journal of Physical Chemistry C, 2012. **116**(9): p. 5407-5413.

18. Gur, I., et al., Air-Stable All-Inorganic Nanocrystal Solar Cells Processed from Solution. Science, 2005. **310**(5747): p. 462-465.

19. Cooney, R.R., et al., Unified picture of electron and hole relaxation pathways in semiconductor quantum dots. Physical Review B (Condensed Matter and Materials Physics), 2007. **75**(24): p. 245311-14.

20. Cooney, R.R., et al., Breaking the Phonon Bottleneck for Holes in Semiconductor Quantum Dots. Physical Review Letters, 2007. **98**(17): p. 177403.

21. Sewall, S.L., et al., State-resolved studies of biexcitons and surface trapping dynamics in semiconductor quantum dots. Journal of Chemical Physics, 2008. **129**(8): p. 084701.

22. Hines, M.A. and P. Guyot-Sionnest, Synthesis and Characterization of Strongly Luminescing ZnS-Capped CdSe Nanocrystals. Journal of Physical Chemistry, 1996. **100**(2): p. 468-71.

23. Dabbousi, B.O., et al., (CdSe)ZnS Core-Shell Quantum Dots: Synthesis and Optical and Structural Characterization of a Size Series of Highly Luminescent Materials. Journal of Physical Chemistry B, 1997. **101**(46): p. 9463-9475.

24. Sewall, S.L., et al., State-resolved observation in real time of the structural dynamics of multiexcitons in semiconductor nanocrystals. Physical Review B, 2011. **84**(23): p. 235304.

25. Schaller, R.D., J.M. Pietryga, and V.I. Klimov, Carrier Multiplication in InAs Nanocrystal Quantum Dots with an Onset Defined by the Energy Conservation Limit. Nano Lett. FIELD Full Journal Title:Nano Letters, 2007. **7**(11): p. 3469-3476.

26. Klimov, V.I., Mechanisms for Photogeneration and Recombination of Multiexcitons in Semiconductor Nanocrystals: Implications for Lasing and Solar Energy Conversion. Journal of Physical Chemistry B, 2006. **110**(34): p. 16827-16845.

27. Franceschetti, A., J.M. An, and A. Zunger, Impact Ionization Can Explain Carrier Multiplication in PbSe Quantum Dots. Nano Letters, 2006. **6**(10): p. 2191-2195.

28. Schaller, R.D., V.M. Agranovich, and V.I. Klimov, High-efficiency carrier multiplication through direct photogeneration of multi-excitons via virtual single-exciton states. Nature Physics, 2005. **1**(3): p. 189-194.

29. Schaller, R.D. and V.I. Klimov, High Efficiency Carrier Multiplication in PbSe Nanocrystals: Implications for Solar Energy Conversion. Physical Review Letters, 2004. **92**(18): p. 186601/1-186601/4.

30. Nozik, A.J., et al., Semiconductor Quantum Dots and Quantum Dot Arrays and Applications of Multiple Exciton Generation to Third-Generation Photovoltaic Solar Cells. Chemical reviews, 2010. **110**(11): p. 6873-6890.

31. Nozik, A.J., Multiple exciton generation in semiconductor quantum dots. Chemical Physics Letters, 2008. **457**(1-3): p. 3-11.

32. Beard, M.C., et al., Multiple exciton generation in colloidal silicon nanocrystals. Nano Letters, 2007. **7**(8): p. 2506-2512.

33. Ellingson, R.J., et al., Highly efficient multiple exciton generation in colloidal PbSe and PbS quantum dots. Nano Letters, 2005. **5**(5): p. 865-871.

34. Nair, G., et al., Perspective on the Prospects of a Carrier Multiplication Nanocrystal Solar Cell. Nano Letters, 2011. **11**(4): p. 2145-2151.

35. McGuire, J.A., et al., Apparent Versus True Carrier Multiplication Yields in Semiconductor Nanocrystals. Nano Letters, 2010. **10**(6): p. 2049-2057.

36. Trinh, M.T., et al., In spite of recent doubts carrier multiplication does occur in PbSe nanocrystals. Nano Letters, 2008. **8**(6): p. 1713-1718.

37. Nair, G., et al., Carrier multiplication yields in PbS and PbSe nanocrystals measured by transient photoluminescence. Physical Review B, 2008. **78**(12).

38. Ben-Lulu, M., et al., On the Absence of Detectable Carrier Multiplication in a Transient Absorption Study of InAs/CdSe/ZnSe Core/Shell1/Shell2 Quantum Dots. Nano Letters, 2008. **8**(4): p. 1207-1211.

39. Tyagi, P. and P. Kambhampati, False multiple exciton recombination and multiple exciton generation signals in semiconductor quantum dots arise from surface charge trapping. Journal of chemical physics, 2011. **134**(9): p. 094706-10.

40. Trinh, M.T., et al., Anomalous Independence of Multiple Exciton Generation on Different Group IVâˆ'VI Quantum Dot Architectures. Nano Letters, 2011. **11**(4): p. 1623-1629.

41. Beard, M.C., et al., Variations in the Quantum Efficiency of Multiple Exciton Generation for a Series of Chemically Treated PbSe Nanocrystal Films. Nano Letters, 2009. **9**(2): p. 836-845.

42. Gdor, I., et al., Exploring Exciton Relaxation and Multiexciton Generation in PbSe Nanocrystals Using Hyperspectral Near-IR Probing. Acs Nano, 2012. **6**(4): p. 3269-3277.

43. Cordones, A.A., T.J. Bixby, and S.R. Leone, Evidence for Multiple Trapping Mechanisms in Single CdSe/ZnS Quantum Dots from Fluorescence Intermittency Measurements over a Wide Range of Excitation Intensities. The Journal of Physical Chemistry C, 2011. **115**(14): p. 6341-6349.

44. Zhao, J., et al., Challenge to the Charging Model of Semiconductor-Nanocrystal Fluorescence Intermittency from Off-State Quantum Yields and Multiexciton Blinking. Physical Review Letters, 2010. **104**(15).

45. Rosen, S., O. Schwartz, and D. Oron, Transient Fluorescence of the Off State in Blinking CdSe/CdS/ZnS Semiconductor Nanocrystals Is Not Governed by Auger Recombination. Physical Review Letters, 2010. **104**(15): p. 157404.

46. Peterson, J.J. and D.J. Nesbitt, Modified Power Law Behavior in Quantum Dot Blinking: A Novel Role for Biexcitons and Auger Ionization. Nano Letters, 2009. **9**(1): p. 338-345.

47. Kamat, P.V., Quantum Dot Solar Cells. Semiconductor Nanocrystals as Light Harvestersâ€ The Journal of Physical Chemistry C, 2008. **112**(48): p. 18737-18753.

48. Kamat, P.V., Meeting the Clean Energy Demand:â€‰ Nanostructure Architectures for Solar Energy Conversion. The Journal of Physical Chemistry C, 2007. **111**(7): p. 2834-2860.

49. Zhu, H.M., N.H. Song, and T.Q. Lian, Controlling Charge Separation and Recombination Rates in CdSe/ZnS Type I Core-Shell Quantum Dots by Shell Thicknesses. Journal of the American Chemical Society, 2010. **132**(42): p. 15038-15045.

50. Jin, S.Y., et al., Correlated single quantum dot blinking and interfacial electron transfer dynamics. Chemical Science, 2010. **1**(4): p. 519-526.

51. Huang, J., et al., Multiple Exciton Dissociation in CdSe Quantum Dots by Ultrafast Electron Transfer to Adsorbed Methylene Blue. Journal of the American Chemical Society, 2010. **132**(13): p. 4858-4864.

52. Boulesbaa, A., et al., Competition between Energy and Electron Transfer from CdSe QDs to Adsorbed Rhodamine B. Journal of Physical Chemistry C, 2010. **114**(2): p. 962-969.

53. Jin, S.Y. and T.Q. Lian, Electron Transfer Dynamics from Single CdSe/ZnS Quantum Dots to TiO2 Nanoparticles. Nano Letters, 2009. **9**(6): p. 2448-2454.

54. Yang, Y., W. RodrÃguez-CÃ³rdoba, and T. Lian, Multiple Exciton Generation and Dissociation in PbS Quantum Dot-Electron Acceptor Complexes. Nano Letters, 2012.

55. Zhu, H. and T. Lian, Enhanced Multiple Exciton Dissociation from CdSe Quantum Rods: The Effect of Nanocrystal Shape. Journal of the American Chemical Society, 2012. **134**(27): p. 11289-11297.

56. Zhu, H., et al., Wave Function Engineering for Efficient Extraction of up to Nineteen Electrons from One CdSe/CdS Quasi-Type II Quantum Dot. Journal of the American Chemical Society, 2012. **134**(9): p. 4250-4257.

57. Zhu, H., N. Song, and T. Lian, Wave Function Engineering for Ultrafast Charge Separation and Slow Charge Recombination in Type II Core/Shell Quantum Dots. Journal of the American Chemical Society, 2011. **133**(22): p. 8762-8771.

58. Krooswyk, J.D., C.M. Tyrakowski, and P.T. Snee, Multivariable Response of Semiconductor Nanocrystal-Dye Sensors: The Case of pH. The Journal of Physical Chemistry C, 2010. **114**(49): p. 21348-21352.

59. Snee, P.T., et al., Quantifying Quantum Dots through FÃ¶rster Resonant Energy Transfer. The Journal of Physical Chemistry C, 2011. **115**(40): p. 19578-19582.

60. Thakar, R., Y. Chen, and P.T. Snee, Efficient Emission from Core/(Doped) Shell Nanoparticles:â€‰ Applications for Chemical Sensing. Nano Letters, 2007. **7**(11): p. 3429-3432.

61. Snee, P.T., et al., A Ratiometric CdSe/ZnS Nanocrystal pH Sensor. Journal of the American Chemical Society, 2006. **128**(41): p. 13320-13321.

62. Lee, K., et al., (Ga1â€“xZnx)(N1â€“xOx) Nanocrystals: Visible Absorbers with Tunable Composition and Absorption Spectra. Nano Letters, 2012. **12**(6): p. 3268-3272.

63. Brown, K.A., et al., Characterization of Photochemical Processes for H2 Production by CdS Nanorodâ€“[FeFe] Hydrogenase Complexes. Journal of the American Chemical Society, 2012. **134**(12): p. 5627-5636.

64. Zhu, H., et al., Near Unity Quantum Yield of Light-Driven Redox Mediator Reduction and Efficient H2 Generation Using Colloidal Nanorod Heterostructures. Journal of the American Chemical Society, 2012. **134**(28): p. 11701-11708.

65. Schreuder, M.A., et al., Control of Surface State Emission via Phosphonic Acid Modulation in Ultrasmall CdSe Nanocrystals: The Role of Ligand Electronegativity. Journal of Physical Chemistry C, 2009. **113**(19): p. 8169-8176.

66. Bowers, M.J., et al., Structure and Ultrafast Dynamics of White-Light-Emitting CdSe Nanocrystals. Journal of the American Chemical Society, 2009. **131**(16): p. 5730-+.

67. Schreuder, M.A., et al., Encapsulated white-light CdSe nanocrystals as nanophosphors for solid-state lighting. Journal of Materials Chemistry, 2008. **18**(9): p. 970-975.

68. Dukes, A.D., et al., Pinned emission from ultrasmall cadmium selenide nanocrystals. Journal of Chemical Physics, 2008. **129**(12).

69. Pennycook, T.J., et al., Dynamic Fluctuations in Ultrasmall Nanocrystals Induce White Light Emission. Nano Letters, 2012. **12**(6): p. 3038-3042.

70. Rosson, T.E., et al., Bright White Light Emission from Ultrasmall Cadmium Selenide Nanocrystals. Journal of the American Chemical Society, 2012. **134**(19): p. 8006-8009.

71. Dukes, A.D., et al., Single-Nanocrystal Spectroscopy of White-Light-Emitting CdSe Nanocrystals. The Journal of Physical Chemistry A, 2011. **115**(16): p. 4076-4081.

72. Schreuder, M.A., et al., White Light-Emitting Diodes Based on Ultrasmall CdSe Nanocrystal Electroluminescence. Nano Letters, 2010. **10**(2): p. 573-576.

73. Dworak, L., et al., Coherent Longitudinal-Optical Ground-State Phonon in CdSe Quantum Dots Triggered by Ultrafast Charge Migration. Physical Review Letters, 2011. **107**(24): p. 247401.

74. Yu, W.W., et al., Experimental Determination of the Extinction Coefficient of CdTe, CdSe, and CdS Nanocrystals. Chemistry of Materials, 2003. **15**(14): p. 2854-2860.

75. Tyagi, P., et al., Controlling Piezoelectric Response in Semiconductor Quantum Dots via Impulsive Charge Localization. Nano Letters, 2010. **10**(8): p. 3062-3067.

76. Sewall, S.L., et al., Direct observation of the structure of band-edge biexcitons in colloidal semiconductor CdSe quantum dots. Physical Review B (Condensed Matter and Materials Physics), 2009. **80**(8): p. 081310(R).

77. Sewall, S.L., R.R. Cooney, and P. Kambhampati, Experimental tests of effective mass and atomistic approaches to quantum dot electronic structure: Ordering of electronic states. Applied Physics Letters, 2009. **94**(24): p. 243116-3.

78. Sagar, D.M., et al., State-Resolved Exciton-Phonon Couplings in CdSe Semiconductor Quantum Dots. Journal of Physical Chemistry C, 2008. **112**(25): p. 9124-9127.

79. Sagar, D.M., et al., Size dependent, state-resolved studies of exciton-phonon couplings in strongly confined semiconductor quantum dots. Physical Review B (Condensed Matter and Materials Physics), 2008. **77**(23): p. 235321-14.

80. Anderson, K.E.H., et al., Noise analysis and noise reduction methods in kilohertz pump-probe experiments. Review of Scientific Instruments, 2007. **78**(7): p. 073101-6.

81. Sewall, S.L., et al., State-to-state exciton dynamics in semiconductor quantum dots. Physical Review B: Condensed Matter and Materials Physics, 2006. **74**(23): p. 235328.

82. Kippeny, T.C., et al., Effects of surface passivation on the exciton dynamics of CdSe nanocrystals as observed by ultrafast fluorescence upconversion spectroscopy. Journal of Chemical Physics, 2008. **128**(8).

83. Garrett, M.D., et al., Band edge recombination in CdSe, CdS and CdSxSe1-x alloy nanocrystals observed by ultrafast fluorescence upconversion: The effect of surface trap states. Journal of Physical Chemistry C, 2008. **112**(33): p. 12736-12746.

84. Garrett, M.D., et al., Band edge dynamics in CdSe nanocrystals observed by ultrafast fluorescence upconversion. Journal of Physical Chemistry C, 2008. **112**(2): p. 436-442.

85. Underwood, D.F., T. Kippeny, and S.J. Rosenthal, Ultrafast Carrier Dynamics in CdSe Nanocrystals Determined by Femtosecond Fluorescence Upconversion Spectroscopy. Journal of Physical Chemistry B, 2001. **105**(2): p. 436-443.

86. Sykora, M., et al., Effect of Air Exposure on Surface Properties, Electronic Structure, and Carrier Relaxation in PbSe Nanocrystals. Acs Nano, 2010. **4**(4): p. 2021-2034.

87. McGuire, J.A., et al., New Aspects of Carrier Multiplication in Semiconductor Nanocrystals. Accounts of Chemical Research, 2008. **41**(12): p. 1810-1819.

88. McGuire, J.A., et al., Spectroscopic Signatures of Photocharging due to Hot-Carrier Transfer in Solutions of Semiconductor Nanocrystals under Low-Intensity Ultraviolet Excitation. Acs Nano, 2010. **4**(10): p. 6087-6097.

89. Efros, A.L. and M. Rosen, Random telegraph signal in the photoluminescence intensity of a single quantum dot. Physical Review Letters, 1997. **78**(6): p. 1110-1113.

90. Empedocles, S.A., et al., Photoluminescence from single semiconductor nanostructures. Advanced Materials (Weinheim, Germany), 1999. **11**(15): p. 1243-1256.

91. Son, D.H., et al., Second Harmonic Generation and Confined Acoustic Phonons in Highly Excited Semiconductor Nanocrystals. Journal of Physical Chemistry B, 2006. **110**(40): p. 19884-19890.

92. Son, D.H., J.S. Wittenberg, and A.P. Alivisatos, Multielectron Ionization of CdSe Quantum Dots in Intense Femtosecond Ultraviolet Light. Physical Review Letters, 2004. **92**(12): p. 127406/1-127406/4.

93. Burda, C., et al., New Transient Absorption Observed in the Spectrum of Colloidal CdSe Nanoparticles Pumped with High-Power Femtosecond Pulses. Journal of Physical Chemistry B, 1999. **103**(49): p. 10775-10780.

94. Norris, D.J., et al., Size dependence of exciton fine structure in CdSe quantum dots. Physical Review B: Condensed Matter, 1996. **53**(24): p. 16347-16354.

95. Norris, D.J. and M.G. Bawendi, Measurement and assignment of the size-dependent optical spectrum in CdSe quantum dots. Physical Review B: Condensed Matter, 1996. **53**(24): p. 16338-16346.

96. Efros, A.L. and M. Rosen, Quantum size level structure of narrow-gap semiconductor nanocrystals: Effect of band coupling. Physical Review B: Condensed Matter and Materials Physics, 1998. **58**(11): p. 7120-7135.

97. Zhong, H., et al., Electronic States and Exciton Fine Structure in Colloidal CdTe Nanocrystals. Journal of Physical Chemistry C, 2009. **113**(24): p. 10465-10470.

98. McArthur, E.A., et al., Charge Carrier Resolved Relaxation of the First Excitonic State in CdSe Quantum Dots Probed with Near-Infrared Transient Absorption Spectroscopyâ€ The Journal of Physical Chemistry B, 2010. **114**(45): p. 14514-14520.

99. An, J.M., et al., The Peculiar Electronic Structure of PbSe Quantum Dots. Nano Letters, 2006. **6**(12): p. 2728-2735.

100. Harbold, J.M., et al., Time-resolved intraband relaxation of strongly confined electrons and holes in colloidal PbSe nanocrystals. Physical Review B: Condensed Matter and Materials Physics, 2005. **72**(19): p. 195312/1-195312/6.

101. Kang, I. and F.W. Wise, Electronic structure and optical properties of PbS and PbSe quantum dots. Journal of the Optical Society of America B: Optical Physics, 1997. **14**(7): p. 1632-1646.

102. Schaller, R.D., et al., Breaking the Phonon Bottleneck in Semiconductor Nanocrystals via Multiphonon Emission Induced by Intrinsic Nonadiabatic Interactions. Physical Review Letters, 2005. **95**(19): p. 196401/1-196401/4.

103. Hu, Y.Z., et al., Biexcitons in semiconductor quantum dots. Physical Review Letters, 1990. **64**(15): p. 1805-7.

104. Kelley, A.M., Electronâˆ'Phonon Coupling in CdSe Nanocrystals. The Journal of Physical Chemistry Letters, 2010. **1**(9): p. 1296-1300.

105. Barbara, P.F., T.J. Meyer, and M.A. Ratner, Contemporary Issues in Electron Transfer Research. Journal of Physical Chemistry, 1996. **100**(31): p. 13148-13168.

106. Jones, M., S.S. Lo, and G.D. Scholes, Signatures of Exciton Dynamics and Carrier Trapping in the Time-Resolved Photoluminescence of Colloidal CdSe Nanocrystals. Journal of Physical Chemistry C, 2009. **113**(43): p. 18632-18642.

107. Jones, M., S.S. Lo, and G.D. Scholes, Quantitative modeling of the role of surface traps in CdSe/CdS/ZnS nanocrystal photoluminescence decay dynamics. Proceedings of the National Academy of Sciences of the United States of America, 2009. **106**(9): p. 3011-3016.

108. Jones, M., et al., Exciton trapping and recombination in type IICdSe/CdTe nanorod heterostructures. Journal of Physical Chemistry C, 2008. **112**(14): p. 5423-5431.

109. Mooney, J., et al., Challenge to the deep-trap model of the surface in semiconductor nanocrystals. Physical Review B, 2013. **87**(8):

110. Babentsov, V., et al., Excitation Dependence of Steady-State Photoluminescence in CdSe Nanocrystal Films. The Journal of Physical Chemistry B, 2005. **109**(32): p. 15349-15354.

111. de Mello DonegÃ¡, C., M. Bode, and A. Meijerink, Size- and temperature-dependence of exciton lifetimes in CdSe quantum dots. Physical Review B, 2006. **74**(8): p. 085320.

5 Two Dimensional Electronic Spectrometer

This chapter is in part a reproduction of a peer-reviewed and published article:

Tyagi, P. and Saari, J.I., Walsh, B. R., Kabir, A, Crozatier, V, Forget, N, Kambhampati, P. "**Two-color two-dimensional electronic spectroscopy using dual acousto-optic pulse shapers for complete amplitude, phase, and polarization control of femtosecond laser pulses.**" *The Journal of Physical Chemistry: A.* 2013.

Contributions by J.I. Saari and P. Tyagi represent the bulk of the technological and theoretical development of the manuscript respectively. B.R. Walsh and A. Kabir provided assistance throughout experimentation and analysis. V. Crozatier and N. Forget provided the acousto-optic programmable dispersive filters. P. Kambhampati was the principle investigator.

The manuscript represents the equal scientific contributions between co-first authors and has been rewritten for this dissertation by J.I. Saari.

2D instrument was implemented by J I Saari and P Tyagi. Experiments were performed by J I Saari. Final analysis and figures 5.6, 5.7 and 5.8 were done by P. Tyagi. Figure 5.5 was generated from data collected by N. Forget.

5.1 Introduction

The discussion of semiconductor nanocrystals thus far has unequivocally demonstrated one thing: more information is good information. Through photon-echo, pump-probe, a multitude of microscopy techniques, time-resolved fluorescence, and more, researchers have developed a toolbox of spectroscopic techniques to explore the various optical signatures available in nature.

All of these techniques, however, have one drawback: they are compressed representations of information. They involve (sometimes multiple) field matter interactions progressing through the various Feynman pathways as discussed in the introductory chapters. However, they ultimately present a one-dimensional projection of the acquired data. The most commonly drawn analogy is that of Nuclear Magnetic Resonance (NMR) imaging.[1, 2] Traditional 1 dimensional (1D) NMR probes a system through its response to nuclear spin-alignment via strong, pulsed magnetic fields. It provides a direct map of the various nuclear spin-environments within a system through their precession to equilibrium. However, it only indirectly provides information as to the coupling within the system. Based on the respective chemical shifts of the peaks in a 1D NMR experiment, one can infer relative nuclear positions within a given chemical structure. However, multi-dimensional NMR, with multiple controlled pulsed magnetic fields, provides not only information pertaining to the various nuclear spin-environments within a system, but also provides the couplings between them. In a fashion, it is a graphical mapping of the density matrix of the spin environments, while 1D NMR provides the diagonal elements, multi-dimensional NMR a more complete representation. Similarly, 1D optical spectroscopy reports on the respective transition energies and two-dimensional (2D) spectroscopy may provide the respective couplings, as well as clarify study of spectral features through deconvolving contributions by spectral diffusion. The power of multidimensional spectroscopy, as exemplified through the proliferation to ubiquity of multidimensional-capable NMR instrumentation amongst commercial and academic institutions alike, has recently brought new life to optical spectroscopies.[3-10]

Fourier transform 2D spectroscopy, as briefly touched upon in the introductory chapters, is a four-wave mixing, non-linear spectroscopic technique. First implemented in the infrared,[10] 2D spectroscopy has since expanded to the visible wavelengths.[11-13] As discussed in the opening chapter, the varying spectral regions report on differing potential energy coordinates of interest. Unlike other n-wave mixing techniques, however, 2D spectroscopy can provide a visual map of the 3rd order response of a system.[14, 15] The emitted signal field is derived through the various contributing Feynman pathways based on the prescribed phase-matching geometry as described in chapter 1. The Fourier transform of the heterodyned (or self-acted) signal created through sweeping the varying pulse arrival times leads to a double-projection about two frequency axis: a two-dimensional spectrum.

A generic pumping scheme, along with definitions for time intervals pertinent to analysis, as compared to the time ordering defined in the first chapter, is shown in figure 5.1**.** In a given experiment, the coherence time (τ_c) is swept in appropriate time-intervals depending on the highest frequency spectral feature of interest, as dictated by the Nyquist sampling rate. The population time remains static for any given coherence time sweep, but may be altered to acquire a population-time dependence of the two-dimensional spectrum. This population time sweeping can be used to monitor protein folding and structure, [16, 17] charge transfer and light harvesting,[13, 18-23] and excitonic interactions.[24-29] Given that the period of visible frequencies is on the order of ~2 fs, sub-femtosecond time-step precision may be required, outside of the rotating frame. This presents the first major experimental difficulty inherent to this technique, the need for inter-pulse optical delay with atto-second precision.

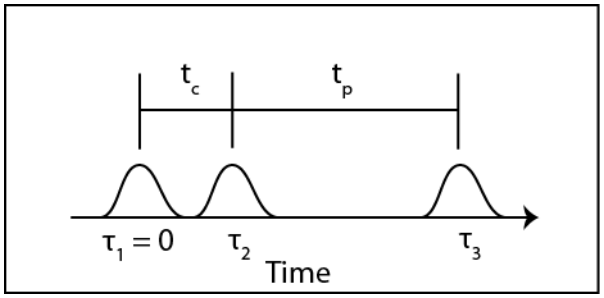

Figure 5.1 – Generic pulse sequence for pump/probe geometry 2D electronic experiment. Pump/probe geometry removes need for Local Oscillator.

The second major technical difficulty is the phase-stability requirements between pump-pulses as dictated by the nature of the detected signal. In essence, any relative shot-to-shot phase jitter between pulses while acquiring multiple spectra for each coherence time will lead to a washing out of the oscillations in the heterodyned signal. The difficulty in maintaining phase stability increases with increased pump energy.

Multiple techniques have been employed in an effort to meet the stringent temporal and phase-stability requirements inherent in multi-dimensional electronic spectroscopy. These approaches range from diffractive optics and glass wedges [3, 30] to acousto-optic programmable dispersive filters (AOPDF) [12, 31, 32] to spatial light modulators (SLM).[33] Through the lack of moving parts and limited calibration requirements, AOPDFs have separated themselves as a powerful alternative to mechanical pulse-pair generation and delay mechanism, such as the glass-wedge/diffractive optic techniques.[11, 12, 32, 34] The SLM method, championed by Nelson et al, has similarly automated much of the tedious work involved in 2D spectroscopy.[33, 35, 36] However, the automation and control over the three primary parameters in prescribing optical pulse trains, relative spatial orientation, phase, and polarization, with minimal calibration and tuning remains elusive.

The many light pulses present in any given two-dimensional electronic experiment provide for a myriad of possible experimental geometries, all depending on the desired signal of interest. Broadly, there exist two categories: collinear and non-collinear geometry. The linearity referring to the relative orientation of the probe and pump pulses.

The non-collinear geometries themselves also fall into two broad subcategories, as mentioned earlier, that of pump-probe and box-CARS, or similar. Box-CARS geometry provides an inherently background free detection method wherein the emitted signal field projects in the phase-matched direction of the three input pulses.

This background free detection has its own drawbacks, however, as both the rephasing and non-rephasing signals, due to the opposite sign for k, are emitted in opposite directions. Similarly, the signal field must often be heterodyned with a local oscillator.[8] In order to reconstruct the total absorptive signal (combination of rephasing and non-rephasing signals) a strong knowledge of the absolute phase of the local oscillator is required.[8]

Beyond the benefit of background free-detection, the box-CARS method allows for multiple spatial orientations, and subsequent wavevectors, for each input pulse.[3, 8] The multiple orientations provide a simple method for performing multiple-quantum measurements, assuming the phase stability required is present. Another benefit of the box-CARS geometry is that all possible phase-matched wavevector combinations are emitted.[8, 37] In principle, with only adjusting the location of the detector and the local oscillator, one could perform multiple non-linear spectroscopies simply by choosing the desired phase-matched signal to monitor.[37]

Pump-probe geometries have the benefit that both the rephasing and non-rephasing signals are emitted in the same direction, that of k_{probe}, as discussed in previous chapters.[11, 38] The subsequent self-action of the signal field removes the difficulty of reconstructing the signal field through the known local oscillator present in the box-CARS geometry. In fact, it removes the requirement of a fourth local oscillator pulse entirely. The difficulty comes from the strong background signal, however. Where in box-CARS geometries the wavevectors were used to tailor and tune the experiment, in pump-probe geometry the relative phases of the input pulses may be cycled to eliminate unwanted contributions.[8, 39]

While collinear geometry makes for an arguably simple experimental design, all possible phase matched signals arise in the same direction leading to a strongly convoluted signal. The guess work, however, involved in determining signal direction is completely removed. The combination of all emitted signals with the strong background signal requires a complex phase-cycling scheme in order to separate the desired outputs.[40]

The control over relative phase between pump-pulses has led to the design and implementation of many phase-cycling schemes similar to those used in NMR.[8, 41-43] Analogous to the wavevector separation method used through box-CARS geometry, phase-cycling makes use of the relative phases of the input pulses whose contribution manifests itself in the emitted signal field.[8, 38] This allows for Feynman pathway selection in the pump-probe and collinear geometries [8] and the subsequent separation of phasing and non-rephasing pathways.

Polarization control of the input pulses may also be used to enhance or supress peaks in 2D spectra easing analysis of the features of interest. For example, linearly polarized pumps may isolate a given molecular vibration or transition through increased dipole coupling, as discussed in the first chapter.

The complete automated control over the pulse parameter space in 2D spectroscopy could greatly extend the functionality and performance of a spectrometer. In this vein, this section will present a novel 2D electronic spectrometer design capable of complete pulse to pulse polarization and phase control with active phase-stability feedback through multiple AOPDFs. Proof-of-principle will be demonstrated through the two-colour 2D spectra of the proto-typical nanocrystal, CdSe.

5.2 – Experimental Details

The 2.5 mJ 1 KHz chirped-pulse amplifier (CPA) laser system used throughout the chapter has been described in detail in the introduction as well as elsewhere.[44, 45] Optical pulses were derived through CPA pumped optical parametric amplifiers (OPA) with sum-frequency generation (SFG) and second-harmonic generation (SHG) extensions. Similarly, a home-built non-collinear OPA was used as described in the introductory sections. Pulse compression was achieved through either custom-designed grating prism pairs (GRISMS) or a folded prism compressor. Final compression was achieved through the AOPDF. Pulse durations were measured through SHG-frequency resolved optical gating via AOPDFs, in the case of the broad-band NOPA, and intensity autocorrelation in a 30 μm BBO, cut at 55.2 and 29.2 for OPA derived pump and probe respectively. Phase stability was measured via spectral interferometry. Polarization was measured through a Mueller ellipsometer.

CdSe samples were used as received from NN-Labs and diluted to 200 mOD at band-edge as measured through a 1 mm pathlength flow cell (Starna Cells). The sample was circulated via peristaltic pumping. Linear absorption spectra were taken before and after experiment to ensure absence of a photoproduct.

2D spectra were acquired through a CCD coupled to a spectrometer (Princeton instruments). The coherence time was swept from -200 to 0 for a given population time. Phase cycling was performed on a shot to shot basis to limit long-term drift between $\Delta\varphi_{12} = 0$ and $\Delta\varphi_{12} = 180°$.

5.3 Results and Discussion

AOPDFs rely on the coupling between a radio-frequency wave and an optical pulse in a birefrigent crystal.[46, 47] In essence, an impingent optical pulse, when appropriately phase-matched, diffracts against a stationary acoustic wave onto the slow axis, as shown in figure 5.2. This acousto-optic coupling allows for complete pulse control through prescribed acoustic waves. As the acoustic waves are readily controlled through software, and subsequent RF drivers, optical pulse trains and experiments may be fully automated with little calibration required. AOPDFs have been applied towards 2D spectroscopy in the infrared[11] as well as visible wavelengths.[48]

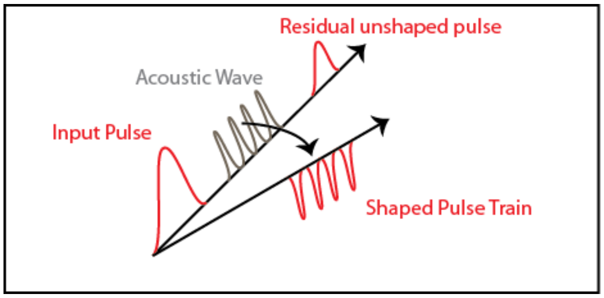

Figure 5.2 - Simplified representation of AOPDF shaping pulse train

5.3.1 – The Design

In order to achieve complete polarization and phase control, as well as active phase stability management through CEP feedback, independent control over each optical pulse is required. In this vein, a double AOPDF (Dazzler, Fastlite Inc) design is employed, as shown in figure 5.3. Regardless of visible

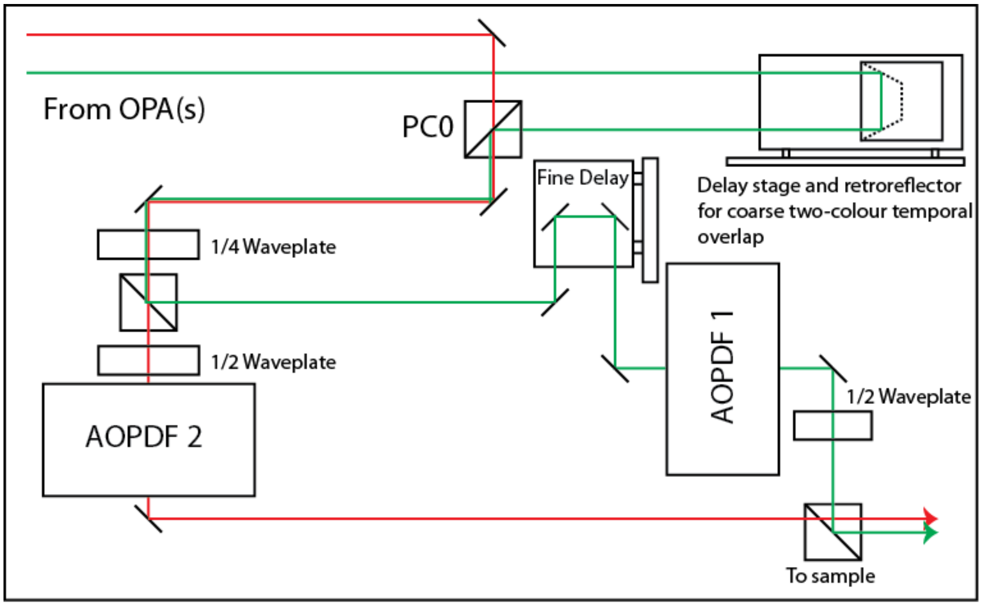

Figure 5.3 - Two colour setup using two acousto-optic programmable dispersive filters. Two manual delay stages are used to coarse adjust and fine tune optical path lengths to ensure time-zero is within delay capabilities of the AOPDFs.

wavelength input source, assuming sufficient pulse energy, this design allows for nearly arbitrary pulse train combinations. Incident linearly polarized light is made circularly polarized through the quarter waveplate, WP1. The light is then split through a polarized beam-splitting cube such that S (Vertical) and P (Horizontal) polarized light are sent to individual AOPDFs. Due to the AOPDF design, incident S-polarized light is required, necessitating the half-waveplate WP2. Upon acousto-optic coupling within the AOPDFs, both output pulses are linearly P-Polarized. WP3 may be used to adjust the final polarization of AOPDF 1. It should be noted that, in order for automated polarization control to occur, both output pulses must be orthogonally polarized before reaching the mixing cube PC2. A 4 cm delay stage is included pre-AODPF 1 in order to compensate for slight optical path length differences between the two arms of the spectrometer. PC2 is nested on a translation stage which, when translated, allows for the conversion between collinear and non-collinear geometries.

5.3.2 – Active Phase Stabilization and Control

Active phase stabilization was achieved through periodic feedback of measured phase-drift to the AOPDFs, as shown in figure 5.4. A beam-splitter directed a portion of the pump pulse pair towards a spectrometer where the shot-to-shot phase stability was measured through spectral interferometry (Figure 5.5a). Any spectral jitter or phase drift would result in the relative phase between the two optical pulses to deviate from a set CEP value (Figure 5.5b). The carrier frequency peak in the spectral interferogram was monitored for both with and without active stabilization and the resultant stability measurements are plotted in figure 5.5c,d. With active phase stabilization feedback at 100 Hz, the phase jitter measured was compensated for through active feedback via the CEP module to the RF driver of one of the AOPDFs. This active feedback resulted in a phase-stability in excess of $\lambda/_{300}$ for the hour monitored. The feedback mechanism is fully automated through control software managing the RF drivers therefore;

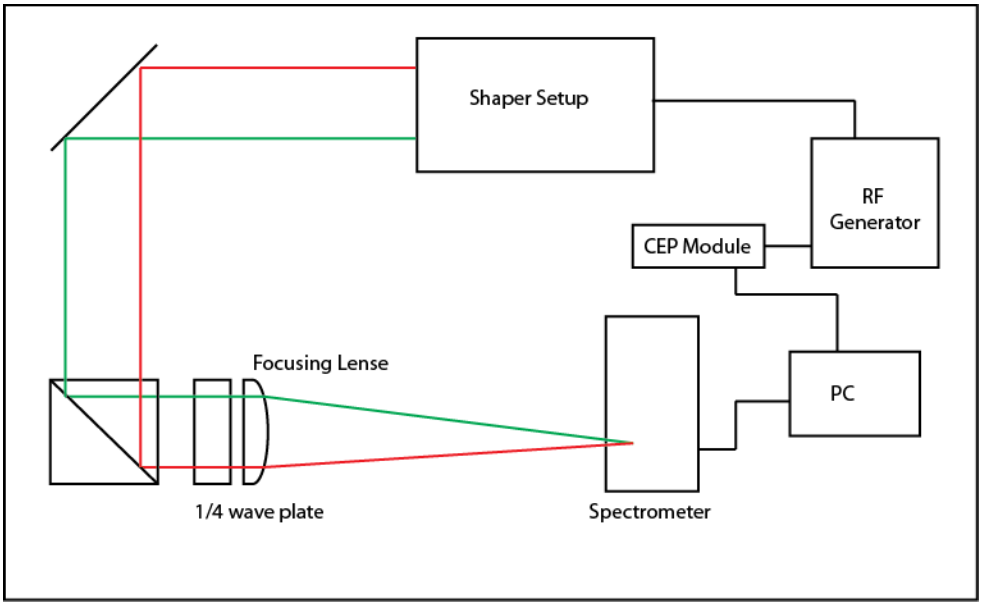

Figure 5.4 - Active feedback schematic. Note: red and green lines represent differing paths through spectrometer, not photon energy.

depending on relative importance of the desired data acquisition rate and over-all phase stability, the feedback rate may be adjusted to suit.

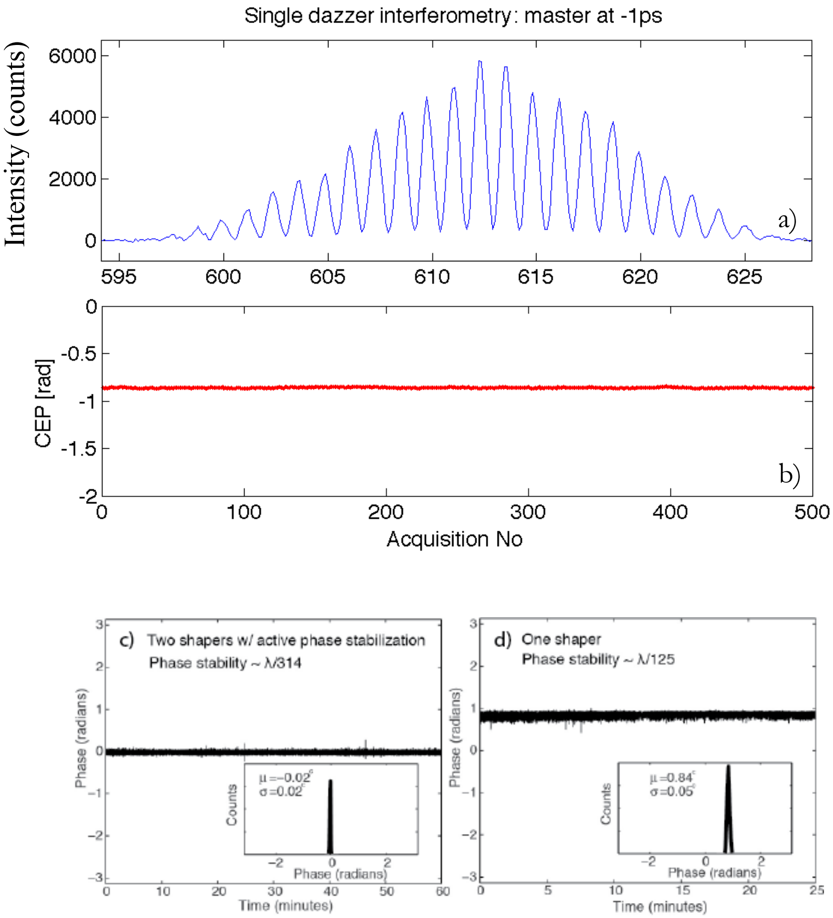

Figure 5.5 – a) Representative spectral interferogram used to measure phase-stability. b) Resultant phase stability over 500 shots for interferogram in a). c) Phase stability measure for active-feedback mechanism between two pulse-shapers. d) Phase stability measurement without active feedback.

5.3.3 – Polarization Control

The active phase-stability module, as well as the duel orthogonally polarized AOPDF outputs, allows for direct polarization control through recombination of the shaped pulses. Polarization control is achieved through adjusting the relative phases of the orthogonally polarized input pulses. After recombination in PC2, the resultant output polarization is given by, in a Jones matrix representation:

$$E_{Out} = \begin{bmatrix} E_s \\ E_p \end{bmatrix} = \begin{bmatrix} E_{0s}e^{i\varphi_s} \\ E_{0p}e^{i\varphi_p} \end{bmatrix} \tag{5.1}$$

where φ_i is the phase of the relative input pulse. This polarization control is made possible due through the high-phase stability acquired with active feedback.

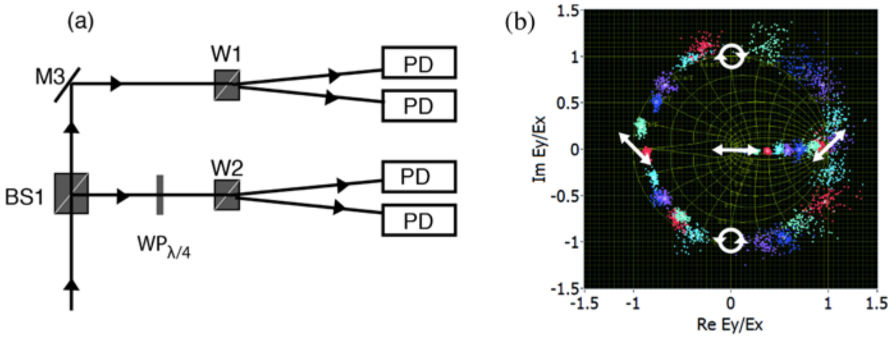

Figure 5.6 - a) schematic representation of Mueller ellipsometer used to determine polarization. b) Poincaré sphere showing compete polarization control.

Polarization control was demonstrated via decomposition of the polarization components in a Mueller ellipsometer, as shown in figure 5.6. The ellipsometer is comprised of two Wollaston prisms and four photodiodes. The relative intensities of the light as read by the four photo-diodes for a given pulse-pair input provides the polarization for that pulse-pair combination. Sweeping the phase of one pulse allows for a complete reconstruction of the Poincaré sphere, demonstrating full polarization control (Figure 5.6b).

5.3.4 2DE of CdSe Nanocrystals

Nanocrystals, due to their unique size-dependent properties and discreet excitonic transitions, present a remarkable area of study for multi-dimensional electronic spectroscopy.[24-27, 49, 50] As alluded to in the previous chapters, the multiexcitonic interactions, as well as various state-filling dynamics, provide a myriad of possibilities in terms of study through polarization controlled 2D spectroscopy. A typical transient absorption spectrum for CdSe nanocrystals is shown in figure 5.7a, along with the pump and probe energies used during the two-colour 2D experiment. The resulting two-colour absorptive spectra may be seen in figure 5.7b-d for the real, imaginary, and absolute value of the processed 2D signal for a population time of 500 fs. This observed cross-peak represents a direct coherence created between the X_1 and X_3 transitions. The orthogonal polarization between pump and probe, along with non-collinear pumping

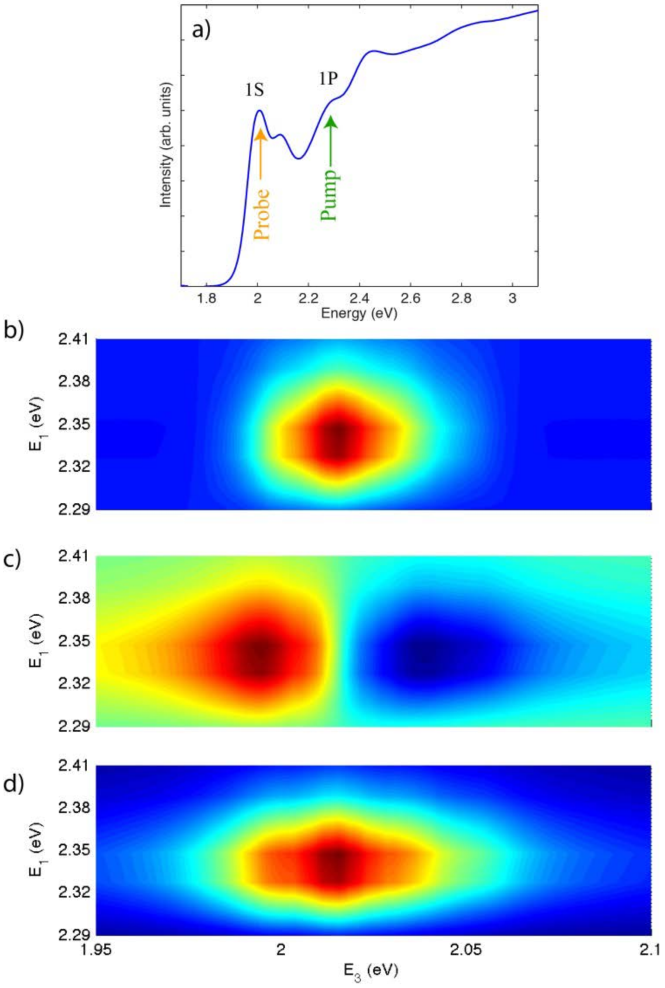

Figure 5.7- a) Linear absorption spectrum of CdSe NC. b-d) real, imaginary and absolute 2D absorptive spectra of CdSe NC at Tp = 500fs, Tc was swept from – 200 – 0 fs.

geometries, allowed for maximal rejection of pump scatter through an analyzer set $5°$ off pump polarization.[48]

The signal as a function of coherence time is shown in figure 5.8. The data was collected in a $0°, 180°$ shot-to-shot phase cycling scheme for $\Delta\varphi_{12}$ in the pump probe geometry. This phase cycling scheme allows for the direct subtraction of the DC response, such as the population dynamics and decay, and amplifies the 2D signal.

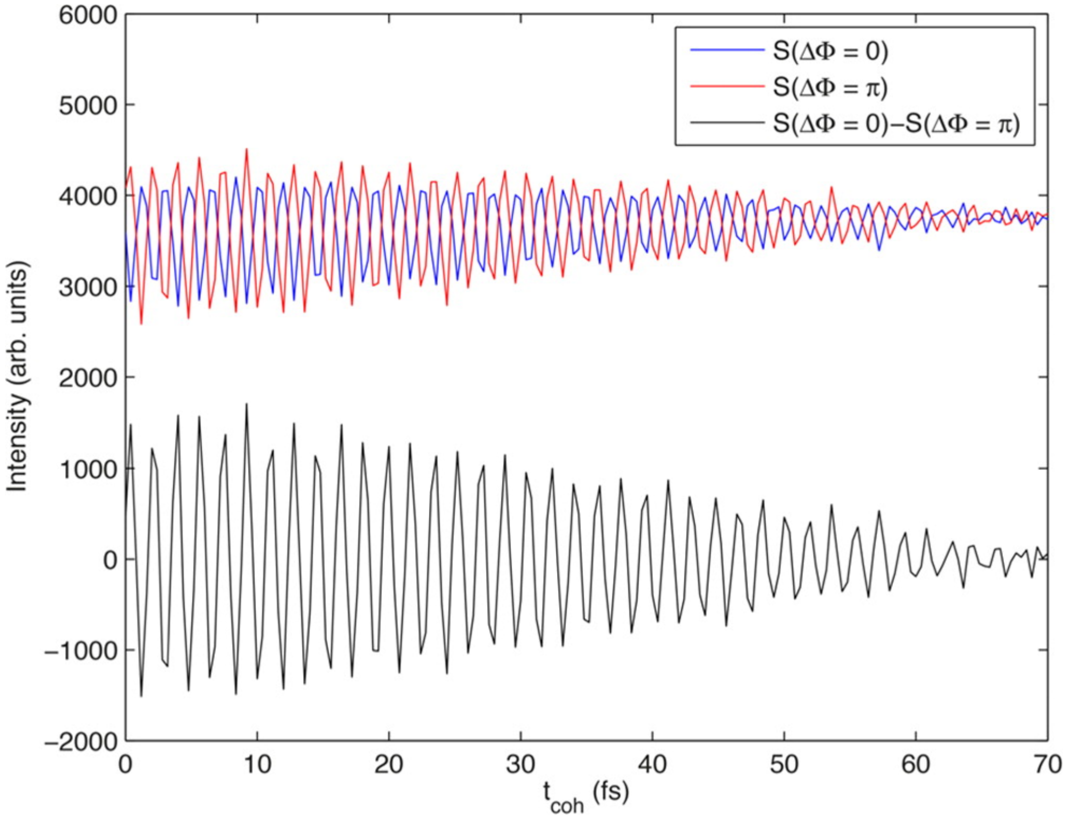

Figure 5.8 – Time domain signal as a function of τ_c. Red and blue trace represent shot/shot phase cycle raw data. Black trace is the subtraction, amplifying the oscillations and removing DC components.

In an effort to further demonstrate functionality of the novel 2D spectrometer, multiple 2D two-colour spectra were taken as a function of population time, figure 5.9a-e. The decay in the over-all intensity of the cross-peak is consistent with prior works (figure 5.9f).[24]

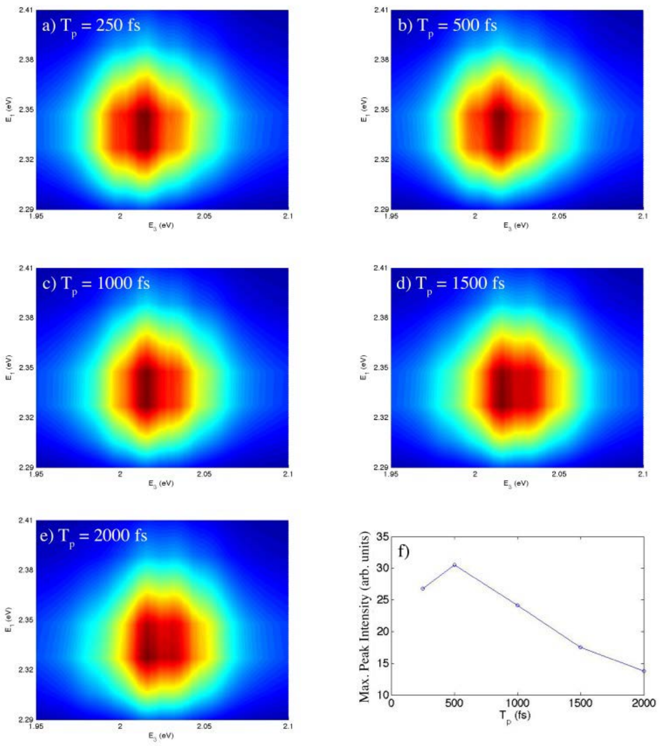

Figure 5.9 - a-e) 2D spectra of CdSe nanocrystals for differing population times. f) Peak intensity as a function of population time.

5.4 Conclusion

The design and proof of principle operation of a novel automated 2D electronic spectrometer through duel synched acousto-optic programmable dispersive filters was presented. Spatial orientation of pump and probe pulses was manipulated through translation of a beam-splitting cube ranging from collinear to non-collinear pump-probe geometries. Phase stability was measured in excess of λ/300 with active feed-back stabilization through spectral interferometry. Full mapping of the Pointe-Carre sphere was demonstrated through recombining AOPDF shaped pulses for full polarization control as measured in a Mueller ellipsometer. Two and one color 2D spectra of CdSe nanocrystals were measured using the described spectrometer design.

5.5 References

1. Jonas, D.M., Two-dimensional femtosecond spectroscopy. Annual Review of Physical Chemistry, 2003. 54(1): p. 425-463.
2. Wright, J.C., Coherent multidimensional vibrational spectroscopy. International Reviews in Physical Chemistry, 2002. 21(2): p. 185-255.
3. Brixner, T., et al., Phase-stabilized two-dimensional electronic spectroscopy. Journal of Chemical Physics, 2004. 121(9): p. 4221-4236.
4. Brixner, T., I.V. Stiopkin, and G.R. Fleming, Tunable two-dimensional femtosecond spectroscopy. Optics Letters, 2004. 29(8): p. 884-886.
5. Piryatinski, A., et al., Simulations of two-dimensional femtosecond infrared photon echoes of glycine dipeptide. Journal of Raman Spectroscopy, 2000. 31(1-2): p. 125-135.
6. Mukamel, S., Multidimensional femtosecond correlation spectroscopies of electronic and vibrational excitations. Annual Review of Physical Chemistry, 2000. 51: p. 691-729.
7. Gundogdu, K., et al., Multidimensional coherent spectroscopy made easy. Chemical Physics, 2007. 341(1-3): p. 89-94.
8. Zanni, P.H.a.M., Concepts and Methods of 2D Infrared Spectroscopy. 2011: Cambridge University Press.
9. Hochstrasser, R.M., Two-dimensional spectroscopy at infrared and optical frequencies. Proceedings of the National Academy of Sciences of the United States of America, 2007. 104(36): p. 14190-14196.
10. Asplund, M.C., M.T. Zanni, and R.M. Hochstrasser, Two-dimensional infrared spectroscopy of peptides by phase-controlled femtosecond vibrational photon echoes. Proceedings of the National Academy of Sciences, 2000. 97(15): p. 8219-8224.
11. Shim, S.-H. and M.T. Zanni, How to turn your pump-probe instrument into a multidimensional spectrometer: 2D IR and Vis spectroscopies via pulse shaping. Physical Chemistry Chemical Physics, 2009. 11(5): p. 748-761.
12. Myers, J.A., et al., Two-color two-dimensional Fourier transform electronic spectroscopy with a pulse-shaper. Opt. Express, 2008. 16(22): p. 17420-17428.
13. Brixner, T., et al., Two-dimensional spectroscopy of electronic couplings in photosynthesis. Nature, 2005. 434(7033): p. 625-628.
14. Hybl, J.D., A.A. Ferro, and D.M. Jonas, Two-dimensional Fourier transform electronic spectroscopy. Journal of Chemical Physics, 2001. 115(14): p. 6606-6622.

15. Mukamel, S., Y. Tanimura, and P. Hamm, Coherent Multidimensional Optical Spectroscopy. Accounts of Chemical Research, 2009. 42(9): p. 1207-1209.

16. Woys, A.M., et al., Parallel beta-Sheet Vibrational Couplings Revealed by 2D IR Spectroscopy of an Isotopically Labeled Macrocycle: Quantitative Benchmark for the Interpretation of Amyloid and Protein Infrared Spectra. Journal of the American Chemical Society, 2012. 134(46): p. 19118-19128.

17. Reddy, A.S., et al., Stable and Metastable States of Human Amylin in Solution. Biophysical Journal, 2010. 99(7): p. 2208-2216.

18. Schlau-Cohen, G.S., et al., Elucidation of the timescales and origins of quantum electronic coherence in LHCII. Nat Chem, 2012. 4(5): p. 389-395.

19. Lewis, K.L.M. and J.P. Ogilvie, Probing Photosynthetic Energy and Charge Transfer with Two-Dimensional Electronic Spectroscopy. The Journal of Physical Chemistry Letters, 2012. 3(4): p. 503-510.

20. Myers, J.A., et al., Two-Dimensional Electronic Spectroscopy of the D1-D2-cyt b559 Photosystem II Reaction Center Complex. The Journal of Physical Chemistry Letters, 2010. 1(19): p. 2774-2780.

21. Schlau-Cohen, G.S., A. Ishizaki, and G.R. Fleming, Two-dimensional electronic spectroscopy and photosynthesis: Fundamentals and applications to photosynthetic light-harvesting. Chemical Physics, 2011. 386(1–3): p. 1-22.

22. Cheng, Y.C. and G.R. Fleming, Dynamics of light harvesting in photosynthesis. Annu Rev Phys Chem, 2009. 60: p. 241-62.

23. Turner, D.B., et al., Quantitative investigations of quantum coherence for a light-harvesting protein at conditions simulating photosynthesis. Phys Chem Chem Phys, 2012. 14(14): p. 4857-74.

24. Turner, D.B., Y. Hassan, and G.D. Scholes, Exciton Superposition States in CdSe Nanocrystals Measured Using Broadband Two-Dimensional Electronic Spectroscopy. Nano Letters, 2012. 12(2): p. 880-886.

25. Wong, C.Y. and G.D. Scholes, Biexcitonic Fine Structure of CdSe Nanocrystals Probed by Polarization-Dependent Two-Dimensional Photon Echo Spectroscopy. Journal of Physical Chemistry A, 2011. 115(16): p. 3797-3806.

26. Block, S.B., et al., Multiresonant Multidimensional Spectroscopy of Surface-Trapped Excitons in PbSe Quantum Dots. Journal of Physical Chemistry Letters, 2012. 3(18): p. 2707-2712.

27. Yurs, L.A., et al., Multiresonant Coherent Multidimensional Electronic Spectroscopy of Colloidal PbSe Quantum Dots. Journal of Physical Chemistry C, 2011. 115(46): p. 22833-22844.

28. Turner, D.B., et al., Multiple-quantum 2D spectroscopy of many-body correlations in GaAs quantum wells, in Ultrafast Phenomena in Semiconductors and Nanostructure Materials Xiv, J.J. Song, et al., Editors. 2010.

29. Abramavicius, D., et al., Coherent Multidimensional Optical Spectroscopy of Excitons in Molecular Aggregates; Quasiparticle versus Supermolecule Perspectives. Chemical Reviews, 2009. 109(6): p. 2350-2408.

30. Cowan, M.L., J.P. Ogilvie, and R.J.D. Miller, Two-dimensional spectroscopy using diffractive optics based phased-locked photon echoes. Chemical Physics Letters, 2004. 386(1-3): p. 184-189.

31. Tian, P.F., et al., Femtosecond phase-coherent two-dimensional spectroscopy. Science, 2003. 300(5625): p. 1553-1555.

32. Shim, S.-H., et al., Automated 2D IR spectroscopy using a mid-IR pulse shaper and application of this technology to the human islet amyloid polypeptide. Proceedings of the National Academy of Sciences, 2007. 104(36): p. 14197-14202.

33. Turner, D.B., et al., Invited Article: The coherent optical laser beam recombination technique (COLBERT) spectrometer: Coherent multidimensional spectroscopy made easier. Review of Scientific Instruments, 2011. 82(8).

34. Grumstrup, E.M., et al., Facile collection of two-dimensional electronic spectra using femtosecond pulse-shaping technology. Optics Express, 2007. 15(25): p. 16681-16689.

35. Vaughan, J.C., et al., Diffraction-based femtosecond pulse shaping with a two-dimensional spatial light modulator. Optics Letters, 2005. 30(3): p. 323-325.

36. Wefers, M.M., H. Kawashima, and K.A. Nelson, AUTOMATED MULTIDIMENSIONAL COHERENT OPTICAL SPECTROSCOPY WITH MULTIPLE PHASE-RELATED FEMTOSECOND PULSES. Journal of Chemical Physics, 1995. 102(22): p. 9133-9136.

37. Brueggemann, B. and T. Pullerits, Nonperturbative modeling of fifth-order coherent multidimensional spectroscopy in light harvesting antennas. New Journal of Physics, 2011. 13.

38. Zhang, Z., et al., Phase-cycling schemes for pump-probe beam geometry two-dimensional electronic spectroscopy. Chemical Physics Letters, 2012. 550: p. 156-161.

39. Mukamel, S., Principles of Optical Non-linear Spectroscopy. 1995: Oxford University Press.

40. Keusters, D., H.S. Tan, and W.S. Warren, Role of pulse phase and direction in two-dimensional optical spectroscopy. Journal of Physical Chemistry A, 1999. 103(49): p. 10369-10380.

41. Wagner, W., et al., Rapid phase-cycled two-dimensional optical spectroscopy in fluorescence and transmission mode. Optics Express, 2005. 13(10): p. 3697-3706.

42. Vaughan, J.C., et al., Coherently controlled ultrafast four-wave mixing spectroscopy. Journal of Physical Chemistry A, 2007. 111(23): p. 4873-4883.

43. Tan, H.-S., Theory and phase-cycling scheme selection principles of collinear phase coherent multi-dimensional optical spectroscopy. Journal of Chemical Physics, 2008. 129(12).

44. Anderson, K.E.H., et al., Noise analysis and noise reduction methods in kilohertz pump-probe experiments. Review of Scientific Instruments, 2007. 78(7): p. 073101-6.

45. Tyagi, P., et al., Two-Color Two-Dimensional Electronic Spectroscopy Using Dual Acousto-Optic Pulse Shapers for Complete Amplitude, Phase, and Polarization Control of Femtosecond Laser Pulses. J Phys Chem A, 2013.

46. Verluise, F., et al., Amplitude and phase control of ultrashort pulses by use of an acousto-optic programmable dispersive filter: pulse compression and shaping. Opt. Lett., 2000. 25(8): p. 575-577.

47. Tournois, P., Acousto-optic programmable dispersive filter for adaptive compensation of group delay time dispersion in laser systems. Optics Communications, 1997. 140(4–6): p. 245-249.

48. Myers, J.A., et al., Two-color two-dimensional Fourier transform electronic spectroscopy with a pulse-shaper. Optics Express, 2008. 16(22): p. 17420-17428.

49. Yang, L. and S. Mukamel, Revealing exciton-exciton couplings in semiconductors using multidimensional four-wave mixing signals. Physical Review B, 2008. 77(7).

50. Griffin, G.B., et al., Two-dimensional electronic spectroscopy of CdSe nanoparticles at very low pulse power. Journal of Chemical Physics, 2013. 138(1).

6 Concluding Remarks and Future Works

6.1 Concluding Remarks

The preceding discussion represents an original scientific contribution by the author. Traditionally, the augmented Auger recombination rates present in semiconductor nanocrystals represented the principle issue in developing nanocrystal-based laser devices. However, when combined with the multiexcitonic binding energies unique to colloidal nanocrystals, these fast recombination rates present a novel platform towards all-optical signal processing and generation. The state-resolved pump-probe spectroscopic technique, combined with tailored pulse sequences, was used to manipulate the optical gain profile of CdSe/ZnS nanocrystals dispersed in toluene. The stimulated emission was modulated through prescribed multiexctionic multiplicity as dictated by appropriately pumping the X_1 and X_4 transitions. The carrier signal, as given by biexcitonic stimulated emission, was modulated both in amplitude and frequency at rates reaching 1 THz. These frequency modulation channels arise from increased multiexcitonic character of the stimulated emission. These channels, based on the nature of multiexcitonic interactions within the NCs, were shown to act in a Boolean AND logic gating scheme.

However, the general description of the semiconductor nanocrystal is that of a particle in a perfectly passivated environment. Many of the discussions surrounding the various limitations and spectroscopic signals ignore surface trapping. State resolved femtosecond pump-probe experiments were performed on fresh and aged CdTe nanocrystals in order to investigate the role of the surface in hot charge carrier trapping. The aged CdTe nanocrystals demonstrated increased electronic relaxation, as monitored by the band-edge bleach, as well as the broad photoinduced absorption ‘shelf’ to the red edge of the transient absorption spectrum. Similarly, steady state experiments demonstrated a stark decrease in photoluminescence intensity with aging. The fluence and state dependence of the increased electronic relaxation rate once again demonstrates a breaking of the phonon bottleneck for nanocrystals through increased surface trapping. The multiexcitonic trapping rate was found to impulsively launch acoustic phonons as monitored by frequency modulation of the absorption spectrum. The combination of phonon and transient absorption spectral data provide a multitude of spectroscopic signatures indicating surface degradation.

The myriad of spectral signatures and the convoluted nature of spectral features drove the design of a novel two-dimensional electronic spectrometer design. Two acousto-optic programmable dispersive filters paired with a CEP module, and spectral interferometry to measure phase jitter, provided phase stable pulse pairs with values in excess of $\lambda/300$ through active CEP feedback. This phase stability allowed for complete polarization control through the recombination of orthogonally polarized pulses in a beam splitter. Polarization states were achieved via setting the relative phase between pulse components and were measured through a Mueller ellipsometer. Proof of principle 2DE experiments were performed on CdSe nanocrystals and results were in agreement with prior works.

6.2 Future Works

Often when writing a dissertation everything just ‘clicks’. Ideas for potential experiments start rushing in as you peruse the literature. Unfortunately, these ideas often come hand-in-hand with sleep, leaving their memory to be muddled by morning. Throughout my time at McGill, I’ve managed to scribble a few ideas down in time, one leading to the article presented in chapter 3. Similarly, time as a graduate student is often spent sifting through half-completed projects. The following section will outline a few technical and experimental ideas in the hopes of expanding upon the work discussed throughout the dissertation.

For the sake of brevity, proposals have been limited to at most 2 pages with figure.

6.2.1 Single Excitonic Gain

The interplay between the induced absorption caused through formation of biexcitons and the stimulated emission from the single excitonic state is the Achilles heel of low lasing thresholds in simple colloidal nanocrystals.[1-4] Multiple efforts have been made to tune the relative interaction energies of multiple excitons from gradient alloying to exotic doped nanocrystals. Klimov et al. successfully demonstrated single excitonic gain through manipulating the biexcitonic binding energy.[1] However, this is only a part of the story. The Stokes shift as dictated by both the fine-structure and phonon coupling within nanocrysts could similarly be tuned.

The key point made by Klimov et al. was the necessity of a roughly 100 meV shift in the binding energy to attain single excitonic gain. In essence, this relative scaling of energy difference between induced absorption frequencies and emission frequencies has only been tried for one direction. In order to tailor a system for single excitonic emission, I introduce the following figure of merit:

$$|\Delta XX_{ABS} - \delta X_{EM}| > 100\ meV \tag{9.1}$$

where δX_{EM} is the single excitonic stokes shift and ΔXX_{ABS} is the absorptive binding energy.

Cadmium Telluride nanocrystals exhibit a large stokes shift, on the order of 100 meV, in the visible spectrum.[5] They also exhibit biexctionic binding energies similar to those found in CdSe nanocrystals, as found in preliminary work by the author. Considering equation 9.1:

$$|30\ meV - 100\ meV| = 70\ meV \tag{9.2}$$

making CdTe nanocrystals a prime candidate for single-excitonic emission.

Preliminary studies, as reported in the previous chapters, have shown that, due to the small size of visible emitting CdTe caused by their narrower bulk bandgap, surface trapping is a major factor when considering emission from CdTe nanocrystals. Capping CdTe in a Type-I fashion should limit the influence of surface trapping, improving their candidacy as single-excitonic lasing media. Experiments to this effect would provide insight into the relative nature of the interplay between emitting and absorbing band-edge states in multiexcitons, as suggested by equation 9.1.

6.2.2 Simultaneous Detection of MX Recombination Through Concurrent Time-resolved PL and Transmission Differential Absorption Spectroscopy

The quantization of Auger relaxation rates was first suggested by Klimov et al.[6] This was achieved through transient absorption spectroscopy in the transmission geometry. Similar state-resolved and infrared studies, as well as time-resolved fluorescence studies, have been performed in an effort to quantify Auger relaxation rates [7-10] through both inter- and intraband relaxation dynamics. The following is a proposal for a combined time-resolved photoluminescence transient absorption instrument capable of directly monitoring X, XX, and MX recombination rates through simultaneous data collection.

The design proposed may be seen in figure 6.1. The state-resolved transient absorption system is similar to that described in the previous chapters, however, the experimental timing is now synched to an Axis Photonics time resolved streak camera with ~1-5 Picosecond time resolution.

State-resolved fluence dependent studies on CdSe nanocrystals in solution using the above technique would provide direct measurement of multiexcitonic interactions and their potential roles in switching devices. For example, pumping the X_1 transition directly and monitoring the subsequent PL and transient absorption spectra for increasing fluence would give the spectral behaviour of X moving to XX with fluence as well as directly correlate transmitted Auger recombination and PL decay. Similarly, the system could be accompanied with a cryostat to allow for concurrent temperature dependent studies of the relevant relaxation rates and surface PL. The fluence, and pump-energy dependent studies would allow for a complete mapping of the correlation between charger carrier energy and relaxation rate through radiative and non-radiative pathways. Thermodynamics and kinetics would be accounted for through implementation of a cryostat.

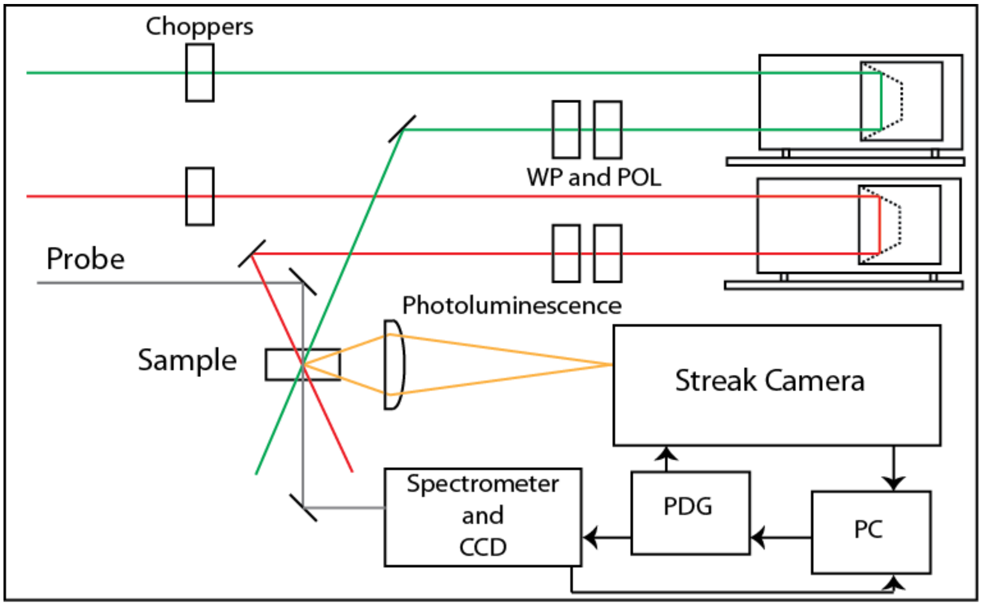

Figure 6.1 – State-Resolved Transient absorption/photoluminescence spectrometer. Timing controlled via PC and PDG (Berkley Electronics). Master clock signals from Oscillator (76 MHz) and master Trigger from Regenerative Amplifier (1 KHz).

6.2.3 Time Resolved PLE

The above spectrometer may be converted to include time-resolved photoluminescence excitation spectra through the simple addition of a broad-band pump source, such as the NOPA described in previous chapters. In order to automate the time-resolved PLE instrument, the output of the NOPA would pass through an AOPDF to allow for spectral selection of the pump wavelength. The AOPDF would cycle through the excitation bandwidth while the time-resolved photoluminescence spectra are captured by the streak camera. This would provide the time-resolved photoluminescence spectra as a function of excitation photon energy, giving valuable information as to the various levels of competition kinetics leading to the so-called photoexcitation spectrum. Including an emitter of known quantum efficiency would give insight as to the relative radiative and non-radiative dynamics based on the quantum yield as a function of time and excitation photon energy.

6.2.4 Sol-Gel Embedded Nanocrystals: Towards Efficient All Optical Signal Processing

Ultimately, in order for the optical signal processing device described in chapter 3 to become a reality, nanocrystals will have to be embedded in a support matrix, or, in optical fibers. Similarly, the chosen nanocrystal would have to operate in the infrared telecom window. In an effort to develop solid-state devices, preliminary work on embedding Rhodamine 6G in Su8 photoresist waveguide material and subsequently measuring the ASE through optical excitation was performed as shown in Figure 6.2.

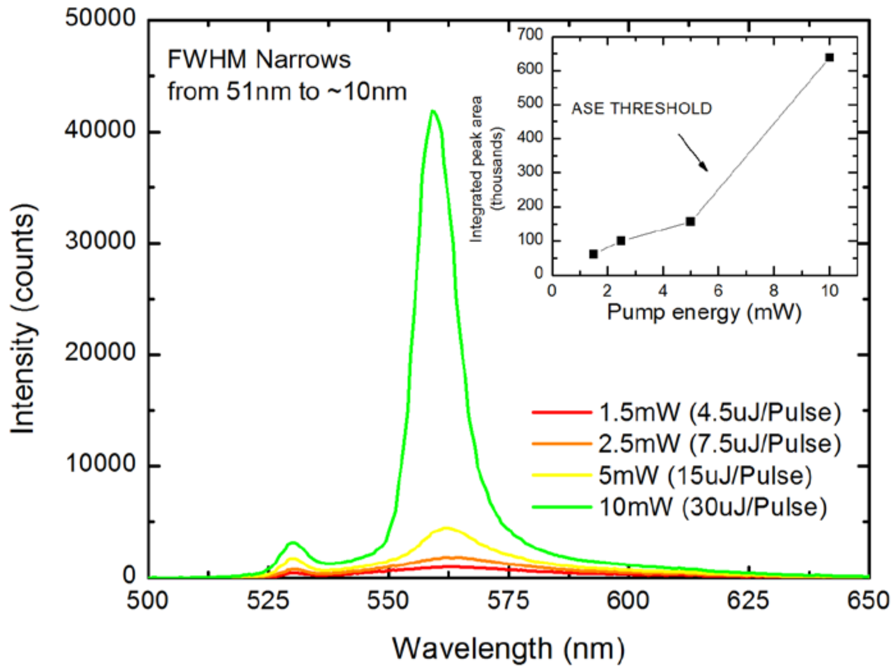

Figure 6.2 - PL and ASE as a function of pump fluence for Rh6G:Su8

The end goal being to embed CdSe/ZnS into multiple processing domains as to mimic an all-optical router, as shown in figure 6.3.

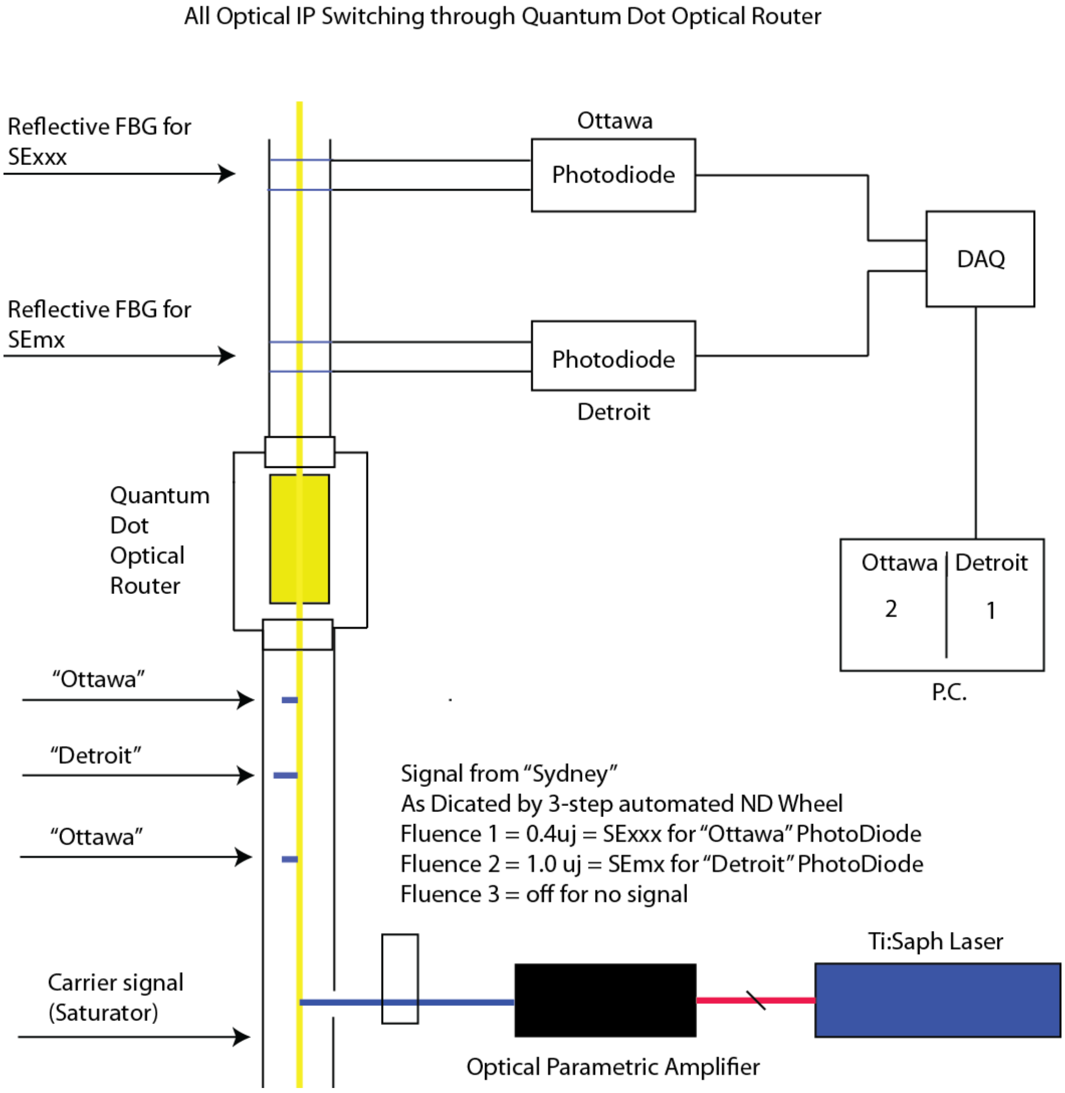

Figure 6.3 – Schematic representation of all-optical nanocrystal router experiment.

In essence, PbSe nanocrystals embedded within an Su8 waveguide matrix would emit with increased multiexcitonic character depending on incident pumping scheme, as described in chapter 3. Fiber Bragg Gratings would act as filters for the various prescribed stimulated emission profiles in order to direct optical traffic to the desired location. Data acquisition cards and Photodiodes would be used to track results.

6.2.5 Fully Automated Broadband 2D Electronic Spectrometer

The two-dimensional electronic spectrometer described in chapter 5 suffered from two major flaws: 1) the bandwidth accessible to the device was limited by the operating window of the GRISMs or prisms used to compress the initial pulse and 2) the compression had to be adjusted each time a new spectral window was desired. In order to overcome these limitations and to subsequently provide a complete, one box, automated 2D electronic spectrometer the design outlined in figure 6.4 is proposed.

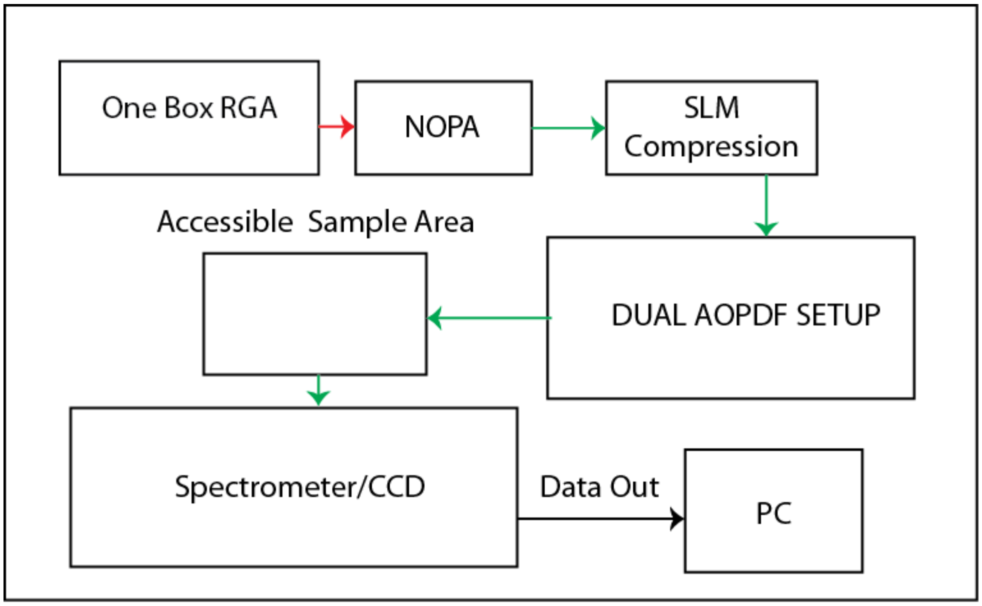

Figure 6.4 – Schematic representation of proposed automated 2DE instrument.

Through implementation of a simple, 1 box amplifier, a broadband NOPA, a Spatial Light Modulator (SLM), and the dual AOPDF design outlined in chapter 5, two-dimensional electronic spectroscopy could become turn-key. The SLM would simply be used to compress the output of the NOPA. Similar commercial approaches have been taken in the infrared using AOPDFs.

6.2.6 Ultrafast Electron Diffraction of CdSe Nanocrystals

The various phonon modes and their respective coupling to optical excitation in nanocrystals has dominated much of the discussion of the general stokes shift and temperature dependence of the emittive states in semiconductor nanocrystals.[11-16] In fact, the phonon progressions manifest themselves in nearly all discussion of the optical properties of semiconductor nanocrystals.

Considering the proposed necessity of coupling to phonons, either through ligand assisted non-adiabatic channels or direct coupling, a great deal of theoretical and spectroscopic studies have been performed in an effort to elucidate the various coupling mechanisms. The acoustic phonon, for example, has been attributed to a spherical breathing mode in CdSe nanocrystals through either piezoelectric or deformation potential arguments.[13, 15] The optical phonon at roughly 208 cm^{-1} arises through long-range Frohlich coupling mechanisms.[13] While these studies have relied on indirect optical measurement through impulsive ultrafast spectroscopy or varied Raman techniques, ultrafast electron diffraction could provide direct observation of the periodic structural vibrations through peak fluctuations in the radially averaged powder diffraction pattern given sufficiently compressed electron bunches.[17-19]

A steady-state powder diffraction pattern of a given CdSe nanocrystal drop cast on a carbon supported TEM grid, as acquired in a TEM, is shown in figure 6.6. In a pump-probe electron diffraction experiment, upon optical excitation, the various atoms will begin to vibrate about their lattice sites, as described in chapter 2. The in-phase oscillations should manifest themselves in a radial expansion and compression of the various rings in the diffraction pattern shown in figure 6.5 as a function of time. This technique could give direct observational evidence as to the various structural frequencies and couplings for the phonon modes in nanocrystals. Similarly, state-resolved and fluence studies, along with capping and aging studies, would provide a direct measure of the various influences of various ligands and the phonon modes, including excitonic temperature.

Similarly, environmental temperature dependence of nanocrystal phonon modes and spectral features could be studied optically, as well as through UED, with the implementation of a cold-finger cryostat within the UED chamber.

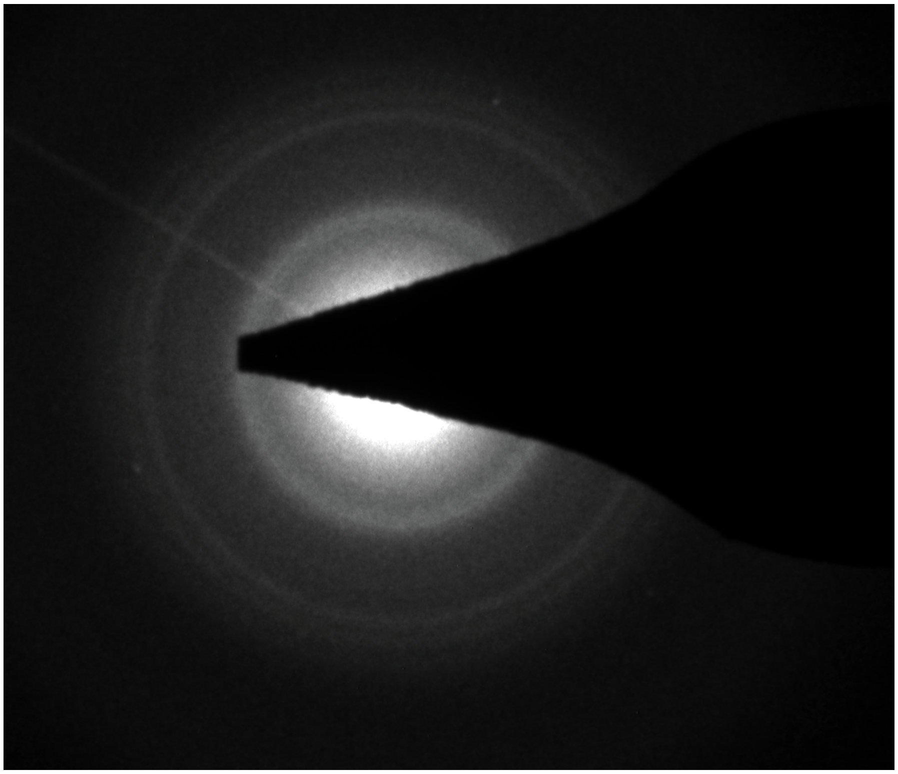

Figure 6.5 – Steady-state powder diffraction pattern of nanocrystal on carbon TEM grid.

THANK YOU

6.3 References

1. Klimov, V.I., et al., Single-exciton optical gain in semiconductor nanocrystals. Nature, 2007. **447**(7143): p. 441-446.

2. Malko, A.V., et al., Interplay between optical gain and photoinduced absorption in CdSe nanocrystals. Journal of Physical Chemistry B, 2004. **108**(17): p. 5250-5255.

3. Cooney, R.R., et al., Gain Control in Semiconductor Quantum Dots via State-Resolved Optical Pumping. Physical Review Letters, 2009. **102**(12): p. 127404.

4. Cooney, R.R., et al., State-resolved manipulations of optical gain in semiconductor quantum dots: Size universality, gain tailoring, and surface effects. Journal of Chemical Physics, 2009. **131**(16).

5. Zhong, H., et al., Electronic States and Exciton Fine Structure in Colloidal CdTe Nanocrystals. The Journal of Physical Chemistry C, 2009. **113**(24): p. 10465-10470.

6. Klimov, V.I., et al., Quantization of multiparticle Auger rates in semiconductor quantum dots. Science, 2000. **287**(5455): p. 1011-1013.

7. Guyot-Sionnest, P., B. Wehrenberg, and D. Yu, Intraband relaxation in CdSe nanocrystals and the strong influence of the surface ligands. Journal of Chemical Physics, 2005. **123**(7).

8. Kambhampati, P., Hot Exciton Relaxation Dynamics in Semiconductor Quantum Dots: Radiationless Transitions on the Nanoscale. The Journal of Physical Chemistry C, 2011. **115**(45): p. 22089-22109.

9. Kambhampati, P., Unraveling the Structure and Dynamics of Excitons in Semiconductor Quantum Dots. Accounts of Chemical Research, 2010. **44**(1): p. 1-13.

10. Knowles, K.E., E.A. McArthur, and E.A. Weiss, Multi-timescale map of radiative and nonradiative decay pathways for excitons in CdSe quantum dots. Abstracts of Papers of the American Chemical Society, 2011. **242**.

11. Mooney, J., et al., Challenge to the deep-trap model of the surface in semiconductor nanocrystals. Physical Review B, 2013. **87**(8).

12. Salvador, M.R., M.W. Graham, and G.D. Scholes, Exciton-phonon coupling and disorder in the excited states of CdSe colloidal quantum dots. Journal of Chemical Physics, 2006. **125**(18).

13. Takagahara, T., Electron-phonon interactions in semiconductor nanocrystals. Journal of Luminescence, 1996. **70**: p. 129-143.

14. Tyagi, P. and P. Kambhampati, False multiple exciton recombination and multiple exciton generation signals in semiconductor quantum dots arise from surface charge trapping. The Journal of Chemical Physics, 2011. **134**(9): p. 094706-10.

15. Tyagi, P., et al., Controlling Piezoelectric Response in Semiconductor Quantum Dots via Impulsive Charge Localization. Nano Letters, 2010. **10**(8): p. 3062-3067.

16. Tyagi, P., et al. Quantized Extrinsic Piezoelectricity in Quantum Dots Revealed by Coherent Acoustic Phonons. in International Conference on Ultrafast Phenomena. 2010. Optical Society of America.

17. Siwick, B.J., et al., An atomic-level view of melting using femtosecond electron diffraction. Science, 2003. **302**(5649): p. 1382-1385.

18. Chatelain, R.P., et al., Ultrafast electron diffraction with radio-frequency compressed electron pulses. Applied Physics Letters, 2012. **101**(8): p. 081901-4.

19. Morrison, V.R., et al., Direct optical measurements of the evolving spatio-temporal charge density in ultrashort electron pulses. Opt. Express, 2013. **21**(1): p. 21-29.

Appendix A – TEM Image

A1 – Freshly Synthesized CdTe nanocrystals

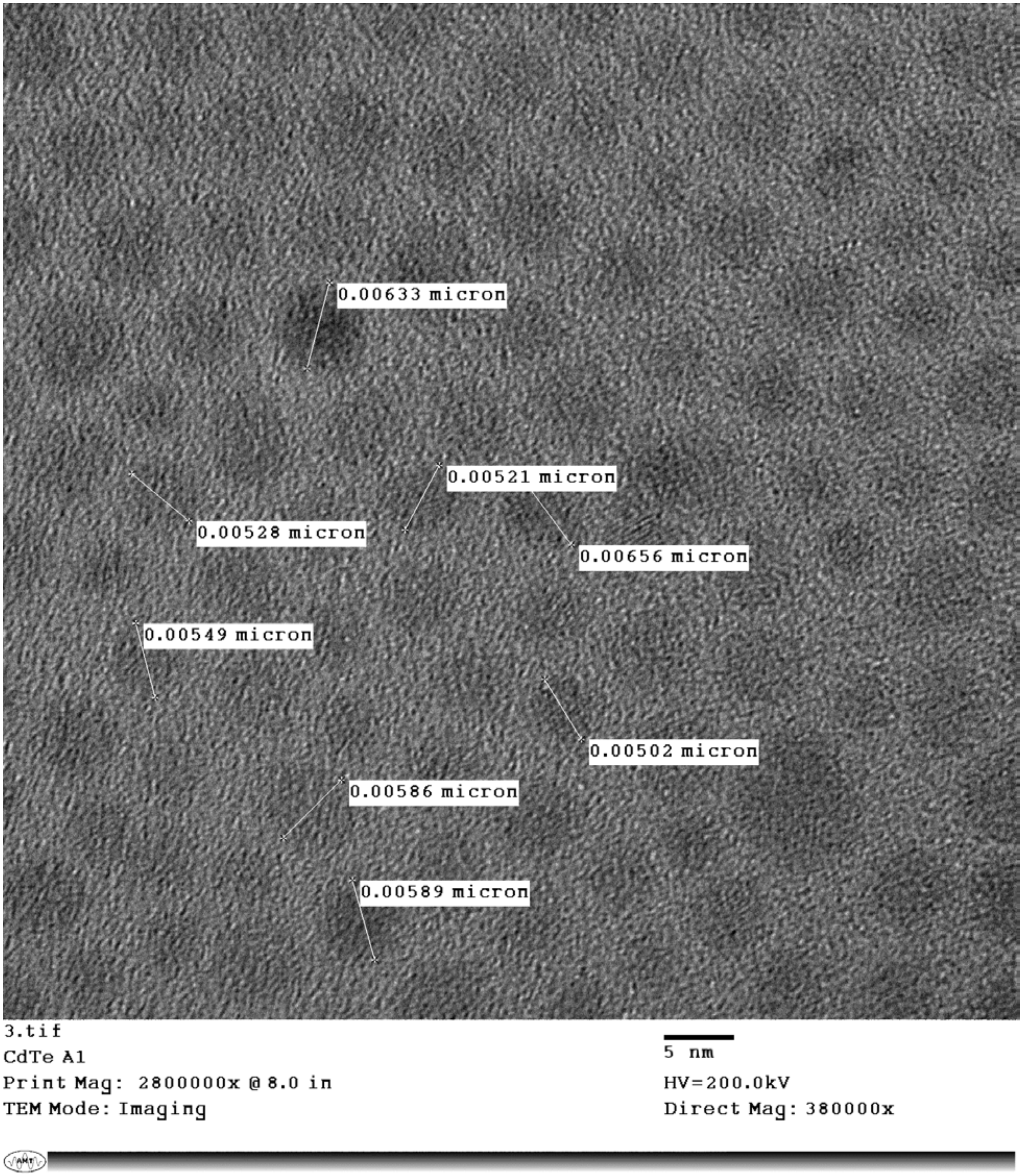

Figure 1 - Representative TEM of Fresh CdTe